DERIVATION AND OBSERVABILITY OF UPPER ATMOSPHERIC DENSITY VARIATIONS UTILIZING PRECISION ORBIT EPHEMERIDES

BY

Travis Francis Lechtenberg

Submitted to the graduate degree program in Aerospace Engineering and the Graduate Faculty of the University of Kansas in partial fulfillment of the requirements for the degree of Master's of Science.

Chairperson: Dr. Craig McLaughlin

Committee members

Dr. Saeed Farokhi

Dr. Shahriar Keshmiri

Date defended:

The Thesis Committee for Travis Lechtenberg certifies that this is the approved Version of the following thesis:

DERIVATION AND OBSERVABILITY OF UPPER ATMOSPHERIC DENSITY VARIATIONS UTILIZING PRECISION ORBIT EPHEMERIDES

Committee:

Chairperson: Dr. Craig McLaughlin

Dr. Saeed Farokhi

Dr. Shahriar Keshmiri

Date approved:

ABSTRACT

Several models of atmospheric density exist in today's world, yet most possess significant errors when compared to data determined from actual satellite measurements. This research utilizes precision orbit ephemerides (POE) in an optimal orbit determination scheme to generate corrections to existing density models to better characterize observations of satellites in low earth orbit (LEO). These corrections are compared against accelerometer derived densities that are available for a few select satellites, notably, the CHAMP and GRACE satellites. These corrections are analyzed by determining the cross correlation coefficients and root-mean-squared values of the estimated corrected densities as compared to the accelerometer derived densities for these satellites. The POE derived densities showed marked improvement using these methods of comparison over the existing empirical density models for all examined time periods and solar and geomagnetic activity levels. The cross correlation values for the POE derived densities also consistently out-performed the High Accuracy Satellite Drag Model (HASDM).

This research examines the ability of POE derived densities to characterize short term variations in atmospheric density that occur on short time scales. The specific phenomena examined were travelling atmospheric disturbances (TAD) and geomagnetic cusps, which had temporal spans of less than half the period of the satellite's orbit, more specifically spans of between four and ten minutes, and less than three minutes respectively. Density variations of shorter duration are more

difficult to observe even in accelerometer data due to diurnal variations that arise from cyclical increases due to the satellite passing from the darkened side of the earth to the lit side. This research also examines the effects of a veritcally propagating atmospheric densities by looking at periods of time during which both the GRACE and CHAMP satellites have coplanar orbits, during which perturbations can be examined for their capability to extend vertically through the atmosphere, as well as their observability in POE derived densities. Additionally, this research extends the application of optimal orbit determination techniques to an additional satellite, the TerraSAR-X, which lacks an accelerometer.

For LEO, one of the greatest uncertainties in orbit determination is drag, which is largely influenced by atmospheric density. There are many factors which affect the variability of atmospheric densities, and some of these factors are well modeled, such as atmospheric heating and to some degree, the solar and geomagnetic activity levels, though some variations are not modeled at all.

The orbit determination scheme parameters found to perform best for most cases were a baseline model of one of the three Jacchia based baseline models, a density correlation half-life of 18 or 180 minutes, and a ballistic coefficient correlation half life of 1.8 minutes. All three Jacchia based models performed very similarly, with the CIRA-1972 model edging out the other two overall. The density correlation half-life's optimal value was usually 180 minutes, though for specific levels of geomagnetic activity, a half-life of 18 minutes was preferable.

During the coplanar periods for both the GRACE and CHAMP satellites, both satellites showed minor density increases that occur on the unlit side of the earth near the equator. These increases were mostly unseen in the precision orbit ephemeris (POE) derived densities, though the POE derived densities did show a slight response to these perturbations. The secondary density increases were seen in both GRACE and CHAMP accelerometer data, and likely existed both above and below the orbits of these two satellites.

The TerraSAR-X densities found for the time period examined in this study using POE data showed deviations from empirical density models of up to 10% for peak atmospheric density values. The CHAMP and GRACE POE derived densities showed a greater relative deviation from the empirical density models during peak density periods, and the deviations for the CHAMP and GRACE satellites' empirically predicted densities much better approximated the density values found using the accelerometers aboard both satellites. As the TerraSAR-X satellite lacks its own accelerometer, the POE derived densities are assumed to be a more accurate representation of the atmospheric densities.

ACKNOWLEDGEMENTS

I would like to thank Dr. Craig McLaughlin for the opportunity to perform this research, as well as his guidance during my time in the graduate program at the University of Kansas. His patience during the accumulation of this research is much appreciated. I would also like to thank Doctors Keshmiri and Farokhi for their participation on my thesis committee.

This research was made possible with the help of many different parties. Funding for this work was provided the National Science Foundation award #0832900 with some additional support provided by the Kansas Space Grant Consortium. David Vallado's help and expertise in working with data conversion scripts and with the Orbit Determination Tool Kit (ODTK) was invaluable. Aid with ODTK scripting was provided by Jens Ramrath at Analytical Graphics, Inc. (AGI). Andrew Hiatt's earlier work formed the basis for the expanded dates for which cross correlation and root-mean squared values were found. Acclerometer derived densities were provided by Sean Bruinsma of the Centre National d'Études Spatiales (CNES) and density values for the High Accuracy Satellite Drag Model (HASDM) were provided by Bruce Bowman of the U.S. Space Command.

TABLE OF CONTENTS

NOMENCLATURE

Symbol	Definition	Units
$\vec{a}$	acceleration vector due to atmospheric drag	m/s^2
a_p	geomagnetic 3-hourly planetary equivalent amplitude index	gamma, Tesla, or kg s m^{-1}
A	satellite cross-sectional area	m^2
A_p	geomagnetic daily planetary amplitude index	gamma, Tesla, or kg s m^{-1}
$\Delta B/B$	estimated ballistic coefficient correction	~
BC	ballistic coefficient	m^2/kg
c_D	satellite drag coefficient	~
d	cross correlation delay	
$F_{10.7}$	daily solar radio flux measured at 10.7 cm wavelength	SFU
$\bar{F}_{10.7}$	$F_{10.7}$ running 81-day centered smoothed data set	SFU
$\bar{F}_S$	Jacchia-Bowman 2008 new solar index	SFU
g_o	gravitational acceleration	m/s^2
Δh	altitude change	m
i	cross correlation series index	
j	user defined Gauss-Markov correlated half-life time series index	
k	Gauss-Markov sequence index	
K_p	geomagnetic planetary index	~
$M_{10.7}$	solar proxy for far ultra-violet radiation	SFU

$\bar{M}_{10.7}$	$M_{10.7}$ running 81-day centered smoothed data set	SFU
m	satellite mass	kg
mx	mean of series x	
my	mean of series y	
M	mean molecular mass	amu
N	number of elements	
Δp	atmospheric pressure change	N/m^2
p_o	absolute pressure	N/m^2
$\hat{P}$	filter covariance matrix	
$\hat{P}^{\theta/(}$	smoother covariance matrix	
$\bar{P}$	differenced covariance matrix	
r	cross correlation coefficient	
$\vec{r}$	satellite position vector	m
R	universal gas constant	$J\ K^{-1}\ mol^{-1}$
$\vec{R}$	McReynold's consistency test ratio	
$S_{10.7}$	solar extreme ultra-violet radiation at 26-34 nm wavelength	SFU
$\bar{S}_{10.7}$	$S_{10.7}$ running 81-day centered smoothed data set	SFU
t	time	S
T	temperature	K
v_{rel}	satellite velocity magnitude relative to Earth's atmosphere	m/s
$\vec{v}_{rel}$	satellite velocity vector relative to Earth's atmosphere	m/s

$w\ t$	Gaussian white random variable	
x	x component of satellite position vector	m
x	Gauss-Markov process dynamic scalar random variable	
x	cross correlation series	
ΔX	state error	
$\Delta\hat{X}$	optimal state error estimate	
$\boldsymbol{X}$	satellite state vector	
$\bar{X}$	difference state vector	
$\hat{\mathbf{X}}_{filter}$	filter state estimate	
$\hat{\mathbf{X}}_{smoother}$	smoother state estimate	
Δy	measurement residual	
y	y component of satellite position vector	m
y	cross correlation series	
Y_{10}	mixed solar index	SFU
z	z component of satellite position vector	m

Greek Letters	Definition	Units
α	Gauss-Markov process variable	
$\Delta\rho/\rho$	estimated atmospheric density correction	~
ρ	atmospheric density	kg/m^3
$\vec{\sigma}$	denominator for McReynold's consistency test ratio	
σ_w^2	variance of Gaussian white random variable	
τ	user defined correlated half-life	
ω_{Earth}	Earth's angular velocity magnitude	rad/s
$\vec{\omega}_{Earth}$	Earth's angular velocity vector	rad/s
Φ	transition function	

Abbreviations	Definition
CC	Cross Correlation
CHAMP	Challenging Minisatellite Payload
CIRA	COSPAR International Reference Atmosphere
COSPAR	Committee on Space Research
CNES	Centre National d'Études Spatiales
DCA	Dynamic Calibration of the Atmosphere
DORIS	Doppler Orbitography by Radiopositioning Integrated on Satellite

Dst	Disturbance Storm Time index
DTM	Drag Temperature Model
ESA	European Space Agency
EUV	Extreme Ultra-Violet
GEOSAT	Geodetic Satellite
GFO	GEOSAT Follow-On
GOES	Geostationary Operational Environmental Satellites
GPS	Global Positioning System
GRACE	Gravity Recovery And Climate Experiment
GSFC	Goddard Space Flight Center
HASDM	High Accuracy Satellite Drag Model
ICESat	Ice, Cloud, and Land Elevation Satellite
MSISE	Mass Spectrometer Incoherent Scatter Extending from ground to space
MUV	Middle Ultra-Violet
NASA	National Aeronautics and Space Administration
NOAA	National Oceanic and Atmospheric Administration
NRLMSISE	Naval Research Laboratory Mass Spectrometer Incoherent Scatter Extending from ground to space
ODTK	Orbit Determination Tool Kit
POE	Precision Orbit Ephemerides
PSO	Precision Science Orbit
RMS	Root-Mean-Squared Value

RSO	Rapid Science Orbit
SBUV	Solar Backscatter Ultraviolet
SEE	Solar Extreme-ultraviolet Experiment
SEM	Solar Extreme-ultraviolet Monitor
SETA	Satellite Electrostatic Triaxial Accelerometer
SFU	Solar Flux Units
SLR	Satellite Laser Ranging
SOHO	Solar and Heliospheric Observatory
SOLSTICE	Solar/Stellar Irradiance Comparison Experiment
SORCE	Solar Radiation and Climate Experiment
STAR	Spatial Triaxial Accelerometer for Research
TAD	Traveling Atmospheric Disturbance
TIMED	Thermosphere Ionosphere Mesosphere Energetics and Dynamics
TLE	Two Line Element
UARS	Upper Atmosphere Research Satellite
XRS	X-Ray Spectrometer

LIST OF FIGURES

LIST OF TABLES

1 INTRODUCTION

1.1 Objective

The goal of this research is to utilize precision orbit ephemerides to generate corrections to existing density models. These corrections yield more accurate density estimates which lead to better drag estimates, improved orbit determination and prediction, as well as an enhanced understanding of density variations in the thermosphere and exosphere. This research primarily focuses on short term variations such as those arising from traveling atmospheric disturbances, geomagnetic cusps, and tides. This research will examine the ability of densities generated by precision orbit ephemerides to characterize these short term density variations. This examination will give a better idea of what temporal resolution can be obtained for short term perturbations in atmospheric density. Some consideration will also be given to the effects of varying levels of geomagnetic and solar activity.

1.2 Motivation

The extreme upper atmosphere, including the thermosphere and exosphere is extremely variable, more so than predicted by current density models. The variations in density magnitude and atmosphere composition at these altitudes can adversely affect the determination and prediction of satellite orbits. Improved orbit determination techniques can be used to help prevent satellite collisions, predict satellite life-spans, and predict satellite reentry times. Several satellite activities

require precise knowledge of the satellite's location and velocity; orbit determination techniques aid in the accurate and precise determination of the satellite's state.

Atmospheric density is one of the largest uncertainties in orbit determination and prediction at low altitudes; it is also one of the primary variables in the calculation of drag on orbiting bodies. Drag is also affected by variables such as the cross sectional area of the orbiting body (A), the mass of the orbiting body (m) and the velocity of the satellite ($\underline{v}$). Other perturbing variables, such as Earth's gravitational field and solar-radiation pressure, are smaller sources of uncertainty than the atmospheric density.

The Earth's atmospheric density is influenced by several effects. The largest influences on atmospheric density are from direct heating from the sun through extreme-ultraviolet (EUV) radiation and the release of charged particles in the atmosphere that interact with the Earth's magnetic field.

Solar heating during periods of extreme solar activity is capable of generating significant short term variations in whole or in part to the atmosphere. The most notable examples of this are atmospheric responses to solar flares, and coronal mass ejections (CMEs). During the period of April 15-24, 2002 a CME impinged the atmosphere, and generated a traveling atmospheric disturbance (TAD). This localized increase in density could be observed moving from pole to pole on the unlit side of the earth [Ref. 1].

Near the geomagnetic poles of the earth, charged particles align with the Earth's magnetic field, and produce abrupt spikes in atmospheric density. Known as

the polar cusp phenomenon, these disturbances are highly localized, and difficult to predict [Ref. 2].

Data used in the model calculations for atmospheric density for magnetic field and solar flux are measured and distributed as averaged three-hour or daily global values. These time scales are generally too large to account for rapid short-term variations in the atmosphere, but are more useful for determination of atmospheric density of larger timescales such as the 14 hour spans examined as the primary time span for this study.

Current density models require corrections as well as an accurate understanding of thermospheric and exospheric densities and atmospheric density variations to determine and predict orbits of individual orbiting bodies. These corrections can be approximated using precision orbit ephemerides (POEs). Using POEs, the behavior of density variations in the upper thermosphere and exosphere is examined at varying degrees of accuracy and precision by varying the ballistic and density coefficient correlation half-lives for a variety of baseline density models. The results of these corrected models will then be compared to accelerometer derived density data from the Spatial Triaxial Accelerometer for Research (STAR) aboard the Challenging Minisatellite Payload (CHAMP) satellite, which was determined by Sean Bruinsma of the Centre National d'Etudes Spatiales (CNES) [Ref. 3]. POE data for the Gravity Recovery and Climate Experiment (GRACE) project were compared against GRACE accelerometer derived densities. Additionally, scenarios of CHAMP and GRACE POE density estimates will be compared with derived density data from

the High Accuracy Satellite Drag Model (HASDM) determined by Bruce Bowman of the U.S. Air Force Space Command [Ref. 4].

Using these estimates of atmospheric density, better models of the drag forces that act upon satellites will be produced. As the accuracy of the density models improve, so too will the drag models. Orbit determination can be significantly improved through these corrections, as drag is one of the primary perturbing forces for low Earth orbiting (LEO) satellites, particularly for orbits for very low altitude satellites. Improved orbit determination leads to better knowledge of a satellite's operational life, its time and location of reentry, as well as future satellite position prediction. This research also brings about a better understanding of how the space environment and weather affect atmospheric density. Currently, knowledge of solar and geomagnetic effects on the atmosphere and exosphere is incomplete; better measurement of density and its variations will facilitate continued study of these effects.

1.3 Satellite Drag

Information on satellite drag characteristics can be found in Reference 5. There are two primary perturbations that affect LEO satellites, the first is acceleration due to atmospheric drag, and the second is additional accelerations due to the oblateness of the earth (J2), and other higher order gravity terms. As the altitude of a satellite decreases, drag becomes a larger and larger factor in the perturbation of a satellite's orbit. After these two forces, the next most significant sources of perturbation are from solar radiation pressure, Earth albedo, and third body effects

from bodies such as the Moon and Sun. Drag is occasionally used for orbit maintenance through aerobraking and tethers which help with satellite orientation, though in general, drag is regarded as a hindrance to the satellite's life span. Satellites at higher altitudes are proportionately more affected by third body effects and solar radiation pressure, as the effects of J2 variations and atmospheric density decrease exponentially with increases in altitude. The continually increasing role of LEO satellites, in both the public and private sectors has led to large amount of research being directed towards the comprehension of the upper atmosphere and its interactions with these satellites in the form of drag. This research will hopefully lead to more accurate atmospheric density models, which can be used for future satellite mission planning. There are three primary goals for modeling drag: first is determining the orbit of the satellite, the second is estimating satellite lifetime, and the third is to determine physical properties of the atmosphere.

Drag is the process through which an object's velocity is altered by the collision of atmospheric particles against its outer hull, which due to the conservation of momentum detract from the velocity of the satellite and transfer momentum to atmospheric particles. This force is non-conservative as the total mechanical energy of the satellite changes due to this interaction with the atmosphere. The majority of the momentum change is localized around periapsis, which reduces the satellites semi-major axis and eccentricity, slowly altering the satellites orbital path to approach a circular orbit.

According to Vallado, [Ref 5] a complete model of atmospheric perturbations must include knowledge of molecular chemistry, thermodynamics, aerodynamics, hypersonics, meteorology, electromagnetics, planetary sciences, and orbital mechanics. Analysis of satellite drag requires a thorough understanding of atmospheric properties. One way of measuring drag is to measure accelerations induced upon the satellite and attempt to isolate the acceleration due to drag, which occurs along the satellite's track. The following equation describes the relationship between acceleration drag forces, and the independent variables of atmospheric density and velocity. Other variables are generally grouped together for the purpose of determining the acceleration due to drag into a quantity known as ballistic coefficient.

$$\vec{a} = -\frac{1}{2}\frac{c_D A}{m}\rho v_{rel}^2 \frac{\vec{v}_{rel}}{|v_{rel}|} \tag{1.1}$$

The drag coefficient c_D is a dimensionless quantity describing the effect that drag has on the satellite and is based largely on the satellite's configuration. The dependence on satellite configuration and variability of the atmosphere's characteristics mean that the drag coefficient for the satellite is typically estimated. Drag coefficients for satellites in the upper atmosphere are typically approximated as 2.2 for flat plates, and 2.0 to 2.1 for spherical bodies. At most, the drag coefficient is estimated to 3 significant figures. The difficulties that arise from complex satellite

configurations require further improvements in satellite drag determination to be researched.

ρ denotes atmospheric density, the concentration of atmospheric particles in a given volume. Density can be one of the more difficult parameters to approximate for a satellite drag situation due to variability of the satellite's cross-sectional area, *A*, and uncertainties in C_D. The variability of *A* is primarily due to constantly changing attitudes of satellites lacking attitude control. A better approximation of *A* and therefore ρ may be obtained if the attitude and geometry of the satellite at various points in time is more accurately known. Mass, *m*, can also be variable over a given amount of time due to orbit maintenance maneuvers, as well as accumulated atmospheric particles that can bond to the surface of the satellite. The relative velocity vector $\vec{v}_{rel}$ is defined as the velocity vector relative to the rotating Earth's atmosphere and can be determined by the following equation.

$$\vec{v}_{rel} = \frac{d\vec{r}}{dt} - \vec{\omega}_{Earth} \times \vec{r} = \left[\frac{dx}{dt} + \vec{\omega}_{Earth} y \frac{dy}{dt} - \vec{\omega}_{Earth} x \frac{dz}{dt} \right]^T \tag{1.2}$$

The atmosphere of the Earth rotates with the Earth, with a velocity profile in which the atmosphere moves most quickly close to the surface of the earth and decreases in speed with altitude. Satellites are subject to both this general motion, as well as atmospheric winds. This atmospheric motion generates side and lifting forces, as well as drag forces. The drag forces are defined as being along the velocity vector of the satellite.

Another way of representing the satellites susceptibility to drag is through the ballistic coefficient (BC). There have been multiple definitions of ballistic coefficient over the years, so clarity of definition is important. The traditional definition of ballistic coefficient, a remnant from the days of muskets and cannons is defined as follows.

Classical Definition

$$BC = \frac{m}{c_D A} \tag{1.3}$$

The definition used by the Orbit Determination Tool Kit (ODTK), the software primarily used for this research, the definition used by Bruce Bowman, and the definition that will be referred to for the rest of this document, however, is this inverse of this relationship.

Definition in this document

$$BC = \frac{c_D A}{m} \tag{1.4}$$

Using this definition, a lower value of BC equates to drag having less of an effect on the given satellite instead of more as in the classical definition.

Static and time varying atmospheric models rely on two relationships that are core to understanding how pressure and density change within the atmosphere [Ref 5]. The first is the ideal gas law.

$$\rho = \frac{p_o M}{g_o R T} \tag{1.5}$$

The ideal gas law characterizes the basic interactions between atmospheric pressure p_o, the mass of the atmospheric constituents M, gravitational acceleration g_o, the universal gas constant R and the temperature of the atmosphere T. As the Earth rotates throughout the day, different portions of the atmosphere are exposed to the sun's rays, which heat the atmosphere. This heat drastically affects atmospheric density through interactions with both the pressure and density of the gases in the upper atmosphere. Atmospheric densities observed on the lit side of the Earth are significantly greater than those found on the unlit side and this connection between temperature and density is of great importance as it is the single largest cause of variation in atmospheric density on a daily basis.

The second equation is the hydrostatic pressure equation which characterizes the change in pressure found to result from changes in height. The hydrostatic equation is defined below.

$$\delta p = -\rho g \delta h \tag{1.6}$$

These two relationships are paramount to understanding the complex interactions in atmospheric density that occur in the atmosphere. Both equations demonstrate the interdependency of pressure and density values. Through these two relationships, much of the atmosphere may be characterized.

1.4 Neutral Atmosphere

The summary contained within this subsection is taken from References 5-9, and a large bulk of the information is taken from Reference 5. For more detailed information on the neutral atmosphere, thermospheric and exospheric density, baseline variations in atmospheric density, atmospheric density drivers, and the space environment, see References 6 and 7.

1.4.1 Neutral Atmosphere Structure

The neutral atmosphere is divided into five layers, dependent upon the processes that take place therein. Each shell terminates at a sometimes ill-defined boundary layer known as a pause that may stretch over tens of kilometers in altitude. The shell at the lowest layer, known as the troposphere is the atmosphere in which we live and breathe. The troposphere ranges from 0-12 km in altitude and is composed of roughly 78% Nitrogen, 21% Oxygen, and the remaining 1% is composed of various other elements, such as carbon dioxide, argon, and helium. The stratosphere lies above the troposphere, and unlike the troposphere, the temperature increases with altitude. The stratosphere terminates around 45 km where it gives way to the mesosphere. The mesosphere is a region of colder temperatures above the stratosphere, and ends at about 80-85 km. The mesosphere is rarely studied as scientific instruments are rarely positioned there due to the mesosphere being above the upper limits of ground based weather balloons, and below the lowest orbit of satellites. These three levels are known as the lower atmosphere, and have very little

bearing on the challenges posed by orbit determination, the exception to this being upward propagations of disturbances observed in the lower atmosphere.

The thermosphere lies above the mesosphere, and is where the composition of the atmosphere shifts from being largely nitrogen to mostly atomic oxygen at altitudes of around 175 km. The thermosphere ranges from the mesopause at near 80-85 km to altitudes of 600 km. Temperature differentials in the thermosphere arise from constituents of the atmosphere absorbing ultraviolet radiation which causes the temperature to increase. Many LEO satellites, as well as the space shuttle carry out most, if not all of their activities in the thermosphere. The exosphere lies at an even higher altitude, where the interactions between particles are few, and as such, the particles primarily follow Newtonian physics. The exosphere and much of the thermosphere have such low densities, that the fluid is treated as a collection of individual particles, rather than as a gas. Above 600 km in the exosphere, lighter particles dominate, and Helium becomes the dominant constituent of the atmosphere until altitudes of nearly 2500 km, above which, Hydrogen dominates.

1.4.2 Variations Affecting Static Atmospheric Models

The simplest atmospheric model is the static model as all atmospheric parameters are assumed constant. There are however variations which have effects on static models, principle among these, are longitudinal and latitudinal variations. As satellites cross the equatorial plane, the effective altitude of the satellite decreases due to the earth's oblateness. Since the effective altitude decreases, the density of the atmosphere that the satellite passes through increases. Longitudinal variations are

usually considered more in time varying models due to the significant differences between the lit and unlit sides of the earth; the lit side being significantly denser than the unlit side. There are also geographical concerns when accounting for longitudinal variations. Features such as oceans, mountain ranges, deserts, and other ecological systems of differing characteristics can have effects on the upper atmosphere due to their effects upward propagation.

1.4.3 Time-Varying Effects on the Thermospheric and Exospheric Density

The largest temporal effects on atmospheric density are the diurnal cycle, wherein the Sun heats the atmosphere and increases the density at upper altitudes, and the solar cycle, the cycle during which the Sun becomes more or less active over a cycle of 11 years. There are two ways in which the Sun heats the Earth's atmosphere, first through direct EUV heating, and the second through charged particles that are emitted from the sun which then interact with the Earth's magnetic field lines to increase atmospheric density. There are also several other temporal variations that affect atmospheric density:

- 27-Day Solar Rotation Cycles
- 11-Year Solar Cycle
- Variations Between Solar Cycles
- Semiannual/Seasonal Variations
- Rotating Atmosphere
- Winds

- Magnetic Storm Variations
- Gravity Waves
- Tides
- Irregular Short-Period Variations

27-Day Solar Rotation Cycles: These effects stem from the Sun's 27-day rotation, which systematically exposes the earth to the entire surface of the Sun. Irregular variations in the solar flux from the sun is related to the growth and decay of active solar regions which revolve with the Sun. Solar flux of the decimetric-wavelength is then correlated to atmospheric density.

11-Year Solar Cycle: Approximately every 11 years, the Sun's poles undergo a reversal, switching the orientation of the magnetic poles. The period in which the sun is most chaotic and active is known as solar maximum and is generally accompanied by increased solar spots, solar flares, and solar activity in general. Due to the violent nature of the Sun during this period, an increased amount of solar energy and ejecta from the sun cause the Earth's atmosphere to become significantly more dense and variable. Conversely, during solar minimum, there is relatively little activity on the sun, and sun spots and solar flares are relatively rare. During this period, the atmosphere contracts and is generally less dense at all altitudes. Since the poles reverse every 11 years, it actually takes around 22 years for the Sun to return to its original state; the 11 year cycle is generally referred to, as that is the period for the solar activity.

Solar Cycle Variation: There is an additional solar cycle that lags slightly behind the 11-year cycle of solar spots and pole reversals. The exact cause for this variation is unknown, but it is speculated that this secondary cycle is also due to sunspot activity.

Variations between Solar Cycles: There are also variations due to certain solar cycles being particularly more violent or benign than usual. This latest cycle has had an unusually prolonged and quiet solar minimum for example.

Semi-Annual/Seasonal Variations: These variations are due primarily to the axial tilt of the earth and the amount of sunlight a hemisphere gets. For example, the northern hemisphere is more dense during June-August, and the southern hemisphere is relatively less dense. Additionally, the distance from the Sun to the Earth plays a role in the density of the atmosphere as that distance varies throughout the year due to the minor eccentricity of Earth's orbit.

Rotating Atmosphere: To some degree, the atmosphere rotates with the Earth. The atmosphere revolves faster closer to the Earth, and slows down with higher altitudes.

Winds: Weather patterns are quite complex and can have a profound impact upon atmospheric densities. Variations in temperature profiles cause winds which can alter the effective speed of a satellite altering the perceived density at that altitude as well as actually altering the density of the atmosphere.

Magnetic Storm Variations: Minor fluctuations in the Earth's magnetic field produce some degree of density variation due to ionized particles aligning with the

Earth's magnetic field. These disturbances become much more pronounced during active geomagnetic periods. Magnetic storms occur when variations in the solar wind impinge the atmosphere, usually following solar flares and coronal mass ejections. Substorms are changes that occur within the magnetosphere, the energy disturbances due to this are then funneled along magnetic field lines towards the poles and are often observable as auroral activity.

Gravity Waves: Gravity waves, as the name implies, are waves that are generated due to gravity, wherein, a disturbance moves a body from equilibrium, generally by increasing its potential energy and then gravity attempts to restore equilibrium. This causes the body to overshoot its equilibrium point and then attempt to restore itself through other methods, such as pressure. The effect is very similar to that which is observed in low level physics courses with springs.

In the atmosphere, a disturbance usually consists of an action altering the density or pressure of the atmosphere locally. An example would be wind causing pressure differentials after moving over a hill or mountain. The displaced air is pulled down by gravity, and then compressing the atmosphere against the Earth, this results in a wave. The effect of these gravity waves is usually limited to the lower atmosphere, into the lower thermosphere. The waves grow in magnitude as the density decreases due to the need to maintain the total energy of the wave. As the waves gain altitude, they are gradually dissipated due to viscous effects.

Tides: Ocean and atmospheric tides caused by gravity have a relatively small effect on atmospheric density. Solar tides, on the other hand, can have a profound

effect on the density and nature of the atmosphere. The solar diurnal tide is a dominating factor in the thermosphere at altitudes above 250 km. This is due to EUV absorption at these altitudes increasing both the temperature and density of the atmosphere.

Irregular Short Period Variations: Irregular short period variations are small disturbances caused by random solar flares, atmospheric hydrogen currents, and transient geomagnetic disturbances.

1.5 Atmospheric Density Models

The following section is primarily a summary of information found in Reference 5, which contains an introduction to commonly used atmospheric density models. Most atmospheric models are developed using one of two approaches. 1) Using laws of conservation as well as models of the atmospheric constituents to create a physical model of the atmosphere. 2) Using simplified physical concepts in conjunction with in-situ measurements and satellite tracking data. The models are also divided into static and time-varying models. Different types of models may be better for differing applications.

Time varying models are generally the most accurate and complete, but require accurate data for different times, and are generally computationally expensive. A simple static exponential model can turn out to be accurate for a given time even though it is much less expensive computationally.

Models examined in this research include: Jacchia 1971 [Ref. 11], Jacchia-Roberts [Ref. 12], Committee on Space Research (COSPAR) International Reference

Atmosphere (CIRA 1972) [Ref. 13], Mass Spectrometer Incoherent Scatter (MSISE 1990) [Ref. 14], and Naval Research Laboratory Mass Spectrometer Incoherent Scatter (NRLMSISE 2000) [Ref. 15]. The "E" suffix on the last two models indicates that these are extended models in that they reach from sea level to space.

1.5.1 Solar and Geomagnetic Indices

Two of the primary drivers behind variability in atmospheric densities are solar and geomagnetic activity. Solar activity accounts for most of the variability in the upper atmosphere. These variations are caused by atmospheric heating that occurs due to the absorption of EUV radiation. Since almost all incoming radiation is absorbed by the atmosphere, a proxy index is used to measure the amount of radiation incoming to the earth in the form of 10.7 cm wavelength electromagnetic radiation. The 10.7 cm wavelength and EUV radiation have been found to both originate from the same layers of the sun's chromosphere and corona. Some satellites are equipped to measure EUV flux directly, but the only model to currently incorporate these readings is the Jacchia-Bowman model. $F_{10.7}$ has been regularly recorded since 1940 in Solar Flux Units (1 SFU = 10^{-22} W m^{-2} Hz^{-1}), and typical values range from 70-300 SFU for any given day. Measurements of solar flux are distributed daily by the National Oceanic and Atmospheric Administration (NOAA) at the National Geophysical Data Center in Boulder, Colorado. From 1947 until 1991, measurements were taken at 1700 UT at the Algonquin Radio Observatory in Ottawa, Ontario. Since then, measurements have been taken at the Dominion Radio Astrophysical

Observatory in Penticton, British Columbia. Measurements of solar flux can be found in Reference 17.

Variations in the earth's magnetic field can affect satellites in numerous ways. First, the charged particles cause ionization in the upper atmosphere. Second, the charged particles alter the attractive forces experienced by the satellite. Third, ionization interferes with satellite tracking and communication. Finally, variations in the magnetic field can interfere with onboard magnets used for attitude adjustment.

Geomagnetic activity is measured to determine atmospheric heating by a quasi-logarithmic geomagnetic planetary index denoted as K_p. The K_p index is a worldwide average of geomagnetic activity below the auroral zones. Measurements of K_p are taken every 3 hours from 12 locations worldwide. The geomagnetic planetary amplitude, a_p, is a linear equivalent of the K_p index, and is a 3-hourly index, which is averaged to a daily planetary amplitude A_p. Planetary amplitude is measured in gamma, defined as:

$$gamma = 10^{-9} Tesla = 10^{-9} \frac{kg \cdot s}{m} \tag{1.7}$$

Values for planetary amplitude range from 0 to 400, though values rarely exceed 100 and average at about 10-20. Geomagnetic activity has two primary cycles, the first mirrors the 11 year solar cycle with maximums occuring during the declining phases of the solar cycles. The second is a semi-annual cycle due to the variability of the solar wind's incidence with the earth's magnetosphere. Data on

geomagnetic planetary indices, and planetary amplitudes is available from Reference 18.

Solar and geomagnetic activity can be separated into bins as defined in Reference 15 as:

Table 1.1: Defined Solar and Geomagnetic Activity Bins

$F_{10.7}$ Solar Activity			A_p Geomagnetic Activity	
Low	$F_{10.7}<75$		Quiet	$A_p<10$
Moderate	$75<F_{10.7}<150$		Moderate	$10<A_p<50$
Elevated	$150<F_{10.7}<190$		Active	$50<A_p$
High	$190<F_{10.7}$			

For the examined dates, the lifespan of the CHAMP satellite, and the full duration for which there are measurements, the ratios of solar and geomagnetic activity are allotted the following proportions:

Table 1.2: Solar and Geomagnetic Activity Distribution

	1950-Present	CHAMP Mission Life	Data Series
Low Solar	16.83%	20.77%	10.61%
Moderate Solar	52.25%	57.80%	51.89%
Elevated Solar	16.25%	11.96%	20.27%
High Solar	14.67%	9.47%	17.24%
Quiet Geomagnetic	59.33%	63.74%	24.43%
Moderate Geomagnetic	36.94%	33.47%	48.39%
Active Geomagnetic	3.74%	2.80%	27.18%

1.5.2 Jacchia 1971 Atmospheric Model

The Jacchia 1971 atmospheric model was created as a replacement for the model proposed the year previously, the Jacchia 1970 model. The model was updated in an attempt to meet the composition and density data derived from mass

spectrometer and EUV-absorption data, with ranges from altitudes of 110-2000 km [Ref. 11]. The model begins analysis by assuming a boundary atmospheric condition at 90 km and that discrepancies in the mean molecular mass below 100 km are due to dissociation of oxygen molecules. From 90-100 km, an empirical model of the mean molecular mass is used, and from 100-150 km a diffusive model is used until the ratio of O/O_2 reaches 9.2 [Ref. 11]. Above 125 km, the atmosphere is modeled with a temperature profile where the temperature approaches an asymptotic value of the exospheric temperature. To even out shorter term variations, such as the 27 day solar, cycle, the model is adapted to use a running 81 day average for geomagnetic and solar activity levels.

1.5.3 Jacchia-Roberts Atmospheric Model

Largely based upon prior work done for the Jacchia 1970 model, the Jacchia-Roberts atmospheric model determines exospheric temperature using analytical expressions based on functions of position, time, solar activity, and geomagnetic activity [Ref. 12]. Density is then empirically determined from atmospheric temperature profiles, or from the diffusion equation. Roberts modified the 1970 model by using partial fractions to integrate from 90-125 km, and used a different asymptotic function from Jacchia's 1971 model in order to achieve an integrable form [Ref. 12].

1.5.4 CIRA 1972 Atmospheric Model

An atmospheric model is periodically released by the Committee on Space Research (COSPAR); releases began in 1965 and the model was updated in 1972 to incorporate the findings of the Jacchia 1971 model, as well as mean values for low altitudes (25-500 km), satellite drag, and ground based measurements [Ref. 13]. The model is semi-theoretical, but leaves some free variables.

1.5.5 MSISE 1990 Atmospheric Model

These models are formulated utilizing mass spectrometer data from satellites, and well as incoherent scatter radar from ground based sites. In addition, data is used from the Drag Temperature Model (DTM), which is based on air-glow temperatures [Ref. 14]. The advantages posed by the MSIS models over modified Jacchia-Roberts models are that the MSIS models take into account a greater amount of data than was available during the creation of the Jacchia-Roberts model, and that these models tend to require smaller amounts of code. The modified Jacchia-Roberts model does out perform this model in certain situations though.

1.5.6 NRLMSISE 2000 Atmospheric Model

The newest release in the MSIS line is the NRLMSISE 2000 model, released by the Naval Research Laboratory, which incorporates satellite drag data using spherical harmonics over two complete solar cycles [Ref. 15]. Both MSISE models require less code in order to determine the atmospheric densities, though Jacchia based models tend to perform better in certain scenarios.

1.5.7 Jacchia-Bowman Atmospheric Models

The Jacchia-Bowman models are derived from Jacchia's diffusion equations, and are intended to reduce density errors by using solar indices, improved semiannual density variation models, and a geomagnetic index algorithm. The newest version of the Jacchia-Bowman model utilizes data from both ground based observations, as well as on-orbit satellite data to calculate thermospheric and exospheric temperatures, which are used to generate density values. Further details apart from those espoused here can be found in Reference 16.

The model uses a combination of four measurements of solar flux to better model semiannual seasonal variations that can be observed peaking in April and October, and attaining minimums in January and July. The October maximum, and July minimum are observed as being more pronounced than the April maximum, and January minimum. The Jacchia-Bowman model uses a previously defined function for the atmospheric density that is a relationship between density, time, amplitude and height as a baseline for attempting to better model this semiannual variation.

Typically, the ultraviolet solar flux is estimated using measurement of the 10.7 cm wavelength, which serves as a proxy for EUV activity. Most EUV energy emitted from the sun is absorbed in the upper thermosphere, thus requiring a proxy. The 10.7 cm wavelength is usually referred to as $F_{10.7}$. The $F_{10.7}$ wavelength is typically represented in models as an 81 day running average denoted by $\bar{F}_{10.7}$. $F_{10.7}$ values tend to bottom out during solar minimum, thus creating a need for the Jacchia-Bowman model to incorporate other models of solar activity.

To account for solar activity after $F_{10.7}$ values bottom out, three other sources of measuring solar activity were used. In December 1995, NASA/ESA launched the Solar and Heliospheric Observatory (SOHO) which uses an instrument dubbed the Solar Extreme-ultraviolet Monitor (SEM). This device measures wavelengths of 26-34 nm, and converts the measurements to SFU. This index is useful for measuring EUV line emissions and is denoted by S_{10} or $\bar{S}_{10}$ for 81-day running averages.

NOAA's series of operational weather satellites are equipped with a Solar Backscatter Ultraviolet (SBUV) spectrometer that is most commonly used to monitor ozone in the lower atmosphere. In its discrete operating mode, the SBUV measures MUV radiation near the 280 nm wavelength, which is near the Mg *h* and *k* lines. This allows the index to measure the chromospheric and a portion of the photospheric solar active region activity. Linear regression of the $F_{10.7}$ index is used to attain the M_{10} index used here.

The GOES X-ray spectrometer (XRS) instrument provides data for the last of the solar indices used in the Jacchia-Bowman model. The XRS measures X-rays in the 0.1-0.8 nm range. X-rays at these wavelengths are a major energy source during periods of high solar activity, but during periods of low to moderate solar activity hydrogen (H) Lyman-α dominates. Lyman-α values are obtained from the SOLSTICE instrument on the UARS and SORCE NASA satellites as well as by the SEE instrument on NASA TIMED research satellite. The SFU values of both the X_{10} and Lyman-α measurements are weighted towards X_{10} values during periods of high

solar activity, and towards the Lyman-α values during periods of moderate to low solar activity to create a mixed solar index known as Y_{10}.

To estimate thermospheric temperatures, the Jacchia-Bowman model used a weighted indexing scheme that incorporated both $\bar{F}_{10}$ and $\bar{S}_{10}$ data, and is denoted as $\bar{F}_S$.

$$\bar{F}_S = \bar{F}_{10} W_T + \bar{S}_{10} \ 1 - W_T \tag{1.8}$$

where:

$$W_T = \ \bar{F}_{10} / 240 \ ^{1/4} \tag{1.9}$$

The Jacchia-Bowman model uses this index as well as the delta values between the daily values and running 81-day averages for all four previously referenced indexes to determine thermospheric densities. The newest model does a much better job of measuring decreases in density during the solar minimum, though it does not completely capture the density variation. The Y_{10} index was recently added in the latest (2008) model and accounts for differences observed between the 2008 and 2006 variations of the model.

In addition to modeling indices of solar activity, the Jacchia-Bowman model also attempts to model changes in the atmosphere caused by geomagnetic storms. The Disturbance Storm Time (Dst) index is used as an indicator of the strength of the storm-time ring current in the inner magnetosphere. Most magnetic storms begin with a sharp rise in Dst due to increased pressure from the solar wind. Following this,

the Dst decreases drastically for the duration of the storm as ring current energy increases during the storm's main phase, funneling energy along magnetic field lines. During recovery phase, Dst increases back to normal levels as ring current energy decreases. Dst is considered a more accurate measure of energy deposited in the thermosphere than the standard a_p index measured by high latitude observatories. Dst is considered more accurate because these observatories can be blinded to energy input during storms and thus underestimate the effect of geomagnetic storms on the atmosphere.

1.5.8 Russian GOST Model

The GOST model is an analytical model developed during the Soviet era to determine atmospheric densities from observations of Cosmos Satellites [Ref. 5]. The model has been used for nearly 30 years, and is still incorporating satellite measurements to this day [Ref. 5]. The GOST model is able to disregard specified parameters easily by omitting them from the calculation; this property allows the GOST to gain its estimates very quickly, and reduce required computer resources [Ref. 5].

1.6 Previous Research on Atmospheric Density Model Corrections

There are two methods of research currently in use to address the problems of modeling atmospheric density for the purpose of determining satellite drag. The first is though Dynamic Calibration of the Atmosphere (DCA), and the second is through the analysis of accelerometer data from satellites themselves.

1.6.1 Dynamic Calibration of the Atmosphere

Dynamic Calibration of the Atmosphere (DCA) is a technique for improving or correcting existing atmospheric models and their corresponding densities. DCA provides information about density variations in the atmosphere and the statistics of these variations [Ref. 5]. DCA techniques have been used since the early 1980's and are an area of ongoing research in applications of orbit determination. DCA modeling techniques estimate density corrections every three hours to maintain consistency with initial work performed by Nazarenko in the 1980's. DCA methods originally determined density from empirical inputs as opposed to observed geomagnetic data which was judged unreliable in the early 1980's. Current DCA approaches also incorporate satellite data from accelerometers and two-line element sets, and give density corrections on a daily basis. DCA techniques use an input of a "true" ballistic coefficient in order to determine density corrections to models; these corrections are usually made to variants of Jacchia-71 and MSIS models [Ref. 5]. There have been several usages of the DCA approach in recent years, primarily detailed in References 4-27.

Reference 4 incorporated data from 75 inactive payloads and debris to solve for corrections to thermospheric and exospheric neutral density for altitudes between 200-800 km. Corrections were regularly made every three hours and densities could be predicted up to three days in advance using predictions of $F_{10.7}$ solar flux. Reference 4 improved upon DCA techniques by using prediction filters, and using a

segmented solution for ballistic coefficient techniques to achieve density accuracies that were within a few percent of true densities.

Reference 20 describes a method for determining daily atmospheric density values by basing them upon satellite drag data. A differential orbit correction program using special perturbations orbit integration was applied to radar and optical observations of satellites to obtain 6-state element vectors, as well as the ballistic coefficients for the satellites observed in this study. The states were integrated from the modified Jacchia 1970 model that was also utilized for HASDM. Daily temperature and density values were calculated using computed energy dissipation rates. These temperatures were verified by examining daily values of satellites as obtained by this DCA examination in comparison to values obtained from the HASDM DCA program. The densities were verified by comparing them against historical data for the past thirty years.

The goal of Reference 21 was to represent the observed semiannual density variation of the last 40 years. The study took historical radar observational data of 13 satellites with perigees ranging from 200-100 km. Using this historical data, accurate daily density values at perigee have been found by relating the density to energy dissipation rates. The study was able observe the semiannual variation, as well as characterize variations due to altitude and solar activity.

Reference 22 estimates corrections to the GOST atmospheric model using data from Two Line Element (TLE) sets. These density corrections are made using a bias term, as well as a linear altitude grid. The model uses input in the form of TLE

data from 300-500 satellites in LEO orbit, in addition to observed solar flux and geomagnetic data. The model was examined over a period of 10 months in the later part of 2002 and early 2003. The paper demonstrates the capability to monitor density variations given satellite TLEs in nearly real time.

Reference 23 also uses TLEs to assess density corrections. These TLEs were taken from inactive objects in LEO orbit. Again, density was given a linear relationship with altitude. Hundreds of satellites were observed and then used to determine density. The accuracy of these densities was judged by comparison of orbit determination and predictions obtained with and without the estimated density corrections.

Reference 24 uses DCA techniques as well as density corrections to better estimate reentry times for spacecraft. In this instance, corrections were made to the NRLMSISE 2000 model. This study considered both spherical and non-spherical objects in orbit around the earth. Reentry predictions increased in accuracy in this study, though the effect was more pronounced for spherical satellites which had unvarying BCs.

Reference 25 estimated corrections to the NRLMSISE 2000 model in an effort to improve orbit determination and prediction. The study acknowledges the limitations of using purely statistical corrections to atmospheric density, while still demonstrating marked improvement over baseline density models.

Reference 26 sought to improve upon existing DCA techniques based on observations during the validation of Russian DCAs. The study found that successive

refinements using a series vanishing coefficients could remove errors from the solution. Each refinement used the previous refinement as a starting point as its basis and the process continued until improvements were no longer made. The primary goal of this study was to reduce residual errors in the calculation of drag.

Reference 27 compares results from using DCA techniques in conjunction with the NRLMSISE model to results obtained from Nazarenko and Yurasov in their DCA base atmospheric density correction. The study examined two 4-year periods with varying levels of geomagnetic and solar activity; the first was from 11/30/1999-11/30/2003, and the second from 1/1/1995-6/1/2000. The study used data from 477 satellites in LEO orbit to derive corrections, and found that the models were valid, and proved that DCA is an effective method for determining corrections to current atmospheric density models.

DCA, though an extraordinarily useful tool, has limitations. DCA approaches are limited to localized time periods for which the DCA technique is applied. In order to correctly anticipate satellite orbit behavior, constant updates on atmospheric density are required, as well as archival knowledge of previous density corrections. DCA approaches also suffer from limited spatial and temporal resolution. The corrections take place on time scales of hours or days, and are ill suited for measuring short term variations in the thermosphere. This lack of temporal resolution is introduced by the usage of daily flux values, and 3-hour geomagnetic indices. Atmospheric variations cannot be represented during the averaging intervals of these indices. Another area of weakness for the DCA approach is the reliance on TLEs;

though TLE data for LEO objects is plentiful, it lacks accuracy in regards to atmospheric density. HASDM References 4, 20, and 21, uses radar observations of LEO objects to obtain better density accuracies, though radar accuracy pales in comparison to that achievable by Precision Orbit Ephemerides (POE) or Satellite Laser Ranging (SLR), and is not generally available to parties outside the Department of Defense.

Research is currently being conducted on applying DCA techniques to GEODYN, the NASA GSFC Precision Orbit Determination and Geodetic Parameter Estimation Program [Ref. 28]. Density corrections were applied to the NRLMSISE 2000 model with the intent of improving orbit precision of the GEOSAT Follow-On (GFO). The results were compared to the MSIS-86 model for a range of solar and geomagnetic activity levels. Results showed little improvement over the existing MSIS-86 model at 800 km, though corrections valid up to 800 km are anticipated to yield considerably improved results [Ref. 28].

Currently, efforts are being made to use TLE data to calibrate thermospheric neutral density models [Ref. 29]. This study uses the large amount of available TLE data to calibrate density models with a lag of but a few days. The study tested two separate calibration schemes on a batch of 50 satellites during the year 2000. One calibration technique applied height-dependent scale factors to the density, and the other made corrections to the CIRA 1972 model temperatures, which vastly affects the physical density model. The errors were reduced in this study from 30% for raw empirical models to 15% for corrected models.

1.6.2 Accelerometers

Another way of measuring atmospheric drag is through the use of accelerometers aboard spacecraft in LEO. Recently, accelerometer accuracy has increased to the point where density can be estimated using the drag equation and measuring non-conservative forces. These accelerometers decrease in usefulness when orbit station keeping and attitude correction maneuvers are being made as these activities introduce additional forces into the accelerometer's analysis. In LEO, drag dominates as the primary non-conservative force; however, several other non-conservative forces exist such as solar radiation pressure, Earth albedo, and Earth infrared radiation. Accurate measurements of solar flux and earth radiation pressure can allow the non-drag terms to be accurately calculated using data received from accelerometers. So far, very few satellites have been equipped with accelerometers that are sufficiently sensitive to measure atmospheric drag, and hence atmospheric density. The only satellites currently equipped with accelerometers of sufficient accuracy are the CHAMP and GRACE satellites. Accelerometers have almost exact opposite characteristics from two-line element sets in that they are highly accurate, though data sets are limited. Two-line element sets tend to be readily available for many satellites, yet are relatively inaccurate. Reference 30 examined accelerometer data from the Satellite Electrostatic Triaxial Accelerometer (SETA) experiment that confirmed the effect of geomagnetic energy being deposited near the geomagnetic poles and hence creating a travelling atmospheric disturbance that propagated toward the poles.

References 31 and 32 detail techniques used to derive atmospheric densities from accelerometer readings, and References 3 and 33 give accelerometer data derived using these techniques.

Reference 31 demonstrates the capability of the CHAMP accelerometer to measure major thermospheric events such as coronal mass ejections (CME) impinging the Earth's atmosphere. The study used accelerometer data to model non-conservative forces instead of relying upon models as the accelerometer is much more precise. Though precise, the accuracy of these measurements from accelerometers is suspect and it was judged the accelerometers likely require calibration and independent verification of data through either POEs or SLR data if this accelerometer data was to be used in subsequent studies.

Reference 32 found that total atmospheric density could be determined using the accelerometer data with the help of accurate force models for other non-conservative forces such as radiative effects. The study acknowledged the susceptibility of density readings to atmospheric wind in along track directions which can increase or decrease the perceived density. The densities could also be affected by systematic bias due to uncertainty in the drag coefficient model as CHAMP's configuration is rather complex for drag coefficient determination. Initial results showed a very high accuracy in determining atmospheric density, which was projected to improve still further with the addition of more data points, as well as better density estimation techniques.

Reference 3 describes the process through which atmospheric density may be determined given accelerometer readings. The CHAMP satellite provides decent geographical and altitude coverage during the course of its allotted 5-year lifespan due to it high-inclination orbit. The data required correcting for orbital maneuvers, specific events, and instrumental bias. The total density was then calculated using a 15-plate model for the drag coefficient. Accuracy was dependent on uncertainties in accelerometer calibration parameters and the aerodynamic coefficient, as well as the geomagnetic activity at the time in question.

Reference 33 details the accuracy and limitations of the accelerometer aboard the CHAMP spacecraft and addresses issues with instrumental bias, scale factors, various modeling approaches, and density retrieval issues. The study analyzed data over the course of 21 months, and accumulated 1.2 million observations spanning all manner of solar and geomagnetic activity. Overall information about CHAMP, its STAR accelerometer, and mission profile in general are also contained in Reference 33.

Reference 34 contains additional information related to the derivation of atmospheric densities from the CHAMP satellite. Calibration of accelerometer bias and scale factors, including variation in time is made using available GPS data for the positioning of CHAMP. Winds in the thermosphere were assumed to have a negligible effect on perceived atmospheric density, and the accuracy of measurements from CHAMP was judged to be largely due to uncertainty in calibration, as well as negligible winds. In this study, time periods near three geomagnetic storms are

examined and compared against results obtained from semi-empirical models to illustrate limitations within the models.

Reference 2 examines polar region density variations in the thermosphere through the use of the CHAMP accelerometers. The study found significant structures with amplitudes of up to 50% above ambient densities located primarily around the polar cusp region which bottomed out nearer to the poles. Energetic solar particles were funneled by the earths magnetic field towards the poles where the energy was deposited and caused temperature and density variations. These effects have such short temporal resolution that it is highly improbable other methods of determining atmospheric density would catch these variations.

The accelerometer aboard the CHAMP satellite has been used to observe numerous solar and geomagnetic events, as well as their ability to cause significant density variations in the thermosphere [Ref. 1, 34-38]. As mentioned above for polar variations, the accelerometer aboard CHAMP is much better able to observe short term density variations than existing empirical and analytical models that lack the temporal resolution required to observe these events. The accelerometer measured rapid density variations generating density waves that propagate towards the poles arising from these storms. CHAMP and GRACE are uniquely suited to the task of identifying these variations' amplitude and span due to the presence of their accelerometers, and their near polar orbits, which allow the satellites opportunities to observe almost all latitudes of the atmosphere.

Reference 39 details the methods through which atmospheric densities may be derived from the GRACE satellites. Densities derived from the GRACE satellites' accelerometers have similar properties and drawbacks to the accelerometer aboard the CHAMP spacecraft, but the satellites orbit at higher altitudes.

Recently, the STAR accelerometer aboard CHAMP has been used to model moderate and large scale density variations in the thermosphere [Ref 40]. Density variations often generate waves that originate at high latitudes and then progress to lower latitudes. Typically, these waves dissipate at mid-range latitudes, however, the waves tend to take longer to dissipate if geomagnetic activity is high, and solar flux is low. When coronal mass ejections (CME) impinge the atmosphere during these conditions, travelling atmospheric disturbances (TAD) may be observed [Ref 41]. These TADs are difficult to observe on the lit side of the earth, but are much more observable on the dark side of the earth. These TADs can be observed along with their relative magnitude, span, and speed using accelerometer data from CHAMP as they propagate away from the poles. Reference 42 used the STAR accelerometer to model corrections for the NRLMSISE model during geomagnetic storms.

The CHAMP and GRACE satellites are invaluable tools for examining the nature of the earth's atmosphere through the use of their accelerometers, and their availability of both GPS and SLR data for the satellites. Unfortunately, these three satellites suffer from very poor spatial coverage as compared to DCA techniques which may have upwards of 700 satellites supplying data.

1.6.3 Additional Approaches

Use of GPS receivers, or SLR range observations to estimate non-conservative accelerations has been examined in several papers thus far. One technique is to use the standard DCA approach to the limited number of satellites that have POE data available, and use these results to modify existing models [Ref. 43]. Calibrating atmospheric models to better match data from higher accuracy readings, such as those from POEs, will lead to significant increases in accuracy of orbit determination. Reference 43 aims to use both high accuracy data, and highly available though less accurate data to create model corrections that have increases in both spatial and temporal resolution.

GPS accelerometry is an additional approach wherein GPS receiver data is used to estimate accelerations due to non-conservative forces [Ref. 46-45]. GPS accelerometry uses precision orbit data to derive forces experienced by the satellite via drag. These forces can then be used to determine atmospheric density. Via this method, temporal resolutions of 20 minutes can be obtained for CHAMP data in both the along-track and cross-track directions. With the launch of GRACE, a highly accurate model of the earth's gravitational field exists, and fulfils GPS accelerometry's need for such an accurate model. GPS accelerometry is most accurate in the along-track direction, which is where the bulk of non-conservative forces are experienced due to drag and station-keeping maneuvers. The technique lacks the precision of accelerometer readings, but several additional missions utilizing GPS

receivers are planned, which will increase the data pool from which to pull observations, and increase the spatial resolution achievable.

Reference 47 uses both batch and Kalman filter techniques to examine accelerations experienced by the GRACE-B satellite. Both approaches are highly accurate, with a resolution of 5 cm with dual frequency data, and 10 cm with single frequency data. The primary point of this study was to determine differences between filter/smoother techniques, and bath techniques. The study found that the extended Kalman filter/smoother is less expensive computationally, while the batch least-squares estimator is smoother and more robust during data gaps.

Reference 48 uses Doppler Orbitography and Radio positioning Integrated by Satellite (DORIS), as well as SLR data to examine density variations in the thermosphere during periods of enhanced geomagnetic activity. The study analyzed satellites at varied altitudes from the 800-900 km range, to the 1300-1400 km range. Significant errors were found to exist for the considered atmospheric models; these errors were greatly improved with more enhanced data processing. DORIS is yet another way of obtaining highly accurate satellite state vectors, and allows for formulation of corrections to atmospheric density models.

1.7 Current Research on Atmospheric Density Model Corrections

This research aimed to combine highly accurate data in the form of precision orbit data with large spatial coverage from a myriad of satellites to better correct atmospheric density models. The research will examine what improvements can be made in both spatial and temporal resolution by using readily available GPS data.

The GPS data is merged with an optimal orbit determination process to achieve a high degree of accuracy in satellite observations ranging from the cm level to the meter level. For this research, POE data is used in conjunction with the aforementioned optimal orbit determination scheme to examine periods during which solar and geomagnetic activity vary greatly, where highly localized density increases were found in previous work, and when large moving variations were observed in the past. Results are compared against CHAMP and GRACE accelerometer data in an effort to compare the derived densities to the true densities derived from accelerometer data.

Some of the initial results, as well as the research leading up to this research are detailed in References 49-51. In Reference 49, derived neutral densities were checked for consistency in overlap periods between data sets. The sets typically have a two hour overlap at the beginning and end of each set of measurements. In the overlap areas, density variations were at worst 10%. When compared to accelerometer data from CHAMP, the derived densities exhibited a similar range of errors [Ref. 50].

Reference 59 examined the viability of using optimal orbit determination processes to model atmospheric density during a range of geomagnetic and solar activity levels by comparing derived densities to accelerometer densities. The study spanned numerous time periods, and input variables such as density and ballistic coefficient half-life were varied to study their effects on estimated densities. The accuracy of varying the input parameters was measured using the cross-correlation between the derived densities and the accelerometer derived densities [Ref. 59]. This

provided a quantitative measure of which variant of input parameters yielded the best results.

1.8 Gauss-Markov Process

A Gauss-Markov process is often used to resolve difficulties that arise from unmodeled or inaccurately modeled forces that may unexpectedly act on the spacecraft. A Gauss-Markov process is introduced to the data to compensate for these forces as a source of process noise. A Gauss-Markov process, as the name suggests, conforms to the properties of both a Gaussian, or normal, distribution, and a Markov process in that the probability density function is solely dependent on the observation immediately preceding it, and not upon any observations earlier than the one immediately preceding it. A more detailed explanation of Gauss-Markov processes is available in Reference 53.

1.9 Estimating Density and Ballistic Coefficient Separately

In the course of dealing with satellite drag, atmospheric density and ballistic coefficient are directly related through the drag equation. Separation of the two variables is difficult in an orbit determination process due to the obvious difficulty of having one equation, and two unknowns. A technique in References 54 and 55 proposes a method of estimating both parameters in real time.

Before a viable manner in which to separate the ballistic coefficient and the atmospheric density was formulated, ballistic coefficient estimates tended to absorb errors in both the density and ballistic coefficient models. The method by which both

are estimated simultaneously involves the two variables having markedly differing half-lives applied to the Gauss-Markov process. These exponential half-lives instruct the process to what degree it should consider previous measurements when inputting process noise. The analysis software used in this research, the Orbit Determination Tool Kit (ODTK), allows the user to manipulate both half-lives, which allows the user to examine the effectiveness of varying those two parameters. More information on this can be found in Reference 53.

1.10 Travelling Atmospheric Disturbances (TAD)

During the period of April 15-24, 2002 several coronal mass ejections (CME) were observed emanating from the Sun, coming into contact with the atmosphere and generating geomagnetic storms [Ref. 1]. These CMEs impinged the atmosphere and channeled energy into the upper atmosphere near the poles causing large localized density increases. These density increases propagated towards the equator, becoming travelling atmospheric disturbances (TAD), in a wave like fashion, with constructive interference occurring near the equator where the two waves propagating from opposing poles interacted. These TADs were pronounced enough that they propagated past the opposing pole, and again towards their poles of origin; though, this effect is much less discernable than the initial waves.

The density increases likely existed on both the lit and unlit sides of the Earth; however, they are much more apparent on the unlit side of the Earth where they are more easily separated from global density values. On the lit side of the Earth,

atmospheric heating due to the Sun causes observation of these TADS to become more difficult.

1.11 Geomagnetic Cusp Features

Using the STAR instrument aboard CHAMP, localized increases in thermospheric density were observed around the geomagnetic poles. These localized densities demonstrated increases of up to 50% from ambient densities [Ref. 2]. The densities around the geomagnetic poles showed this increase around 75^{o} geomagnetic latitude, with a basin localized around the actual geomagnetic pole. The exact process that results in these increases is still not readily apparent; though it is thought that Joule heating and the interaction of magnetic field lines is responsible for a portion of the density increase [Ref. 2].

1.12 Examined Satellites

1.12.1 CHAMP

The CHAMP satellite, as seen in Figure 1.1 was launched on July 15, 2000 with a scheduled mission life of 5 years to generate highly precise gravity and magnetic field measurements [Ref. 56]. CHAMP was specifically designed to measure the medium wavelength gravity field, map Earth's global magnetic field, and perform atmosphere/ionosphere sounding. The CHAMP satellite possesses the highly accurate Spatial Triaxial Accelerometer for Research (STAR) instrument which was used in this study to determine atmospheric density [Ref. 56].

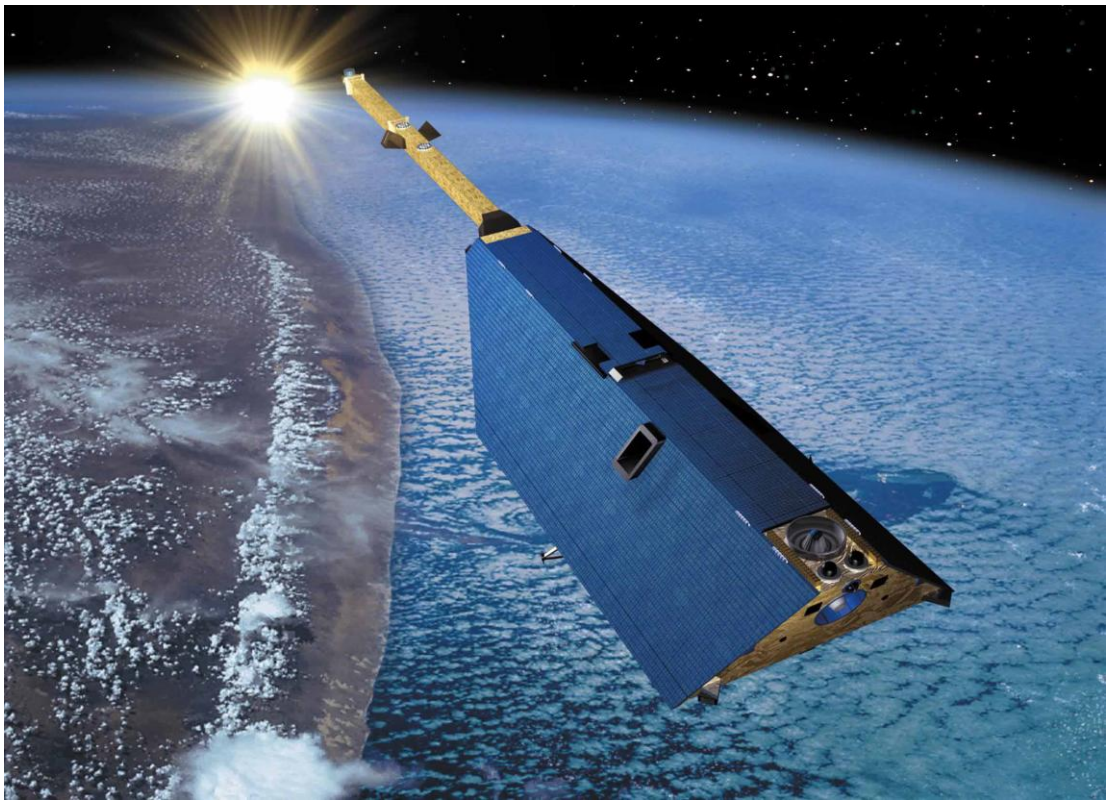

Figure 1.1: Artist Rendering of the CHAMP Satellite in Orbit

1.12.2 GRACE

The GRACE project, as seen in Figure 1.2 is a small network of two satellites designed to measure the Earth's magnetic field very precisely. To accomplish this goal, both satellites are also equipped with very sensitive accelerometers, as well as a satellite ranging system that allows the satellites to measure very small perturbations in the distance between them [Ref. 57]. The perturbations arise when one of the satellites passes over a region of the Earth that is more or less dense than the Earth as a whole, causing that satellite to either accelerate or decelerate and alter the distance between them [Ref. 57]. The accelerometers aboard these two spacecraft were used to analyze corrected densities found in this research.

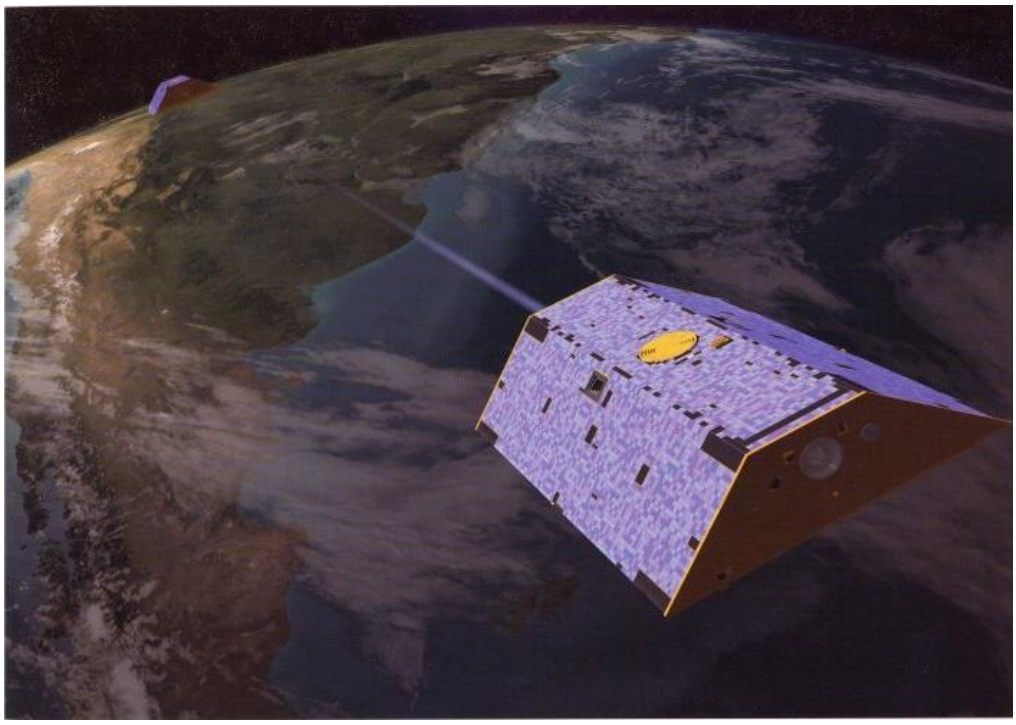

Figure 1.2: Artist Rendering of the GRACE Satellites in Orbit

1.12.3 TerraSAR-X

The TerraSAR-X satellite, as seen in Figure 1.3, is a German satellite designed to perform radar based Earth observations, and unlike the CHAMP and GRACE satellites, the TerraSAR-X does not possess an accelerometer. The TerraSAR-X was launched from the Baikonur Cosmodrome in Kazakhstan on June 15th, 2007 [Ref. 58]. The orbits for the TerraSAR-X satellite were examined for the period of September 21-30, 2007, and compared to results for the same time period for the CHAMP and GRACE satellites.

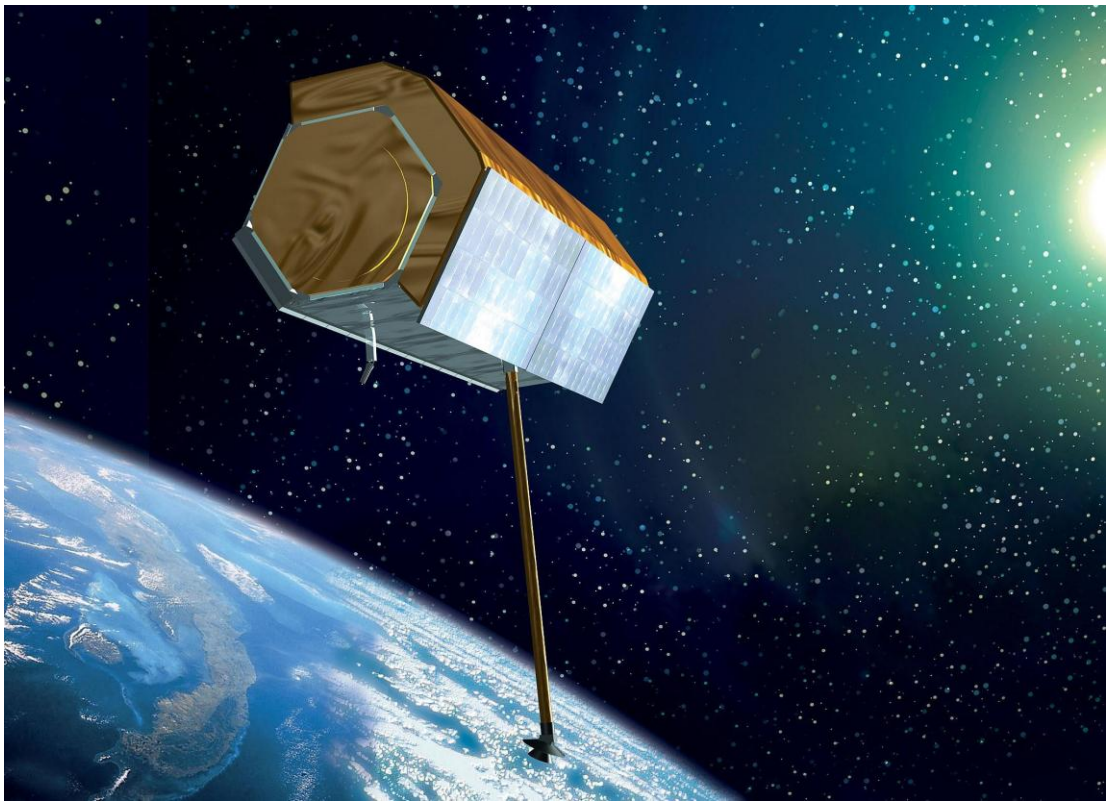

Figure 1.3: Artist Rendering of the TerraSAR-X Satellite in Orbit

2 Methodology

This section details the methods used to obtain results for determining the atmospheric density in the thermosphere. Position and velocity vectors were derived from Precision Orbit Ephemerides (POE) for the CHAMP and GRACE satellites in an optimal determination process. The optimal orbit determination process yielded density values along the path of the satellite, as well as ballistic coefficient values for the satellite during that time. Varyious orbit determination schemes were examined to determine the relative accuracy of the atmospheric density corrections by assuming accelerometer derived densities as truth. The effects of varying density correlation half-life, ballistic coefficient correlation half-life, and baseline density models are examined to find which corrected models best characterize the atmosphere in both long and short term solutions.

2.1 Precision Orbit Ephemerides

POE data is currently available for both the CHAMP and GRACE satellites in the form of Precision Science Orbits (PSO) or Rapid Science Orbits (RSO). This data is available from Helmholtz Centre Potsdam at their website at http://isdc.gfz-potsdam.de. Processing and accuracy details of RSOs can be found in References 60-63. Accuracies for RSOs vary from 5-10 cm for most of the mission lives of the satellites, though early in the mission lives, accuracies were as poor as 25 cm. There is no published data for the accuracies of PSOs, though, as PSOs incorporate additional gravity field solutions obtained from CHAMP, these solutions are assumed

at least as accurate, and likely more accurate than RSOs. For this reason, PSO data is preferred over RSO data when available. PSO data is unavailable for dates prior to 2003 and after 2005, and none are available for the GRACE or TerraSAR-X satellites.

2.2 Optimal Orbit Determination

An optimal orbit determination scheme is used to determine atmospheric densities in the thermosphere. The process for utilizing an optimal orbit determination scheme is detailed in Reference 53, with additional information contained in References 5 and 64.

Orbit determination is the process of estimating orbits in relation to the central body provided accurate measurements are available. Orbiting bodies can be effected by several forces, predominately geopotential, and third-body gravitational accelerations, as well as forces due to pressures acting on the surface areas of the satellites. Artificial satellites tend to have increased sensitivity to pressure effects such as drag, solar radiation pressure (SRP), and earth albedo. This is due to the decreased density of artificial satellites as opposed to natural satellites which are generally solid throughout.

Each measurement used in an orbit determination is preferred to possess sufficient orbit parameters to predict the future state of the satellite. This requires that six independent elements of the state be known. In Cartesian coordinates, these are the position and velocity vectors; in Keplerian elements, these are eccentricity (e), semimajor axis (a), inclination (i), longitude of the ascending node (Ω), argument of

periapsis (ω), and either mean anomaly (M) or true anomaly (ν) [Ref. 5]. The general state at time t is denoted as $\mathbf{X}(t)$, and the orbit determination problem can be stated as: If at an initial time t_0, the state $\mathbf{X}_0$ of a satellite following a ballistic trajectory is known, then equations of motion can be integrated to give the state of the vehicle at any time [Ref. 53]. Unfortunately, the initial state of the orbiting body is not precisely known, and the dynamical models are also not precisely known. This causes the path of the orbiting body to deviate from the predicted path. For this reason, updated measurements are required for better approximating the true trajectory of the orbiting body, though the trajectory cannot be precisely known due to random and systematic errors. Measurements are generally in the form of range, range-rate, azimuth, elevation, and other observable quantities that often must be used to determine more useful state variables, as these measurements are often nonlinear functions of the desired state variables [Ref. 53].

In this research, as well as the research leading up to it, POE data were used as measurements in the optimal orbit determination scheme. These POEs provided relatively accurate measurements for use as input for a Kalman filter/smoother scheme using a Gauss-Markov processes, both of these concepts will be described in greater detail later in the section.

There is ongoing debate over the "best" method to determine orbit characteristics. Some methods compile results more quickly, though at the risk of reduced accuracy. Some methods are able to take into account each observation as it is observed, while others require all measurements to be accumulated.

According to Reference 65 any orbit determination scheme may be referred to as optimal if the following criteria are met:

1. *"Sequential processing is used to account for force modeling errors and measurement information in the time order in which they are realized.*
2. *The optimal state error estimate* $\Delta\hat{X}$ *is the expectation of the state error* ΔX *given the measurement residual* Δy. *That is:* $\Delta\hat{X} = E\ \Delta X \mid \Delta y$. *This is Sherman's Theorem.*
3. *Linearization of state estimate time transition and state to measurement representation is local in time, not global.*
4. *The state estimate structure is complete.*
5. *All state estimate models and state estimate error model approximations are derived from appropriate force modeling physics, and measurement sensor performance.*
6. *All measurement models and measurement error model approximations are derived from appropriate sensor hardware definition and associated physics, and measurement sensor performance.*
7. *Necessary conditions for real data:*
    - *Measurement residuals approximate Gaussian white noise.*

- *McReynolds' filter-smoother consistency test is satisfied with probability 0.99.*

8. *Sufficient conditions for simulated data: The state estimate errors agree with the state estimate error covariance function.*

The first six requirements defined standards for optimal algorithm design, and the creation of a realistic state estimate error covariance function. The last two requirements enable validation: They define realizable test criteria for optimality. The last requirement implies the development and use of a physically realistic measurement simulator."

2.3 Gauss-Markov Process Half-Lives

Gauss-Markov processes are introduced into the orbit determination scheme in ODTK through the use of the density and ballistic coefficient correlation half lives. These half lives are expressed as ratios of the corrections as compared to the calculated values using the CIRA 1972 model in the form of $\Delta\rho/\rho$ and $\Delta B/B$, which represent the amount of time required for the estimated correction to the corresponding values to decay to half its original value [Ref. 66].

The ODTK help file [Ref. 66] details how these variables are incorporated into Gauss-Markov processes. To examine this, let a random scalar variable be denoted by $x=x(t_k)$, in this case, that random scalar variable is either density or ballistic coefficient. The variable satisfies the equation:

$$x\ t_{k+1}\ = \Phi\ t_{k+1}, t_k\ \ x\ t_k\ + \sqrt{1-\Phi^2\ t_{k+1}, t_k}\ w\ t_k \tag{2.1}$$

where *w(t)* is a Gaussian variable with a fixed standard deviation and a zero mean. Since *w(t)* in this equation is solely dependent on the previous measurement, the *w(t)* process is also Markovian. The initial value of the Gauss-Markov process is equal to the initial value of the scalar variable being examined, and the transfer function is defined as:

$$\Phi\ t_{k+1}, t_k\ = e^{\alpha |t_{k+1} - t_k|} \tag{2.2}$$

where

$$\alpha = \frac{\ln(.5)}{\tau} \tag{2.3}$$

and τ is the user supplied half life for the given variable [Ref. 66].

2.4 Filter-Smoother Description

Precision orbit ephemerides were input as measurements into a sequential filtering scheme that estimates a series of state variables including position and velocity vectors, density corrections, spacecraft ballistic coefficient corrections, as well as other variables of interest such as station biases, additional forces, measurements, and model parameters. The filter process takes previous measurements into account to integrate force models and determine the future state of orbiting bodies. The filter outputs a converged state and covariance estimate that are later used in the following iterations of the filter approach.

The smoother process takes the last output of the filtering process and works sequentially backwards to the initialization state of the filter. The smoother's output is determined by inputting the series of outputs from the filtering scheme. None of the initial measurements used in the determination of the filter solutions are used for the smoother process. The smoother is applied to take into account all files that are included in the measurements [Ref. 53]. Detailed explanations and algorithms for filter and smoother schemes can be found predominately in Reference 53, with supplemental information in References 5, 64, 65, and 67.

2.5 McReynolds' Filter-Smoother Consistency Test

The McReynolds's Filter-Smoother consistency test is used to test the validity of the filter and smoother state estimations by comparing them to one another. The test consists as follows; a dimensionless ratio, $\dot{R}$, is formed from the difference between the smoother and filter values compared to the square root of the difference between the two covariance matrices. The test is gauged as passed if 99% or more of the ratios are less than 3.

$$R = \left| \frac{\dot{X}_{i,\,filter} - \dot{X}_{i,smoother}}{\sigma_i} \right| \leq 3 \tag{2.4}$$

$$\sigma_i = \sqrt{\bar{P}_{i,\,filter} - \bar{P}_{i,smoother}} \tag{2.5}$$

The McReynolds's consistency test is further detailed in Reference 65.

2.6 Using Orbit Determination to Estimate Atmospheric Density

The orbits estimated using ODTK are optimal in the least-squares, or minimum variance sense. ODTK's sequential filtering scheme estimates corrections to baseline atmospheric density models and ballistic coefficients for the satellites, calculates residuals, conducts position and velocity consistency tests, generates state variables, and estimates other state parameters of interest. A smoother was then applied to the filtered data in order to take into account all measurements in the determination of these parameters and increase the accuracy of the estimations. The filter/smoother scheme estimates atmospheric density corrections, and ballistic coefficient corrections, including covariance matrices determined by the physics models associated with the orbit determination scheme. ODTK is able to estimate corrections to a variety of baseline atmospheric density models, including Jacchia-1971, CIRA-1972, Jacchia-Roberts, MSISE-1990, and NRLMSISE-2000 models. ODTK used the GRACE Gravity Model GGM02C to integrate the equations of motion for the satellite, which is complete to the 200^{th} degree, and incorporates GRACE satellite data, as well as terrestrial gravity information [Ref. 57]. ODTK also includes additional force models in addition to drag, these models include a complex assessment of the Earth's gravity field, solar, Earth infrared, and Earth albedo radiation pressure, lunar and solar gravitational effects, general relativity, and ocean and solid Earth tides.

Results for estimating the atmospheric density are expected to clump into two groups divided by baseline atmospheric density model. The first group is expected to consist of the Jacchia-1971, Jacchia-Roberts, and CIRA-1972 models due to the models being based on the Jacchia-1970 model with slight improvements. The second grouping was expected to consist of the MSISE-1990 and NRLMSISE-2000 models which are both Mass Spectrometer Incoherent Scatter Extended models.

There are two corrections to atmospheric density that are applied in ODTK, the first takes place as a global correction to density based upon the daily $F_{10.7}$ value, the daily A_p value, and the height of perigee of the satellite orbit. These corrections are then propagated through the orbit through the use of exponential Gauss-Markov processes; a transformation is applied to relate the current corrections for atmospheric density to the corrections determined at perigee. The second correction is used to account for each sequential observation of the satellite, as well as more up to date information of current atmospheric conditions. The sequential process allows for corrections to be estimated as each observation is acquired. These sequential measurements take into account the user provided density and ballistic coefficient exponential Gauss-Markov process half-lives.

Ballistic coefficient is estimated as part of the filter/smoother process, and is defined in ODTK for CHAMP as having a nominal value of 0.00444 m^2/kg for 2002-2003 and 0.00436 m^2/kg for 2004-2005 [Ref. 67]. The nominal value for CHAMP's BC changes due to the changing mass of the satellite through station keeping maneuvers, as well as the decaying orbit of CHAMP. Values for the CHAMP

satellite's nominal ballistic coefficient that were not included in these ranges were extrapolated to years both preceding and following these ranges by taking into account the changing mass of the satellite. The nominal ballistic coefficient for GRACE is defined as 0.00687 m^2/kg in the ODTK orbit determination scheme [Ref. 67]. The nominal ballistic coefficient of GRACE is less variable than that of CHAMP due to the GRACE satellites' lack of station keeping maneuvers. The GRACE satellites were launched with no intention of raising their orbit [Ref. 57].

Five different independent variables were examined for their effects on the accuracy and precision of these atmospheric corrections: baseline density model, density correlation half-life, ballistic coefficient correlation half-life, geomagnetic activity level, and solar activity level.

2.6.1 Varying Baseline Density Model

The five baseline models are examined to determine which model interacts with the orbit determination scheme to obtain the best results. More detailed descriptions of these models can be found in Section 1.5.

2.6.2 Varying Density and Ballistic Coefficient Correlated Half-Lives

Solutions were found for the following dates in Tables 2.1-2.6, these dates encompass a range of dates from differing periods in the solar cycle, differing periods in the Earth's orbit, and differing levels of geomagnetic and solar activity. The tables give the initial date for the time period in question, the initial time during that day, the duration of the scenario, and the A_p and $F_{10.7}$ values for the scenario. The A_p and $F_{10.7}$

values were time averaged for scenarios that span multiple days. The density and ballistic coefficient exponential Gauss-Markov process half-lives are varied by orders of magnitude in variations of 1.8 minutes, 18 minutes, and 180 minutes for each of the two half-lives resulting in 9 cases for each baseline density model, or 45 cases total. Reference 59 examined higher values for the density and ballistic coefficient correlation half-lives, but higher values invariably fared worse than iterations involving half-lives of shorter duration.

Table 2.1: Dates of Available CHAMP Data and Corresponding Geomagnetic and Solar Activity for 2001

Year	Month	Day	t_i (hr)	span (min)	A_p	$F_{10.7}$
2001	Jun	17	22	840	6.75	224.18
2001	Jun	18	10	840	61.3	235.2
2001	Jun	18	22	840	49	208.4
2001	Jun	19	10	840	16.3	200.88
2001	Jun	19	22	840	19	204.18
2001	Jul	20	10	840	17.3	204.53
2001	Jul	27	22	840	9	120.53
2001	Jul	28	10	840	3.75	118.63
2001	Jul	28	22	840	3.75	120.13
2001	Jul	29	10	840	7.75	121.13
2001	Jul	29	22	840	7.75	118.63
2001	Jul	30	10	840	12	117.43

Year	Month	Day	t_i (hr)	span (min)	A_p	$F_{10.7}$
2001	Oct	1	22	840	81	205.1
2001	Oct	2	10	840	85	203.4
2001	Oct	2	22	840	91	194.1
2001	Oct	3	10	840	122	193.1
2001	Oct	22	0	720	152	230.4
2001	Oct	22	10	840	150	232
2001	Nov	5	22	840	32	232.6
2001	Nov	6	10	840	134	225.5

Table 2.2: Dates of Available CHAMP Data and Corresponding Geomagnetic and Solar Activity for 2002

Year	Month	Day	t_i (hr)	span (min)	A_p	$F_{10.7}$
2002	Feb	17	0	2160	32.4	191.02
2002	Feb	18	12	2160	22.3	188.17
2002	Feb	19	0	2160	21.9	191.17
2002	Apr	15	0	1440	7	203.3
2002	Apr	16	0	1440	62	195.7
2002	Apr	17	0	1440	63	193.5
2002	Apr	19	0	1440	70	179.7
2002	Apr	20	0	1440	70	177.3
2002	Apr	23	0	1440	27	176.9
2002	May	16	22	840	10.5	161.03
2002	May	17	10	840	8.5	159.18
2002	May	17	22	840	6.5	165.28
2002	May	18	10	840	26.3	164.75
2002	May	18	22	840	26.3	172.95
2002	May	19	10	840	10.3	174.9
2002	May	19	22	840	20.3	175.3
2002	May	20	10	840	16.5	171.65
2002	May	20	22	840	16.3	186.65
2002	May	21	10	840	14.5	191.6
2002	May	21	22	840	17.8	186.8
2002	May	22	10	840	12.3	185.8
2002	May	22	22	840	11	185
2002	May	23	10	840	150	182.53
2002	Aug	17	0	720	39.6	232.3
2002	Aug	17	10	840	12.3	228.65
2002	Aug	17	22	840	13.8	243.25
2002	Aug	18	10	840	33.8	247.98
2002	Aug	18	22	840	38	243.68
2002	Aug	19	10	840	44.5	245.05
2002	Aug	19	22	840	51	235.25
2002	Aug	20	10	840	49	234.75
2002	Aug	20	22	840	54.5	226.95
2002	Aug	21	10	840	35	224.98
2002	Aug	21	22	840	53.3	225.08
2002	Aug	22	10	840	8.8	224
2002	Aug	22	22	840	13	228.4
2002	Aug	23	10	840	11	236.9
2002	Sep	6	22	840	9.8	184.4
2002	Sep	7	10	840	108	183.4
2002	Sep	30	22	840	40	140.1
2002	Oct	1	10	840	130	141.1
2002	Oct	1	22	840	69	137
2002	Oct	2	10	840	35	133.5
2002	Oct	3	22	840	73	154.7
2002	Oct	4	10	840	74	158.2
2002	Oct	23	22	840	14	159.4
2002	Oct	24	10	840	98	155.4
2002	Nov	20	22	840	43	149.2
2002	Nov	21	10	840	77	147.6
2002	Dec	6	0	720	41	143.9
2002	Dec	6	10	840	15	143.2
2002	Dec	6	22	840	14	145.9
2002	Dec	7	10	840	27	145.8
2002	Dec	16	22	840	8	203.5
2002	Dec	17	10	840	3	209.6
2002	Dec	17	22	840	4.8	194.4
2002	Dec	18	10	840	4.5	191.6
2002	Dec	18	22	840	4	187.7
2002	Dec	19	10	840	42	185.8
2002	Dec	19	22	840	36	189.4
2002	Dec	20	10	840	31	193.4
2002	Dec	20	22	840	33	181
2002	Dec	21	10	840	14	180.8
2002	Dec	21	22	840	37	169.3
2002	Dec	22	10	840	17	169.6
2002	Dec	22	22	840	14	156.9
2002	Dec	23	10	840	39	156.5

Table 2.3: Dates of Available CHAMP Data and Corresponding Geomagnetic and Solar Activity for 2003

Year	Month	Day	t_i (hr)	span (min)	A_p	$F_{10.7}$
2003	Jan	4	0	720	64.8	138.2
2003	Jan	4	10	840	15.3	136.95
2003	Jan	4	22	840	28.5	141.95
2003	Jan	5	10	840	11	139.8
2003	Jan	5	22	840	10.5	153.4
2003	Jan	6	10	840	6.75	156.55
2003	Jan	6	22	840	6.25	157.55
2003	Jan	7	10	840	9.25	155.25
2003	Jan	7	22	840	10	165.45
2003	Jan	8	10	840	5.5	165.78
2003	Jan	8	22	840	6.25	174.68
2003	Jan	9	10	840	5.25	176.45
2003	Feb	1	22	840	24.8	122.78
2003	Feb	2	10	840	76.3	121.58
2003	Mar	19	0	720	55.2	107.2
2003	Mar	19	10	840	13.8	109.85
2003	Mar	19	22	840	20.5	99.25
2003	Mar	20	10	840	45.5	98.175
2003	Mar	20	22	840	31.8	91.875
2003	Mar	21	10	840	42.5	90.8
2003	Mar	21	22	840	54	88.8
2003	Mar	22	10	840	21.3	87.275
2003	Mar	22	22	840	29.3	91.375
2003	Mar	23	10	840	35.5	91.175
2003	Mar	23	22	840	36.5	96.075
2003	Mar	24	10	840	7.25	94.575
2003	May	28	22	840	54.8	139.63
2003	May	29	10	840	205	146.9
2003	May	29	22	840	140	125.7
2003	May	30	10	840	64.8	121.43
2003	Jun	17	22	840	73.5	124.68
2003	Jun	18	10	840	90.8	123.68
2003	Jul	10	22	840	10.3	126.3
2003	Jul	11	10	840	94	126.3
2003	Aug	17	22	840	24	119.6
2003	Aug	18	10	840	176	118.5
2003	Aug	20	22	840	26	120.1
2003	Aug	21	10	840	99	121.6
2003	Sep	11	22	840	24	96.2
2003	Sep	12	10	840	12	95.18
2003	Sep	12	22	840	15	96.88
2003	Sep	13	10	840	8	97.68
2003	Sep	13	22	840	15	96.18
2003	Sep	14	10	840	6.8	95.15
2003	Sep	14	22	840	6.3	97.75
2003	Sep	15	10	840	6.8	97.9
2003	Sep	15	22	840	7.3	99.9
2003	Sep	16	10	840	51	98.75
2003	Sep	16	22	840	43	105.4
2003	Sep	17	10	840	111	106.2
2003	Oct	13	22	840	26	92.43
2003	Oct	14	10	840	122	91.05
2003	Oct	28	22	840	204	279.1
2003	Oct	29	10	840	204	279.1
2003	Oct	29	22	840	204	279.1
2003	Oct	30	10	840	191	271.4
2003	Oct	30	22	840	191	271.4
2003	Oct	31	10	840	116	248.9
2003	Oct	31	22	840	116	248.9
2003	Nov	1	10	840	26	210.4
2003	Nov	10	22	840	42	93.48
2003	Nov	11	10	840	91	92.95
2003	Nov	12	22	840	42	99.18
2003	Nov	13	10	840	92	100.8
2003	Nov	20	0	2880	150	177

Table 2.4: Dates of Available CHAMP Data and Corresponding Geomagnetic and Solar Activity for 2004

Year	Month	Day	t_i (hr)	span (min)	A_p	$F_{10.7}$
2004	Jan	15	22	840	22	116.1
2004	Jan	16	10	840	43.3	115.85
2004	Jan	16	22	840	42.3	118.05
2004	Jan	17	10	840	28.5	119.35
2004	Jan	17	22	840	30	116.35
2004	Jan	18	10	840	29	111.93
2004	Jan	18	22	840	32.3	126.63
2004	Jan	19	10	840	28.8	131.68
2004	Jan	19	22	840	22	126.18
2004	Jan	20	10	840	27	124.5
2004	Jan	20	22	840	23.5	125.7
2004	Jan	21	10	840	22.8	128.03
2004	Jan	21	22	840	22	119.93
2004	Jan	22	10	840	103	119.48
2004	Jul	18	22	840	14	153.4
2004	Jul	19	10	840	15.8	152.58
2004	Jul	19	22	840	39.8	158.68
2004	Jul	20	10	840	8.25	156.3
2004	Jul	20	22	840	9.25	171.9
2004	Jul	21	10	840	12.8	174.55
2004	Jul	21	22	840	11.3	179.55
2004	Jul	22	10	840	13	181.58
2004	Jul	22	22	840	11.8	178.48
2004	Jul	23	10	840	4.5	177.53
2004	Jul	23	22	840	5.8	178.2
2004	Jul	24	10	840	61	180.4
2004	Jul	24	22	840	52	172.4
2004	Jul	25	10	840	70	175.1
2004	Jul	26	22	840	41	145.9
2004	Jul	27	10	840	236	146.9
2004	Oct	31	22	840	17	134.3
2004	Nov	1	10	840	6.3	134
2004	Nov	1	22	840	7.8	131.6
2004	Nov	2	10	840	7.3	130.3
2004	Nov	2	22	840	5.8	133
2004	Nov	3	10	840	20	133.7
2004	Nov	3	22	840	17	133.7
2004	Nov	4	10	840	11	132.4
2004	Nov	4	22	840	14	137.5
2004	Nov	5	10	840	2.5	141.9
2004	Nov	5	22	840	6.8	129.6
2004	Nov	6	10	840	1.8	126.3
2004	Nov	6	22	840	1.3	127
2004	Nov	7	10	840	94	128.6
2004	Nov	7	22	840	86	123.1
2004	Nov	8	10	840	129	117.6
2004	Nov	8	22	840	264	134
2004	Nov	9	10	840	201	147

Table 2.5: Dates of Available CHAMP Data and Corresponding Geomagnetic and Solar Activity for 2005

Year	Month	Day	t_i (hr)	span (min)	A_p	$F_{10.7}$
2005	Jan	16	22	840	23.3	134.78
2005	Jan	17	10	840	95.5	136.3
2005	Jan	17	22	840	68.5	123.5
2005	Jan	18	10	840	118	118.3
2005	Jan	18	22	840	140	126.3
2005	Jan	19	10	840	76.3	130.68
2005	Jan	20	22	840	17	112.13
2005	Jan	21	10	840	126	112.6
2005	Mar	11	0	720	26.2	103.6
2005	Mar	11	10	840	5.5	102.3
2005	Mar	11	22	840	8.25	107.5
2005	Mar	12	10	840	4.25	107.88
2005	Mar	12	22	840	5.25	111.58
2005	Mar	13	10	840	9.5	113.05
2005	Mar	13	22	840	8.75	110.85
2005	Mar	14	10	840	23.5	111.13
2005	Mar	14	22	840	25.5	107.83
2005	Mar	15	10	840	4.75	107.85
2005	Mar	15	22	840	6.75	104.45
2005	Mar	16	10	840	11.3	104.4
2005	Mar	16	22	840	7	101.2
2005	Mar	17	10	840	17	101.58
2005	Mar	17	22	840	16.8	96.875
2005	Mar	18	10	840	18.5	96.575
2005	Mar	18	22	840	18	93.075
2005	Mar	19	10	840	5.75	93.175
2005	Mar	19	22	840	21	89.275
2005	Mar	20	10	840	5	88.1
2005	Apr	4	22	840	41.8	87.6
2005	Apr	5	10	840	38.3	88.575
2005	May	7	22	840	16.3	102.85
2005	May	8	10	840	149	100.95
2005	May	8	22	840	79	109.95
2005	May	9	10	840	13.5	109.85
2005	May	9	22	840	17.3	119.25
2005	May	10	10	840	9.5	120.03
2005	May	10	22	840	11.8	126.33
2005	May	11	10	840	23	129.9
2005	May	11	22	840	17	121.9
2005	May	12	10	840	21	117.7
2005	May	12	22	840	23	126.4
2005	May	13	10	840	26	135.3
2005	May	15	10	840	87	103
2005	May	29	22	840	36	96.95
2005	May	30	10	840	168	97.13
2005	Jun	11	22	840	6.8	107.6
2005	Jun	12	10	840	105	109.2
2005	Jun	22	22	840	8.8	80.6
2005	Jun	23	10	840	83	80.33
2005	Jul	9	22	840	28	106.5
2005	Jul	10	10	840	99	107.4
2005	Aug	23	22	840	9	102.9
2005	Aug	24	10	840	196	102.3
2005	Sep	10	22	840	43	112.7
2005	Sep	11	10	840	145	109
2005	Sep	11	22	840	155	117.4
2005	Sep	12	10	840	133	120.6
2005	Sep	14	22	840	25	119.9
2005	Sep	15	10	840	52	119.4
2005	Oct	23	22	840	14	73.55
2005	Oct	24	10	840	3.3	73.63
2005	Oct	24	22	840	3.3	72.73
2005	Oct	25	10	840	6.5	72.6
2005	Oct	25	22	840	5	72.2
2005	Oct	26	10	840	28	72.33
2005	Oct	26	22	840	36	71.43
2005	Oct	27	10	840	18	71.33
2005	Oct	27	22	840	14	70.83
2005	Oct	28	10	840	12	70.35
2005	Oct	28	22	840	9.3	71.75
2005	Oct	29	10	840	9	71.85
2005	Oct	29	22	840	7.3	72.85
2005	Oct	30	10	840	5	72.75

Table 2.6: Dates of Available CHAMP Data and Corresponding Geomagnetic and Solar Activity for 2006 and 2007

Year	Month	Day	t_i (hr)	span (min)	A_p	$F_{10.7}$
2006	Aug	2	10	840	12.3	74.525
2006	Aug	2	22	840	15	73.625
2006	Aug	3	10	840	5.75	73.85
2006	Aug	3	22	840	8.5	72.05
2006	Aug	4	10	840	2	71.625
2006	Dec	21	22	840	28.3	70.6
2006	Dec	22	10	840	27.8	70.925
2006	Dec	22	22	840	30	70.425
2006	Dec	23	10	840	25.8	70.1
2006	Dec	23	22	840	20.5	70.9
2006	Dec	24	10	840	17.8	70.4

Year	Month	Day	t_i (hr)	span (min)	A_p	$F_{10.7}$
2007	Sep	8	22	840	8.8	67.68
2007	Sep	9	10	840	3.5	67.65
2007	Sep	9	22	840	2	67.85
2007	Sep	10	10	840	3.5	68.13
2007	Sep	10	22	840	3.8	67.23
2007	Sep	11	10	840	4.5	67.08

2.6.3 Solar and Geomagnetic Activity Level Bins

The results of the examination of the accuracy and precision of the corrected densities are sorted into divisions defined in Section 1.5.1 in Tables 2.1-2.6. This is done to examine how the optimal combination of baseline density model, density correlation half-life, and ballistic coefficient correlation half-life is affected by the varying degrees of geomagnetic and solar activity.

2.7 Validation of the Estimated Atmospheric Density

The densities derived in ODTK were compared to those derived from CHAMP and GRACE accelerometers by Sean Bruinsma of CNES. The accelerometer derived densities are averaged over 10 second intervals as described in References 32-33. The POE derived densities are also given in 10 second increments, however, the time stamps for the POE derived densities do not coincide with the accelerometer derived density time-stamps. For this reason, the POE derived densities are interpolated to

corresponding time stamps from the accelerometer derived densities. POE data is interpolated instead of accelerometer data as the variation of the POE densities is smoother than data derived from accelerometers. The accuracy and precision of POE derived densities is compared to those found by comparing results from HASDM to the accelerometer derived densities. Techniques for determining densities for HASDM are defined in Reference 4.

2.8 Cross Correlation

Cross correlation (CC) is a method for determining the degree to which two time-varying quantities are correlated. The method of determining cross correlation was taken from Reference 68. Cross correlation is a measure of precision, and was used to determine the precision of POE derived densities as compared to accelerometer derived densities. Cross correlation, *r*, between two data sets, *x* and y, for a given delay, *d*, is defined as:

$$r\ d\ = \frac{\sum\left[\ x_i - \bar{x}\quad y_{i-d} - \bar{y}\ \right]}{\sqrt{\sum\ x_i - \bar{x}\ ^2}\sqrt{\sum\ y_{i-d} - \bar{y}\ ^2}} \tag{2.6}$$

Values for cross correlation range from -1 to 1, with 1 representing a perfect correlation, and -1 representing a perfect negative correlation. For the purposes of this study, the case with the highest cross correlation was identified for each baseline density model. Then the highest overall cross correlation was identified for all 45 cases.

2.9 Root Mean Squared Values

The Root Mean Squared (RMS) technique is used to compare estimated density corrections to actual densities derived from accelerometers. RMS measures the average deviation from the true values of the quantity in question. RMS for a quantity, *x*, from true value, *y*, is defined as:

$$RMS = \sum_{i=1}^{m} \frac{\sqrt{x_i - y_i}^{2}}{m} \tag{2.7}$$

Both RMS and CC values are used to determine the best set of corrections to atmospheric density due to CC values being susceptible to offset, and RMS values being susceptible to bias that can be introduced by the ballistic coefficient and density approximations and can absorb variations in the atmospheric density. In this study, the RMS values will always possess units of 10^{-12} kg/m^3.

2.10 Travelling Atmospheric Disturbances (TAD)

The TADs on the unlit portion of the earth are observed by removing the portion of the satellite orbits that occur on the lit side of the Earth. This is determined using the local time-stamps provided in the accelerometer density file in conjunction

with the UTC time-stamps that are also supplied as part of the POE density determination scheme as well as the accelerometer-derived density file.

2.11 Geomagnetic Cusp Features

Geomagnetic cusp features are localized around the geomagnetic poles, and thus in this examination, the latitudes and longitudes of the CHAMP satellite are converted into geomagnetic latitude and longitude. This was done by applying a three-dimensional polar coordinate transformation based upon the location of the geomagnetic poles for the year in question. The locations for the geomagnetic poles were obtained from values published by the Geological Survey of Canada [Ref 69]. A series of geomagnetic polar passes were subsequently examined using this data, and the observability of this phenomena using POE density data was assessed.

2.12 Coplanar Cases

There are four known periods of time in which both the CHAMP and GRACE satellites orbited within the same plane. These times were the dates centered around December 14, 2008; February 20, 2007; April 3, 2005; and May 9, 2003. To examine these coplanar times, the time period for three days prior to a specific date, and three days following a specific date are examined. For the time period in question, the cross correlation and root-mean-squared values are found for the POE derived densities and HASDM densities as compared to the accelerometer derived densities. The estimated and accelerometer derived density values are then compared graphically to examine similarities between the density values.

2.13 Extension of Orbit Determination Techniques to TerraSAR-X

The TerraSAR-X satellite has rapid science orbit (RSO) data available from GFZ-Potsdam, much like data available for the CHAMP and GRACE satellites. Unlike the CHAMP and GRACE satellites, TerraSAR-X lacks an accelerometer. By examining the cross correlation and root-mean squared values from the CHAMP and GRACE satellites for the simultaneous time periods with the TerraSAR-X, an optimal orbit determination scheme was determined, and then applied to the TerraSAR-X data. This orbit determination scheme allows corrections to be made to predicted atmospheric densities along the path of the TerraSAR-X satellite. In this research, data was examined from Sept. 21-30, 2007.

3 EFFECTS OF VARYING SELECT ORBIT DETERMINATION PARAMETERS

This section largely encompasses the type of work performed in Reference 59, though expanded to a larger range of dates and times. Cross Correlation (CC) and Root-Mean-Squared (RMS) values are found for a zero-time delay for each variant of density correlation half-life, ballistic coefficient half-life, and baseline density model compared to accelerometer derived densities for CHAMP. CC and RMS values were also found for HASDM and empirical Jacchia-1971 values compared to accelerometer derived densities. This was done for a basis of comparison for improvements made to the existing models. HASDM uses CHAMP as one of its calibration satellites, and the accelerometer derived densities determined by Sean Bruinsma are calibrated in part using HASDM densities, which may skew results in favor HASDM. There may also be biases introduced to both the CC and RMS values due to errors in ballistic coefficient (BC) approximations; if these biases could be removed, slightly different values for atmospheric density would be found. Due to the biases imposed, more consideration was given to the CC values as they are more indicative of the actual atmospheric density trends. The results from these CC and RMS calculations are then time-averaged over the course of all solutions.

3.1 Overall Analysis of Cross-Correlation and Root-Mean-Squared Values for CHAMP

Table 3.1: Zero Delay Cross Correlation Coefficients Time Averaged Across All Solutions.
The total duration is given in minutes, and both the HASDM and Empirical Jacchia 1971 cross correlations are given. Yellow (light gray) indicators are the best cross correlation coefficients for the given baseline density model, and the Orange (darker gray) indicates the best overall cross correlation.

	Total Duration	A_p avg	$F_{10.7}$ avg	HASDM	Empirical
	252877	43.30	140.58	0.9059	0.8538
Half Lives (min) Density/Ballistic	CIRA 1972	Jacchia 1971	Jacchia-Roberts	MSISE 1990	NRLMSISE 2000
1.8-1.8	0.9045	0.9039	0.9040	0.8805	0.8821
1.8-18	0.8988	0.8985	0.8986	0.8775	0.8788
1.8-180	0.8888	0.8884	0.8886	0.8713	0.8729
18-1.8	0.9096	0.9093	0.9094	0.8823	0.8850
18-18	0.9064	0.9061	0.9062	0.8797	0.8820
18-180	0.8919	0.8915	0.8916	0.8671	0.8697
180-1.8	0.9098	0.9098	0.9098	0.8873	0.8883
180-18	0.9050	0.9050	0.9050	0.8834	0.8841
180-180	0.8805	0.8798	0.8799	0.8633	0.8641

Table 3.2: Zero Delay Root-Mean-Squared Values Time Averaged Across All Solutions.
The total duration is given in minutes, and both the HASDM and Empirical Jacchia 1971 RMS values are given. Yellow (light gray) indicators are the best RMS values for the given baseline density model, and the Orange (darker gray) indicates the best overall RMS values. All RMS values are given in 10^{-12} kg/m^3.

	Total Duration	A_p avg	$F_{10.7}$ avg	HASDM	Empirical
	252877	43.30	140.58	0.5597	1.1721
Half Lives (min) Density/Ballistic	CIRA 1972	Jacchia 1971	Jacchia-Roberts	MSISE 1990	NRLMSISE 2000
1.8-1.8	0.6294	0.6291	0.6304	0.9414	0.9346
1.8-18	0.7482	0.7446	0.7472	0.9763	0.9717
1.8-180	0.9433	0.9419	0.9439	1.0707	1.0641
18-1.8	0.5786	0.5825	0.5827	0.9423	0.9315
18-18	0.6130	0.6127	0.6144	0.9581	0.9498
18-180	0.8163	0.8126	0.8162	1.1148	1.1078
180-1.8	0.5702	0.5751	0.5745	0.9218	0.9195
180-18	0.6032	0.6041	0.6046	0.9533	0.9525
180-180	0.8813	0.8773	0.8798	1.2840	1.2816

Tables 3.1 and 3.2 exhibit trends expected in the data in that the results for the varying baseline density models are tiered according to the method of their determination. The CIRA-1972, Jacchia-1971, and Jacchia-Roberts models all show similar results for each given case of density and ballistic coefficient correlation half-lives. The same similarities are apparent in the MSISE-1990, and NRLMSISE-2000 models. Results for the CIRA-1972, Jacchia-1971, and Jacchia-Roberts models are significantly better than those obtained for the MSISE-1990 and NRLMSISE-2000 models and this trend holds true for all variations of geomagnetic and solar activity as will be demonstrated later in this chapter.

The combination of a density correlation half-life of 180 minutes and a ballistic coefficient correlation half-life of 1.8 minutes had the best characteristics for the overall data. Altering the density correlation half-life to 18 minutes yielded very similar results with the major sources of increased accuracy and precision coming from the alteration of ballistic coefficient half-life and the baseline density model. The best baseline density model using this comparison is the Jacchia-1971 model; though the other two Jacchia family density models, CIRA-1972 and Jacchia-Roberts, also show very similar results.

For comparison, results from the empirical Jacchia-1971 model and the HASDM model were also determined. The results obtained from the empirical Jacchia-1971 model were significantly worse than those obtained from the models that included corrections obtained through the use of POEs. The HASDM model exhibited very similar results to the optimal combinations of baseline density model,

density correlation half-life, and ballistic coefficient half-life. The POE corrected densities typically show a slightly better cross correlation to accelerometer data than HASDM densities, though HASDM possesses slightly better RMS values. The degree to which the use of CHAMP as a calibration satellite for HASDM contributes to this accuracy is currently unknown.

3.2 Analysis of Cross-Correlation and Root-Mean-Squared Values for CHAMP for Varying Degrees of Geomagnetic Activity

The cross correlation and root-mean-squared values were separated based on the daily planetary amplitude, A_p, in the manner described in Section 1.5.1. By separating the cases, an investigation can be made into the accuracy and precision of the corrected densities as they are affected by geomagnetic activity.

The geomagnetic activity bins are divided as follows:

- Quiet geomagnetic bin: $A_p \leq 10$
- Moderate geomagnetic bin: $10 < A_p < 50$
- Active geomagnetic bin: $A_p \geq 50$

3.2.1 Quiet Geomagnetic Activity Bin

Table 3.3: Zero Delay Cross Correlation Coefficients Time Averaged for Quiet Geomagnetic Periods.
The total duration is given in minutes, and both the HASDM and Empirical Jacchia 1971 cross correlations are given. Yellow (light gray) indicators are the best cross correlation coefficients for the given baseline density model, and the Orange (darker gray) indicates the best overall cross correlation.

	Total Duration	A_p avg	$F_{10.7}$ avg	HASDM	Empirical
	61780	6.27	123.81	0.9569	0.9367
Half Lives (min) Density/Ballistic	CIRA 1972	Jacchia 1971	Jacchia-Roberts	MSISE 1990	NRLMSISE 2000
1.8-1.8	0.9499	0.9496	0.9495	0.9368	0.9385
1.8-18	0.9497	0.9497	0.9497	0.9389	0.9400
1.8-180	0.9463	0.9462	0.9462	0.9379	0.9388
18-1.8	0.9525	0.9524	0.9523	0.9389	0.9408
18-18	0.9512	0.9509	0.9508	0.9373	0.9391
18-180	0.9415	0.9407	0.9407	0.9285	0.9298
180-1.8	0.9550	0.9550	0.9550	0.9438	0.9452
180-18	0.9529	0.9527	0.9527	0.9413	0.9427
180-180	0.9365	0.9347	0.9347	0.9255	0.9265

Table 3.4: Zero Delay Root-Mean-Squared Values Time averaged for Quiet Geomagnetic Periods.
The total duration is given in minutes, and both the HASDM and Empirical Jacchia 1971 RMS values are given. Yellow (light gray) indicators are the best RMS values for the given baseline density model, and the Orange (darker gray) indicates the best overall RMS values. All RMS values are given in 10^{-12} kg/m^3.

	Total Duration	A_p avg	$F_{10.7}$ avg	HASDM	Empirical
	61780	6.27	123.81	0.3294	0.6403
Half Lives (min) Density/Ballistic	CIRA 1972	Jacchia 1971	Jacchia-Roberts	MSISE 1990	NRLMSISE 2000
1.8-1.8	0.3779	0.3773	0.3775	0.4958	0.4707
1.8-18	0.4425	0.4396	0.4403	0.5181	0.5032
1.8-180	0.5384	0.5378	0.5383	0.5796	0.5715
18-1.8	0.3550	0.3583	0.3578	0.5022	0.4694
18-18	0.3737	0.3745	0.3746	0.5077	0.4809
18-180	0.4838	0.4851	0.4861	0.5946	0.5769
180-1.8	0.3477	0.3519	0.3509	0.4890	0.4562
180-18	0.3632	0.3648	0.3643	0.5005	0.4720
180-180	0.5198	0.5247	0.5251	0.6785	0.6559

Table 3.3 and Table 3.4 indicate that for dates of quiet geomagnetic activity, HASDM out-performs all POE derived densities in terms of both CC and RMS. CC values for the three Jacchia derived models are very similar to the point of being identical out to four significant figures for the optimal combination of density and ballistic coefficient correlation half lives. Corrections to the mass spectrometer incoherent scatter (MSIS) derived models have CC values that are significantly lower than those of the Jacchia-based models. For quiet geomagnetic periods, these CC values are about .01 less for those models' highest CC values as compared to the CC values of the Jacchia based models. The HASDM RMS values are about 0.025×10^{-12} kg/m^3 more accurate than the best value obtained through POE data.

3.2.2 Moderate Geomagnetic Activity Bin

Table 3.5: Zero Delay Cross Correlation Coefficients Time Averaged for Moderate Geomagnetic Periods.
The total duration is given in minutes, and both the HASDM and Empirical Jacchia 1971 cross correlations are given. Yellow (light gray) indicators are the best cross correlation coefficients for the given baseline density model, and the Orange (darker gray) indicates the best overall cross correlation.

	Total Duration	A_p avg	$F_{10.7}$ avg	HASDM	Empirical
	122367	24.17	139.34	0.9157	0.8781
Half Lives (min) Density/Ballistic	CIRA 1972	Jacchia 1971	Jacchia-Roberts	MSISE 1990	NRLMSISE 2000
1.8-1.8	0.9154	0.9146	0.9149	0.8940	0.8969
1.8-18	0.9112	0.9110	0.9111	0.8918	0.8942
1.8-180	0.9028	0.9026	0.9028	0.8867	0.8889
18-1.8	0.9180	0.9176	0.9178	0.8930	0.8972
18-18	0.9148	0.9145	0.9147	0.8903	0.8942
18-180	0.8982	0.8980	0.8983	0.8754	0.8791
180-1.8	0.9194	0.9194	0.9194	0.8980	0.9010
180-18	0.9146	0.9146	0.9146	0.8937	0.8963
180-180	0.8860	0.8858	0.8858	0.8693	0.8718

Table 3.6: Zero Delay Root-Mean-Squared Values Time averaged for Moderate Geomagnetic Periods.
The total duration is given in minutes, and both the HASDM and Empirical Jacchia 1971 RMS values are given. Yellow (light gray) indicators are the best RMS values for the given baseline density model, and the Orange (darker gray) indicates the best overall RMS values. All RMS values are given in 10^{-12} kg/m^3.

	Total Duration	A_p avg	$F_{10.7}$ avg	HASDM	Empirical
	122367	24.17	139.34	0.4505	0.8533
Half Lives (min) Density/Ballistic	CIRA 1972	Jacchia 1971	Jacchia-Roberts	MSISE 1990	NRLMSISE 2000
1.8-1.8	0.5008	0.4988	0.4993	0.7405	0.7042
1.8-18	0.5814	0.5750	0.5775	0.7505	0.7263
1.8-180	0.7112	0.7075	0.7098	0.8034	0.7900
18-1.8	0.4753	0.4784	0.4777	0.7591	0.7134
18-18	0.5005	0.4976	0.4988	0.7686	0.7287
18-180	0.6674	0.6589	0.6627	0.8941	0.8643
180-1.8	0.4637	0.4681	0.4665	0.7434	0.6995
180-18	0.4898	0.4887	0.4885	0.7684	0.7287
180-180	0.7440	0.7330	0.7351	1.0530	1.0189

Table 3.5 and Table 3.6 indicate that HASDM densities again outperform POE derived densities in terms of RMS, though the POE densities show better CC values for the Jacchia-based models. Again, CC values for the three Jacchia based models are almost identical, with the two MSIS models having both lower CC and RMS values. For moderate geomagnetic activity, the CC values of the MSIS models are about 0.02 less than values obtained for Jacchia based models. The HASDM RMS values are about 0.013×10^{-12} kg/m^3 better than optimal values from the Jacchia based models, which are in turn, about 0.28×10^{-12} kg/m^3 better than values obtained for the MSIS derived models.

3.2.3 Active Geomagnetic Activity Bin

Table 3.7: Zero Delay Cross Correlation Coefficients Time Averaged for Active Geomagnetic Periods.
The total duration is given in minutes, and both the HASDM and Empirical Jacchia 1971 cross correlations are given. Yellow (light gray) indicators are the best cross correlation coefficients for the given baseline density model, and the Orange (darker gray) indicates the best overall cross correlation.

	Total Duration	A_p avg	$F_{10.7}$ avg	HASDM	Empirical
	68730	110.64	157.87	0.8424	0.7359
Half Lives (min) Density/Ballistic	CIRA 1972	Jacchia 1971	Jacchia-Roberts	MSISE 1990	NRLMSISE 2000
1.8-1.8	0.8443	0.8439	0.8439	0.8058	0.8051
1.8-18	0.8308	0.8304	0.8303	0.7968	0.7964
1.8-180	0.8120	0.8112	0.8114	0.7839	0.7850
18-1.8	0.8560	0.8559	0.8558	0.8122	0.8130
18-18	0.8512	0.8510	0.8510	0.8089	0.8091
18-180	0.8360	0.8357	0.8358	0.7973	0.7989
180-1.8	0.8520	0.8521	0.8519	0.8174	0.8145
180-18	0.8451	0.8451	0.8450	0.8129	0.8096
180-180	0.8202	0.8199	0.8200	0.7966	0.7943

Table 3.8: Zero Delay Root-Mean-Squared Values Time averaged for Active Geomagnetic Periods.
The total duration is given in minutes, and both the HASDM and Empirical Jacchia 1971 RMS values are given. Yellow (light gray) indicators are the best RMS values for the given baseline density model, and the Orange (darker gray) indicates the best overall RMS values. All RMS values are given in 10^{-12} kg/m^3.

	Total Duration	A_p avg	$F_{10.7}$ avg	HASDM	Empirical
	68730	110.64	157.87	0.9612	2.2176
Half Lives (min) Density/Ballistic	CIRA 1972	Jacchia 1971	Jacchia-Roberts	MSISE 1990	NRLMSISE 2000
1.8-1.8	1.0843	1.0875	1.0912	1.6996	1.7616
1.8-18	1.3199	1.3207	1.3253	1.7903	1.8297
1.8-180	1.7205	1.7222	1.7252	1.9882	1.9950
18-1.8	0.9635	0.9696	0.9719	1.6639	1.7350
18-18	1.0283	1.0320	1.0359	1.7003	1.7647
18-180	1.3802	1.3806	1.3863	1.9754	2.0187
180-1.8	0.9599	0.9661	0.9677	1.6284	1.7276
180-18	1.0209	1.0245	1.0274	1.6896	1.7830
180-180	1.4508	1.4512	1.4563	2.2394	2.3115

Table 3.7 and Table 3.8 indicate that during active geomagnetic periods, POE derived densities for Jacchia based models yield superior CC and RMS values than both HASDM and MSIS derived densities. The Jacchia based models have CC values about 0.014 better than HASDM values, and about 0.04 better than MSIS derived densities. The Jacchia based RMS values perform 0.0013×10^{-12} kg/m^3 better than HASDM densities and about 0.65×10^{-12} kg/m^3 better than MSIS derived densities. During active geomagnetic periods, the optimal combination of density and ballistic coefficient correlation half-lives is a 1.8 minute ballistic coefficient correlation half-life, and either an 18 or 180 minute density correlation half-life depending upon usage of either the CC or RMS results.

3.2.4 Summary of the Geomagnetic Activity Bins

As would be expected, the accuracy and precision of the corrected atmospheric densities decreases with increased geomagnetic activity. During quiet geomagnetic periods, HASDM cross correlation coefficients and root-mean-squared values tend to fare slightly better than POE derived density corrections. As geomagnetic activity increases, however, POE derived densities show better CC and RMS values as compared to HASDM values. For all levels of geomagnetic activity, the Jacchia based models performed noticeably better than those based on Mass Spectrometer Incoherent Scatter (MSIS). Also, a ballistic coefficient correlation half-life of 1.8 minutes proved to be best for all levels of geomagnetic activity. At increased levels of geomagnetic activity, the optimal input of density correlation half-life decreases from 180 minutes to 18 minutes, which is to be expected if variation frequency increases with increased levels of geomagnetic activity.

Cross correlation coefficients for the three Jacchia based baseline models are relatively similar for all levels of geomagnetic activity, but comparative RMS values vary. During quiet geomagnetic periods, the Jacchia-1971 and Jacchia-Roberts baseline models yield better RMS values; during moderate geomagnetic periods, all three baseline models have similar RMS values; and during active geomagnetic periods, the CIRA-1972 baseline model yields better RMS values than the other two baseline models.

3.2.5 Low Solar Activity Bin

Table 3.9: Zero Delay Cross Correlation Coefficients Time Averaged for Low Solar Activity Periods.
The total duration is given in minutes, and both the HASDM and Empirical Jacchia 1971 cross correlations are given. Yellow (light gray) indicators are the best cross correlation coefficients for the given baseline density model, and the Orange (darker gray) indicates the best overall cross correlation.

	Total Duration	A_p avg	$F_{10.7}$ avg	HASDM	Empirical
	26821	12.72	71.23	0.9305	0.8969
Half Lives (min) Density/Ballistic	CIRA 1972	Jacchia 1971	Jacchia-Roberts	MSISE 1990	NRLMSISE 2000
1.8-1.8	0.9120	0.9087	0.9093	0.8927	0.8954
1.8-18	0.9127	0.9124	0.9127	0.8989	0.9001
1.8-180	0.9087	0.9087	0.9088	0.9004	0.9009
18-1.8	0.9265	0.9256	0.9257	0.9088	0.9109
18-18	0.9246	0.9240	0.9242	0.9072	0.9091
18-180	0.9146	0.9148	0.9150	0.8998	0.9012
180-1.8	0.9307	0.9307	0.9307	0.9147	0.9164
180-18	0.9281	0.9283	0.9284	0.9122	0.9139
180-180	0.9068	0.9060	0.9064	0.8942	0.8960

Table 3.10: Zero Delay Root-Mean-Squared Values Time averaged for Low Solar Activity Periods.
The total duration is given in minutes, and both the HASDM and Empirical Jacchia 1971 RMS values are given. Yellow (light gray) indicators are the best RMS values for the given baseline density model, and the Orange (darker gray) indicates the best overall RMS values. All RMS values are given in 10^{-12} kg/m^3.

	Total Duration	A_p avg	$F_{10.7}$ avg	HASDM	Empirical
	26821	12.72	71.23	0.2983	0.7259
Half Lives (min) Density/Ballistic	CIRA 1972	Jacchia 1971	Jacchia-Roberts	MSISE 1990	NRLMSISE 2000
1.8-1.8	0.3662	0.3528	0.3526	0.4297	0.4293
1.8-18	0.4784	0.4529	0.4549	0.5279	0.5312
1.8-180	0.6097	0.5976	0.5985	0.6398	0.6413
18-1.8	0.3091	0.3149	0.3111	0.3757	0.3684
18-18	0.3342	0.3187	0.3179	0.4071	0.4051
18-180	0.4843	0.4531	0.4559	0.5518	0.5552
180-1.8	0.2964	0.3086	0.3038	0.3565	0.3484
180-18	0.3085	0.3032	0.3006	0.3758	0.3723
180-180	0.4635	0.4225	0.4264	0.5400	0.5469

Table 3.9 and Table 3.10 indicate that for periods of low solar flux, very high CC values, and very low RMS values were observed for all corrected and uncorrected models. The POE derived density corrections to the CIRA-1972 model yield slightly better CC and RMS values than HASDM densities, and the CC values for the corrected Jacchia-1971 and Jacchia-Roberts models also surpass that of HASDM densities. The high quality of the CC and RMS values results from the low solar activity which causes the atmosphere to behave much like idealized empirical versions of the atmosphere.

3.2.6 Moderate Solar Activity Bin

Table 3.11: Zero Delay Cross Correlation Coefficients Time Averaged for Moderate Solar Activity Periods.
The total duration is given in minutes, and both the HASDM and Empirical Jacchia 1971 cross correlations are given. Yellow (light gray) indicators are the best cross correlation coefficients for the given baseline density model, and the Orange (darker gray) indicates the best overall cross correlation.

	Total Duration	A_p avg	$F_{10.7}$ avg	HASDM	Empirical
	131210	46.87	115.69	0.8873	0.8341
Half Lives (min) Density/Ballistic	CIRA 1972	Jacchia 1971	Jacchia-Roberts	MSISE 1990	NRLMSISE 2000
1.8-1.8	0.8891	0.8888	0.8888	0.8654	0.8663
1.8-18	0.8806	0.8804	0.8804	0.8608	0.8616
1.8-180	0.8707	0.8703	0.8704	0.8556	0.8566
18-1.8	0.8945	0.8944	0.8944	0.8676	0.8698
18-18	0.8913	0.8912	0.8911	0.8654	0.8673
18-180	0.8779	0.8777	0.8778	0.8552	0.8574
180-1.8	0.8932	0.8933	0.8932	0.8688	0.8695
180-18	0.8877	0.8878	0.8877	0.8646	0.8653
180-180	0.8683	0.8681	0.8680	0.8502	0.8511

Table 3.12: Zero Delay Root-Mean-Squared Values Time averaged for Moderate Solar Activity Periods.
The total duration is given in minutes, and both the HASDM and Empirical Jacchia 1971 RMS values are given. Yellow (light gray) indicators are the best RMS values for the given baseline density model, and the Orange (darker gray) indicates the best overall RMS values. All RMS values are given in 10^{-12} kg/m^3.

	Total Duration	A_p avg	$F_{10.7}$ avg	HASDM	Empirical
	131210	46.87	115.69	0.5551	0.9733
Half Lives (min) Density/Ballistic	CIRA 1972	Jacchia 1971	Jacchia-Roberts	MSISE 1990	NRLMSISE 2000
1.8-1.8	0.5965	0.5958	0.5962	0.8802	0.8620
1.8-18	0.6857	0.6821	0.6836	0.8750	0.8668
1.8-180	0.8092	0.8074	0.8088	0.9141	0.9102
18-1.8	0.5609	0.5636	0.5633	0.9073	0.8807
18-18	0.5875	0.5862	0.5871	0.9032	0.8821
18-180	0.7275	0.7207	0.7232	0.9929	0.9779
180-1.8	0.5590	0.5622	0.5614	0.8968	0.8759
180-18	0.5883	0.5864	0.5867	0.9152	0.8967
180-180	0.7752	0.7621	0.7647	1.1396	1.1204

Table 3.11 and Table 3.12 indicate that HASDM RMS values are slightly better than the optimal values obtained for POE derived densities, but optimal CC values for all three Jacchia based models were greater than those found for HASDM. Both CC and RMS values of the Jacchia based models outperform those of the two MSIS models, by roughly 0.025 for CC values and by 0.3×10^{-12} kg/m^3 for RMS values. Corrected density models perform best during periods of moderate solar activity with a ballistic coefficient correlation half-life of 1.8 minutes, and a density correlation half-life of either 18 minutes for CC values, or 180 minutes for RMS values. The actual values of the two quantities changes very little from 18 to 180 minutes, so either value is viable for an optimal choice for determining atmospheric density.

3.2.7 Elevated Solar Activity Bin

Table 3.13: Zero Delay Cross Correlation Coefficients Time Averaged for Elevated Solar Activity Periods.
The total duration is given in minutes, and both the HASDM and Empirical Jacchia 1971 cross correlations are given. Yellow (light gray) indicators are the best cross correlation coefficients for the given baseline density model, and the Orange (darker gray) indicates the best overall cross correlation.

	Total Duration	A_p avg	$F_{10.7}$ avg	HASDM	Empirical
	51250	35.80	172.48	0.9432	0.9012
Half Lives (min) Density/Ballistic	CIRA 1972	Jacchia 1971	Jacchia-Roberts	MSISE 1990	NRLMSISE 2000
1.8-1.8	0.9448	0.9444	0.9446	0.9250	0.9265
1.8-18	0.9408	0.9406	0.9407	0.9214	0.9228
1.8-180	0.9315	0.9312	0.9314	0.9137	0.9160
18-1.8	0.9470	0.9467	0.9469	0.9235	0.9259
18-18	0.9431	0.9428	0.9430	0.9200	0.9220
18-180	0.9298	0.9295	0.9299	0.9080	0.9102
180-1.8	0.9446	0.9444	0.9445	0.9277	0.9287
180-18	0.9401	0.9399	0.9399	0.9234	0.9239
180-180	0.9166	0.9163	0.9167	0.9059	0.9060

Table 3.14: Zero Delay Root-Mean-Squared Values Time averaged for Elevated Solar Activity Periods.
The total duration is given in minutes, and both the HASDM and Empirical Jacchia 1971 RMS values are given. Yellow (light gray) indicators are the best RMS values for the given baseline density model, and the Orange (darker gray) indicates the best overall RMS values. All RMS values are given in 10^{-12} kg/m^3.

	Total Duration	A_p avg	$F_{10.7}$ avg	HASDM	Empirical
	51250	35.80	172.48	0.5624	1.1163
Half Lives (min) Density/Ballistic	CIRA 1972	Jacchia 1971	Jacchia-Roberts	MSISE 1990	NRLMSISE 2000
1.8-1.8	0.6105	0.6096	0.6141	0.9235	0.9142
1.8-18	0.7120	0.7090	0.7153	0.9439	0.9286
1.8-180	0.8933	0.8906	0.8962	1.0178	1.0023
18-1.8	0.5806	0.5807	0.5848	0.9388	0.9342
18-18	0.6192	0.6175	0.6235	0.9588	0.9485
18-180	0.8100	0.8065	0.8152	1.0951	1.0796
180-1.8	0.5815	0.5824	0.5847	0.9328	0.9348
180-18	0.6204	0.6201	0.6237	0.9711	0.9668
180-180	0.9132	0.9133	0.9183	1.3110	1.2933

Table 3.13 and Table 3.14 indicate that for periods of elevated solar activity, HASDM densities have better RMS values than any of the POE derived densities, however, the CC values of the corrections to the Jacchia based models are superior to the value obtained for HASDM. The difference between these values for the optimal combination of baseline model, density correlation half-life, and ballistic coefficient half-life, and the HASDM densities is relatively small in comparison to the MSIS derived baseline model corrections, which have significantly higher RMS values, 0.34×10^{-12} kg/m^3, and markedly lower CC values, 0.02, as compared to both HASDM and Jacchia based densities.

3.2.8 High Solar Activity Bin

Table 3.15: Zero Delay Cross Correlation Coefficients Time Averaged for High Solar Activity Periods.
The total duration is given in minutes, and both the HASDM and Empirical Jacchia 1971 cross correlations are given. Yellow (light gray) indicators are the best cross correlation coefficients for the given baseline density model, and the Orange (darker gray) indicates the best overall cross correlation.

	Total Duration	A_p avg	$F_{10.7}$ avg	HASDM	Empirical
	43596	60.19	220.67	0.9028	0.8306
Half Lives (min) Density/Ballistic	CIRA 1972	Jacchia 1971	Jacchia-Roberts	MSISE 1990	NRLMSISE 2000
1.8-1.8	0.8989	0.8990	0.8991	0.8662	0.8694
1.8-18	0.8953	0.8952	0.8952	0.8629	0.8658
1.8-180	0.8805	0.8801	0.8803	0.8504	0.8538
18-1.8	0.9004	0.9003	0.9005	0.8617	0.8665
18-18	0.8975	0.8972	0.8972	0.8582	0.8626
18-180	0.8752	0.8739	0.8740	0.8349	0.8396
180-1.8	0.9059	0.9058	0.9058	0.8785	0.8798
180-18	0.9018	0.9015	0.9014	0.8749	0.8753
180-180	0.8583	0.8561	0.8561	0.8335	0.8342

Table 3.16: Zero Delay Root-Mean-Squared Values Time averaged for High Solar Activity Periods.
The total duration is given in minutes, and both the HASDM and Empirical Jacchia 1971 RMS values are given. Yellow (light gray) indicators are the best RMS values for the given baseline density model, and the Orange (darker gray) indicates the best overall RMS values. All RMS values are given in 10^{-12} kg/m^3.

	Total Duration	A_p avg	$F_{10.7}$ avg	HASDM	Empirical
	43596	60.19	220.67	0.7313	2.1105
Half Lives (min) Density/Ballistic	CIRA 1972	Jacchia 1971	Jacchia-Roberts	MSISE 1990	NRLMSISE 2000
1.8-1.8	0.9125	0.9224	0.9235	1.4614	1.4877
1.8-18	1.1447	1.1538	1.1560	1.5952	1.6091
1.8-180	1.6109	1.6185	1.6191	1.8695	1.8604
18-1.8	0.7956	0.8065	0.8060	1.4002	1.4275
18-18	0.8537	0.8678	0.8685	1.4613	1.4898
18-180	1.2950	1.3173	1.3188	1.8513	1.8722
180-1.8	0.7592	0.7692	0.7683	1.3317	1.3841
180-18	0.8096	0.8234	0.8230	1.4024	1.4609
180-180	1.4203	1.4614	1.4598	2.1444	2.2049

Table 3.15 and Table 3.16 indicate that for periods of elevated solar activity, HASDM densities seem to have better RMS values than any of the POE derived densities, however, the CC values of the corrections to the Jacchia based models are superior to the value obtained for HASDM. The difference between these values for the optimal combination of baseline model, density correlation half-life, and ballistic coefficient half-life, and the HASDM densities is relatively small in comparison to the MSIS derived baseline model corrections, which have significantly higher RMS values, 0.57×10^{-12} kg/m^3, and markedly lower CC values, 0.025, as compared to both HASDM and Jacchia based densities.

3.2.9 Summary of the Solar Activity Bins

As seen before, the Jacchia based baseline models perform noticeably better than the MSIS derived models in terms of cross correlation coefficient, as well as, root-mean-squared values. HASDM densities have better RMS values for higher solar activity levels; while POE derived densities have better RMS values at low levels of solar activity. For most levels of solar activity, the optimal density correlation half-life is 180 minutes, with a ballistic coefficient correlation half-life of 1.8 minutes. The CIRA-1972 baseline model generally performs better than the other two Jacchia based models; this holds true for periods of low, moderate and elevated solar activity, though during periods of high solar activity, the CIRA-1972 baseline model possesses less accurate RMS values than the other two models, yet higher cross correlation coefficients. This is also consistent with the results for periods of high geomagnetic activity, of which this time period belongs in which overall data showed that for active geomagnetic periods a density correlation half-life of 18 minutes performs better than a half-life of 180 minutes.

POE derived densities performed better in terms of cross correlation coefficient than HASDM densities for all levels of solar activity. Additional corrections may need to be made to the POE derived densities to decrease the RMS values to be more competitive with the HASDM RMS values. These possible corrections would attempt to reduce bias in the densities caused by errors in the ballistic coefficient estimation, though the source of the bias may also reside in the accelerometer data requiring it to be adjusted instead.

4 OBSERVABILITY OF TRAVELLING ATMOSPHERIC DISTURBANCES IN PRECISION ORBIT EPHEMERIS DERIVED DENSITIES

This chapter examines the observability of travelling atmospheric disturbances (TAD) during the time periods of April 19, 2002, and May 23, 2002. Cross correlation coefficients were taken for the time period in question, as well as root-mean-squared values. In addition to the two techniques utilized earlier, graphical representation of the densities along the path of the satellite will be provided. The temporal span of the disturbances, as measured by the satellite, was between 6-10 minutes. The observed densities were zeroed out for time periods that were not along the nocturnal passes during which the TADs were observed in accelerometer derived densities.

4.1 Cross Correlation and Root-Mean-Squared Values for April 19, 2002

Table 4.1: Cross Correlation Coefficients for All of April 19, 2002.
The total duration is given in minutes, and both the HASDM and Empirical Jacchia 1971 cross correlations are given. Yellow (light gray) indicators are the best cross correlation coefficients for the given baseline density model, and the Orange (darker gray) indicates the best overall cross correlation.

	Total Duration	A_p avg	$F_{10.7}$ avg	HASDM	Empirical
	4314	70.00	179.70	0.7774	0.6878
Half Lives (min) Density/Ballistic	CIRA 1972	Jacchia 1971	Jacchia-Roberts	MSISE 1990	NRLMSISE 2000
1.8-1.8	0.7873	0.7829	0.7855	0.6871	0.7110
1.8-18	0.7848	0.7809	0.7831	0.6790	0.7045
1.8-180	0.7639	0.7596	0.7620	0.6519	0.6832
18-1.8	0.8054	0.8010	0.8034	0.6893	0.7165
18-18	0.7972	0.7933	0.7957	0.6833	0.7097
18-180	0.7621	0.7579	0.7608	0.6544	0.6856
180-1.8	0.7881	0.7851	0.7863	0.7387	0.7488
180-18	0.7791	0.7765	0.7777	0.7292	0.7390
180-180	0.6996	0.6964	0.6993	0.6964	0.7070

Table 4.2: Root-Mean-Squared Values for All of April 19, 2002.
The total duration is given in minutes, and both the HASDM and Empirical Jacchia 1971 RMS values are given. Yellow (light gray) indicators are the best RMS values for the given baseline density model, and the Orange (darker gray) indicates the best overall RMS values. All RMS values are given in 10^{-12} kg/m^3.

	Total Duration	A_p avg	$F_{10.7}$ avg	HASDM	Empirical
	4314	70.00	179.70	1.1285	1.7898
Half Lives (min) Density/Ballistic	CIRA 1972	Jacchia 1971	Jacchia-Roberts	MSISE 1990	NRLMSISE 2000
1.8-1.8	1.0192	1.0290	1.0351	1.8861	1.7861
1.8-18	1.1654	1.1733	1.1811	1.8624	1.7808
1.8-180	1.4857	1.4964	1.4992	1.8930	1.8143
18-1.8	0.9460	0.9570	0.9618	1.9104	1.7955
18-18	1.0086	1.0179	1.0249	1.9390	1.8324
18-180	1.3084	1.3196	1.3270	2.1092	1.9956
180-1.8	0.9516	0.9580	0.9641	1.8441	1.7547
180-18	1.0008	1.0060	1.0142	1.9209	1.8301
180-180	1.4659	1.4845	1.4920	2.6796	2.4594

April 19 is a day of elevated solar activity, and high geomagnetic activity due to the coronal mass ejections that occurred during that period. With these characteristics, the cross correlation and root-mean-squared values seen in Table 4.1 and Table 4.2 for April 19 follow trends expressed in the previous section for dates with similar characteristics. The optimal CC and RMS values occur for the CIRA-1972 baseline model, with a ballistic coefficient correlation half-life of 1.8 minutes, and a density correlation half-life of 18 minutes. This is consistent with earlier results of optimal density and ballistic coefficient half-life values for high geomagnetic activity. For overall data, the optimal combination was of 180 minutes for the density correlation half-life and 1.8 minutes for ballistic coefficient correlation half-life. The values for the variation of 18 minutes for the density correlation half-life are only very slightly less than those of the 180 minute variation.

The CC and RMS values were also examined for only the nocturnal passes during which the TADs were observed. This was done by setting the value to zero for all densities that existed in other time periods. This zeroing of density values greatly improves the CC and RMS values with respect to those found in Tables 4.1 and 4.2, however, these values are used in comparison to other cases which possess the same zeroed out densities, which makes the values acceptable.

Table 4.3: Cross Correlation Coefficients for Limited Nocturnal Periods of April 19, 2002.
The total duration is given in minutes, and both the HASDM and Empirical Jacchia 1971 cross correlations are given. Yellow (light gray) indicators are the best cross correlation coefficients for the given baseline density model, and the Orange (darker gray) indicates the best overall cross correlation.

	Total Duration	A_p avg	$F_{10.7}$ avg	HASDM	Empirical
	252877	43.30	140.58	0.9787	0.9741
Half Lives (min) Density/Ballistic	CIRA 1972	Jacchia 1971	Jacchia-Roberts	MSISE 1990	NRLMSISE 2000
1.8-1.8	0.9786	0.9783	0.9785	0.9688	0.9725
1.8-18	0.9789	0.9786	0.9788	0.9686	0.9722
1.8-180	0.9781	0.9778	0.9780	0.9665	0.9709
18-1.8	0.9796	0.9793	0.9795	0.9683	0.9723
18-18	0.9800	0.9797	0.9799	0.9688	0.9726
18-180	0.9797	0.9794	0.9796	0.9673	0.9717
180-1.8	0.9773	0.9772	0.9772	0.9741	0.9757
180-18	0.9772	0.9770	0.9771	0.9738	0.9752
180-180	0.9780	0.9778	0.9779	0.9742	0.9759

Table 4.4: Root-Mean-Squared Values for Limited Nocturnal Periods of April 19, 2002.
The total duration is given in minutes, and both the HASDM and Empirical Jacchia 1971 RMS values are given. Yellow (light gray) indicators are the best RMS values for the given baseline density model, and the Orange (darker gray) indicates the best overall RMS values. All RMS values are given in 10^{-12} kg/m^3.

	Total Duration	A_p avg	$F_{10.7}$ avg	HASDM	Empirical
	4314	70.00	179.70	0.4638	0.5266
Half Lives (min) Density/Ballistic	CIRA 1972	Jacchia 1971	Jacchia-Roberts	MSISE 1990	NRLMSISE 2000
1.8-1.8	0.4588	0.4630	0.4596	0.5885	0.5532
1.8-18	0.4519	0.4552	0.4528	0.5790	0.5465
1.8-180	0.4609	0.4637	0.4619	0.5850	0.5496
18-1.8	0.4510	0.4557	0.4518	0.5967	0.5606
18-18	0.4444	0.4486	0.4452	0.5900	0.5553
18-180	0.4428	0.4465	0.4441	0.6012	0.5654
180-1.8	0.4731	0.4757	0.4735	0.5550	0.5346
180-18	0.4717	0.4738	0.4721	0.5655	0.5417
180-180	0.4665	0.4683	0.4685	0.6603	0.6152

When the examined data set is limited to only the nocturnal passes, the best CC and RMS values are obtained when the ballistic coefficient correlation half-life is

increased to 18 minutes as seen in Table 4.3 and Table 4.4. Other optimal parameters remain the same as for the cumulative data for April 19.

4.2 Density Values for Nocturnal Passes on April 19, 2002

Five density values were represented for each of the four passes shown in Figures 4.1-4.4 that CHAMP performed during the period in which the TAD existed. The first are the accelerometer densities, which are gauged as truth; the second are the densities predicted by HASDM; the third are densities obtained from the empirical Jacchia model; and the final two are the optimal configurations determined in the previous subsection, with a CIRA-1972 baseline model, an 18 minute density correlation half-life, and ballistic coefficient correlation half-lives of 1.8 and 18 minutes. By examining these values, it can be determined if/how well the density models and modified density models characterize the TADs.

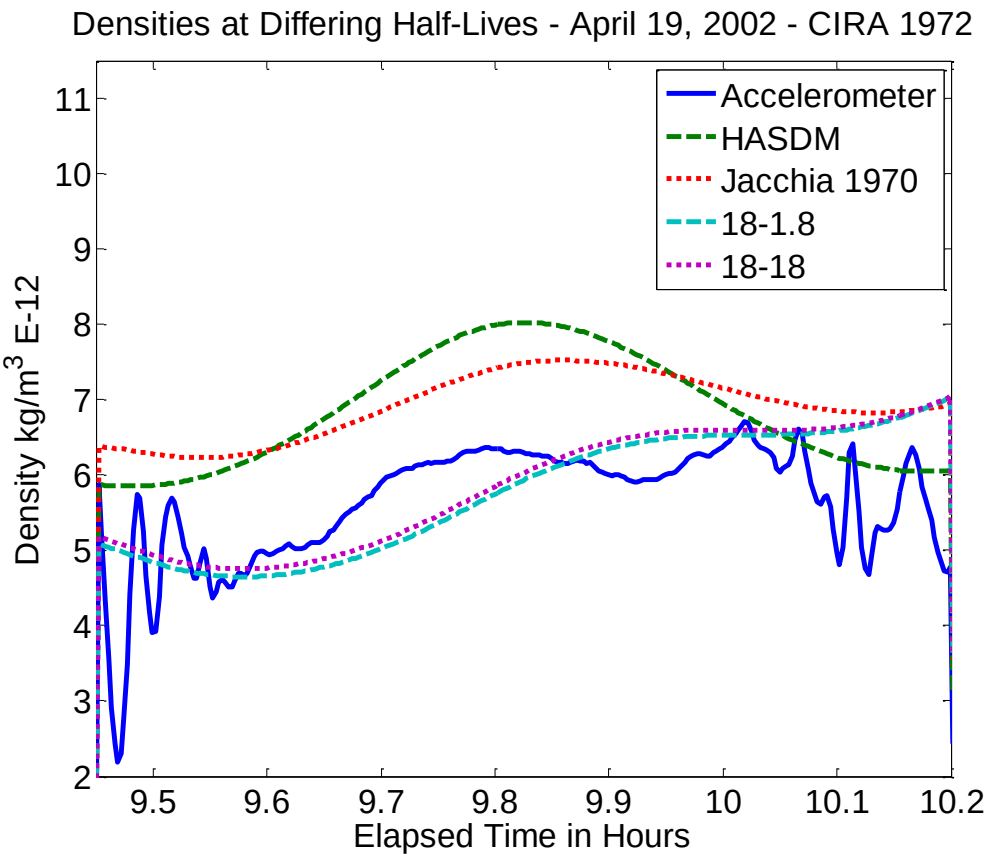

Figure 4.1: Nocturnal CHAMP Satellite Densities on April 19, 2002, Orbit 7
The TAD has yet to initialize, and the atmospheric densities remain relatively constant.

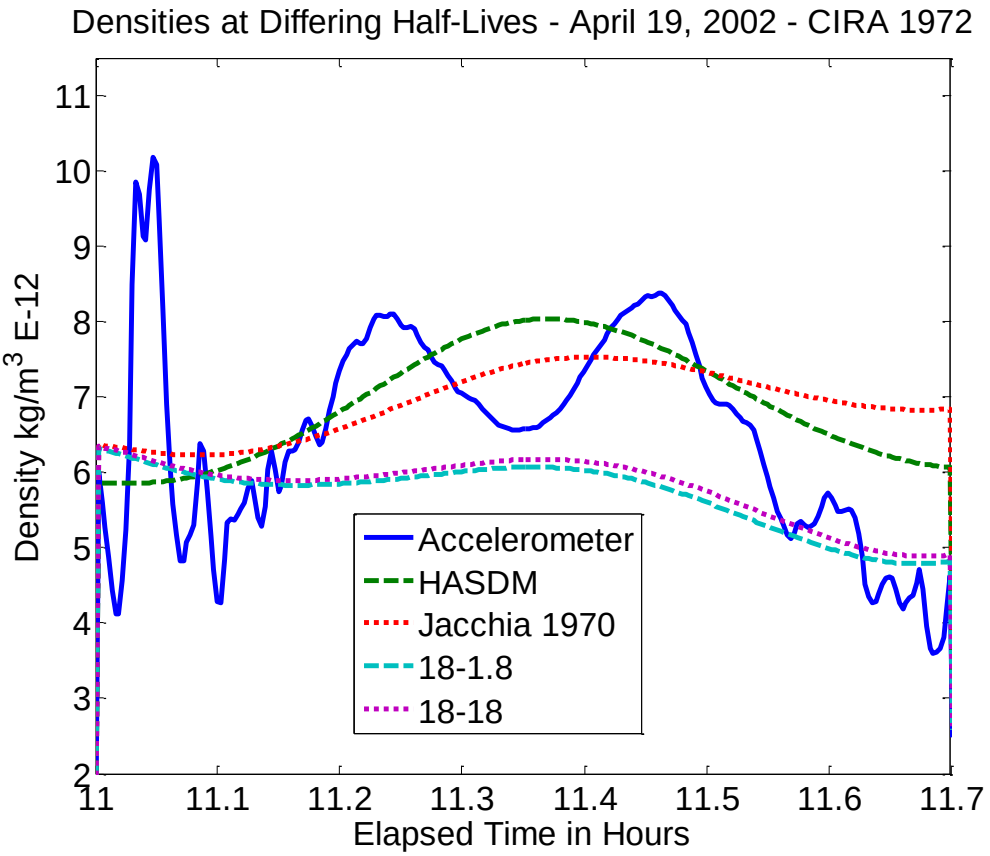

Figure 4.2: Nocturnal CHAMP Satellite Densities on April 19, 2002, Orbit 8
The TAD is propagating toward the equator at this point and is observable as the two localized density increases at approximately 11.24 hours and 11.46 hours.

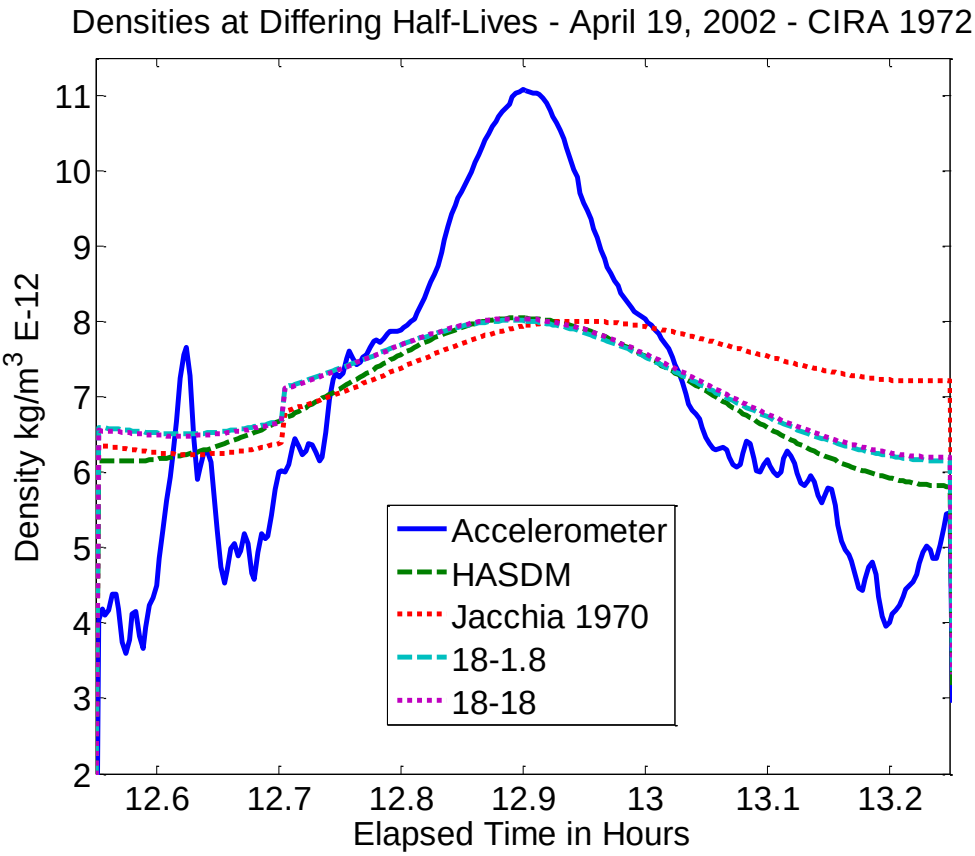

Figure 4.3: Nocturnal CHAMP Satellite Densities on April 19, 2002, Orbit 9
The TADs from the opposing poles are constructively interfering near the equator, or at 12.9 hours.

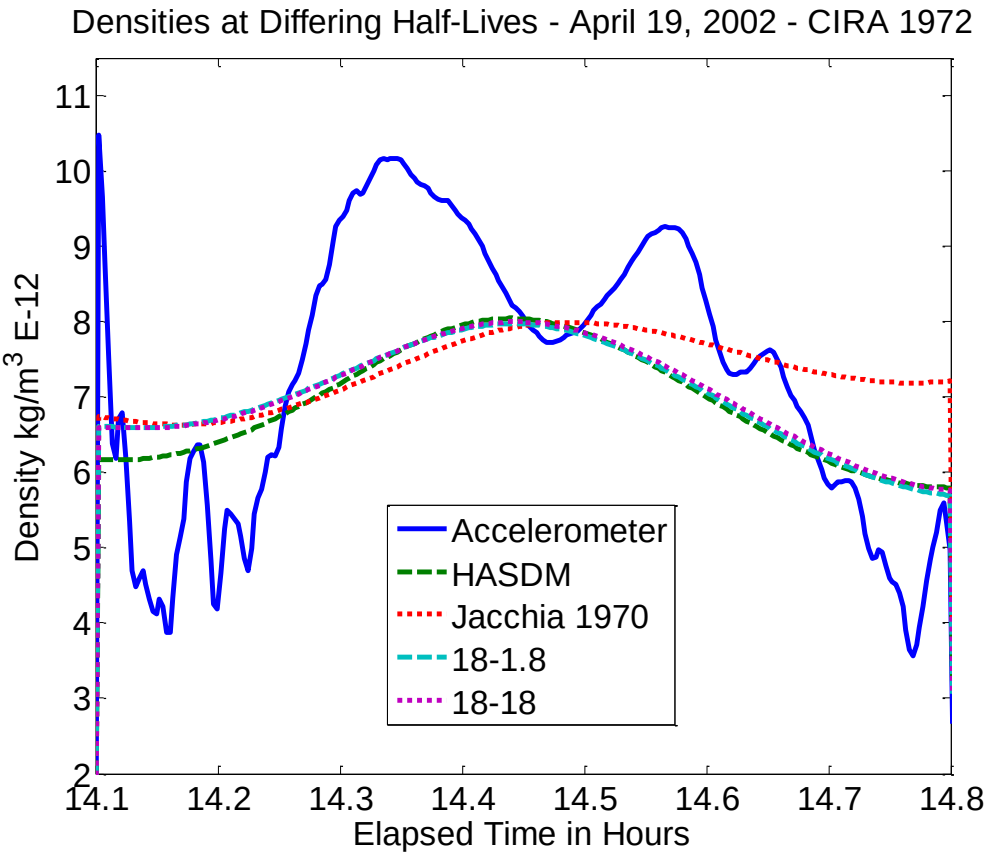

Figure 4.4: Nocturnal CHAMP Satellite Densities on April 19, 2002, Orbit 10
The TADs have passed through each other and continue on towards the opposing poles.

4.3 Density Values for Nocturnal Passes on May 23, 2002

Four density values were represented for the three passes CHAMP performed during the period in which the TAD existed. The first are the accelerometer densities, which are gauged as truth; the second are the densities predicted by HASDM; the third are densities obtained from the empirical Jacchia model; and the final set of densities is the optimal configuration determined for overall data, with a CIRA-1972 baseline model, an 180 minute density correlation half-life, and ballistic coefficient correlation half-lives of 1.8 minutes. This TAD was observed over the course of three orbits seen in Figures 4.5-4.7. Examination of these values will indicate if the lack of correlation in the previous subsection was merely an outlier in terms of the prediction of atmospheric density for TADs.

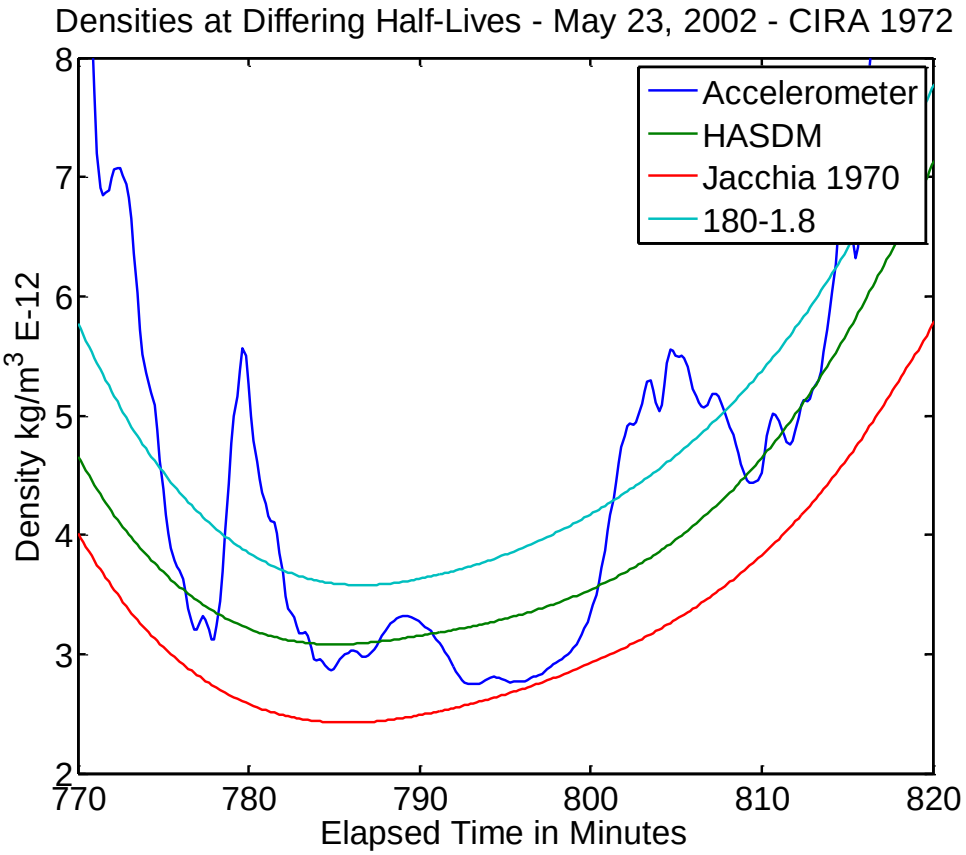

Figure 4.5: Nocturnal CHAMP Satellite Densities on May 23, 2002, Orbit 9
The TADs are seen at about 780 minutes and 805 minutes respectively, moving equator-ward.

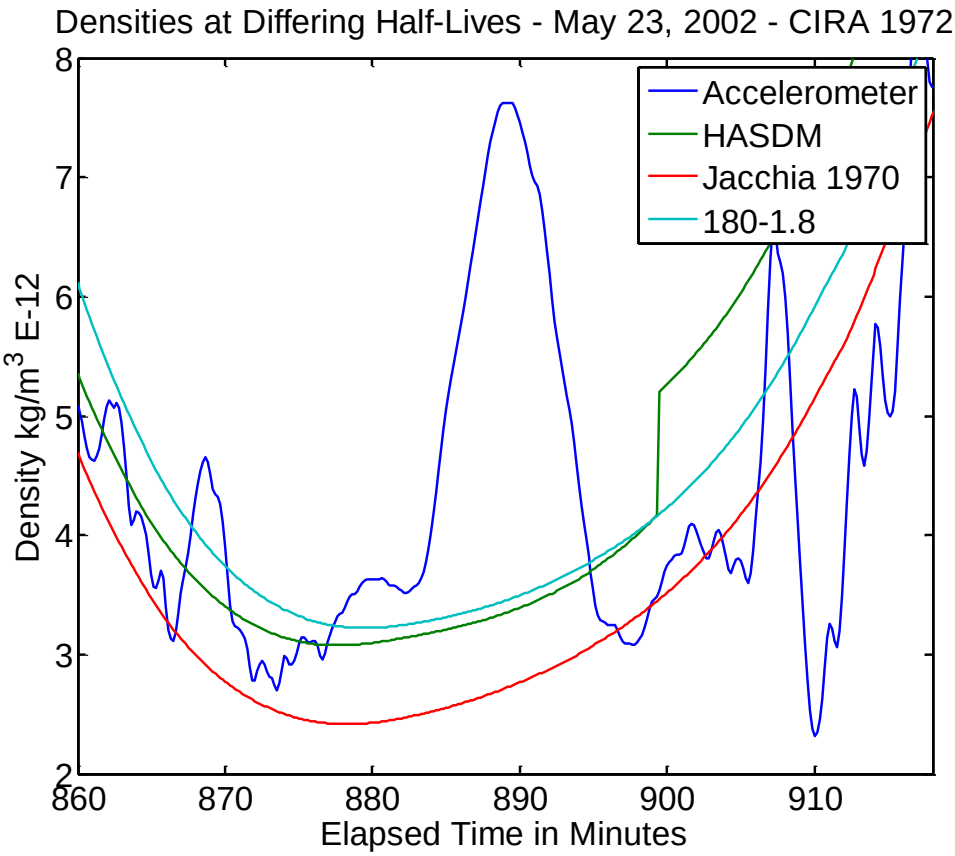

Figure 4.6: Nocturnal CHAMP Satellite Densities on May 23, 2002, Orbit 10
The TADs are seen constructively interfering at about 880 minutes into the day

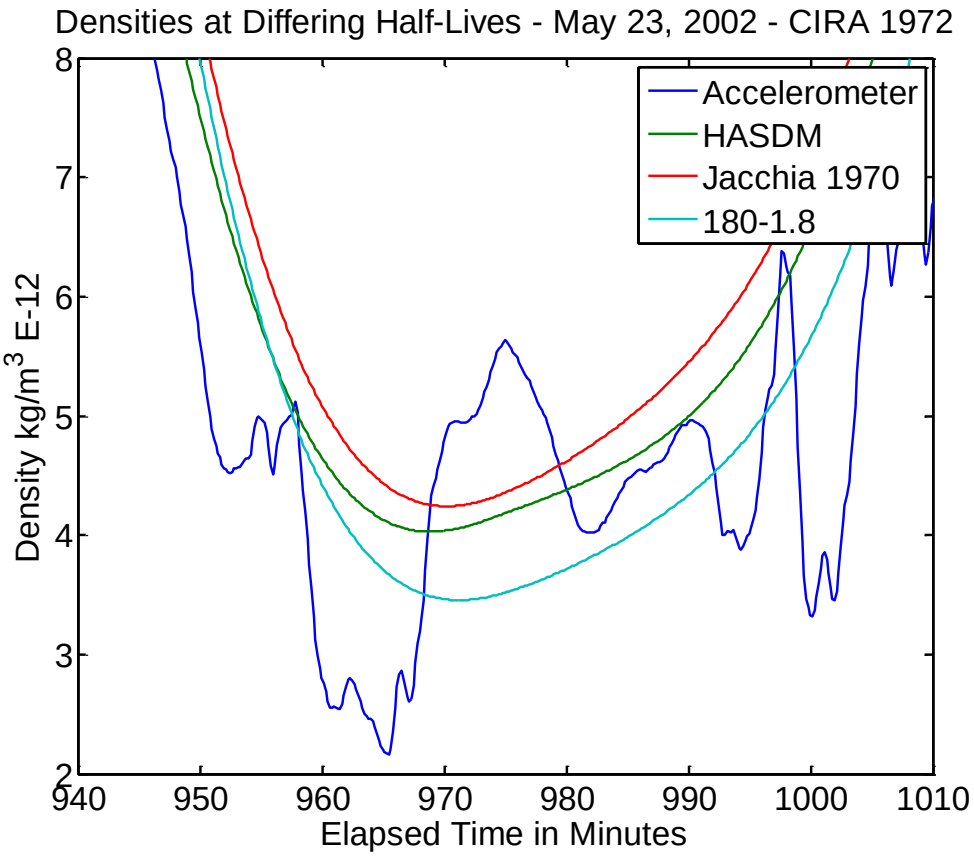

Figure 4.7: Nocturnal CHAMP Satellite Densities on May 23, 2002, Orbit 11
The TADs are moving past each other at this point and are visible at 975 minutes and 990 minutes respectively

As with the TADs seen on April 19th, none of the density models displayed in Figures 4.6-4.7 displayed any capability to model the travelling atmospheric disturbances. While the April 19th models showed what might be construed as a minor response to the TADs, the May 23rd models showed no indication of responding to the TADs. The model densities for May 23rd, decreased smoothly to a minimum value early in the nocturnal part of the orbit and then rose again in response to the diurnal heating.

4.4 Summary

There is relatively little to suggest that either the POE derived densities, the HASDM densities, or the empirical model densities are able to predict the appearance and characteristics of travelling atmospheric disturbances. The empirical model is not expected to display this behavior as it does not account for satellite measurements at all. Both the empirical model and HASDM are included for purposes of comparison and to demonstrate the effects of the underlying model. There are no localized increases in density that correspond to the increases seen due to the travelling atmospheric disturbances. During the period of constructive interference, the peak amplitudes of both POE derived densities and HASDM densities do appear to correspond with the peak associated with the constructive interference. The peak that appears to correspond to the constructive interference appears to simply be a product of the density models as it appears in the other three nocturnal passes as well.

5 OBSERVABILITY OF DENSITY INCREASES LOCALIZED AROUND THE NORTH GEOMAGNETIC POLE

In this section, the observability of localized increases to atmospheric density near the north geomagnetic pole is examined for selected geomagnetic polar passes that show significant and noticeable increases in density. This will be examined by using graphical representations of the CHAMP satellite's geomagnetic latitude, as well as a graphical representation of density values determined by the onboard accelerometer, HASDM, and the POE derived densities described earlier in this work. Only POE data corresponding to the two optimal orbit determination configurations are used, these two configurations are of a baseline CIRA-1972 model, with a ballistic coefficient correlation half-life of 1.8 minutes and density correlation half-lives of 18 and 180 minutes respectively.

5.1 Geomagnetic Pole Passes from April 19, 2002

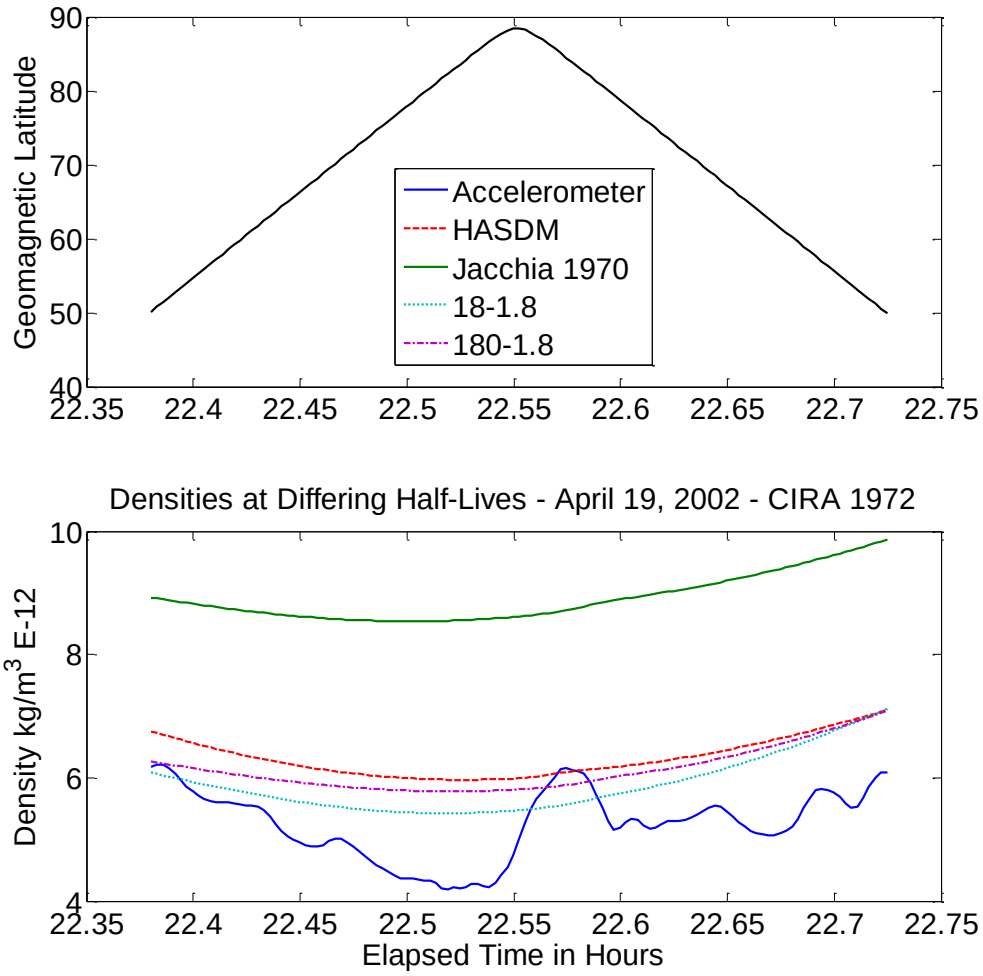

Figure 5.1: CHAMP Geomagnetic Pole Pass at Approximately 22:30 UTC April 19, 2002

An atmospheric density peak is observable at 22:33 UTC.

HASDM and POE derived densities are much closer to values for atmospheric density derived from accelerometer measurements than the empirical Jacchia 1971

model, though none of the density estimates show any indication of modeling this geomagnetic cusp phenomena in Figure 5.1.

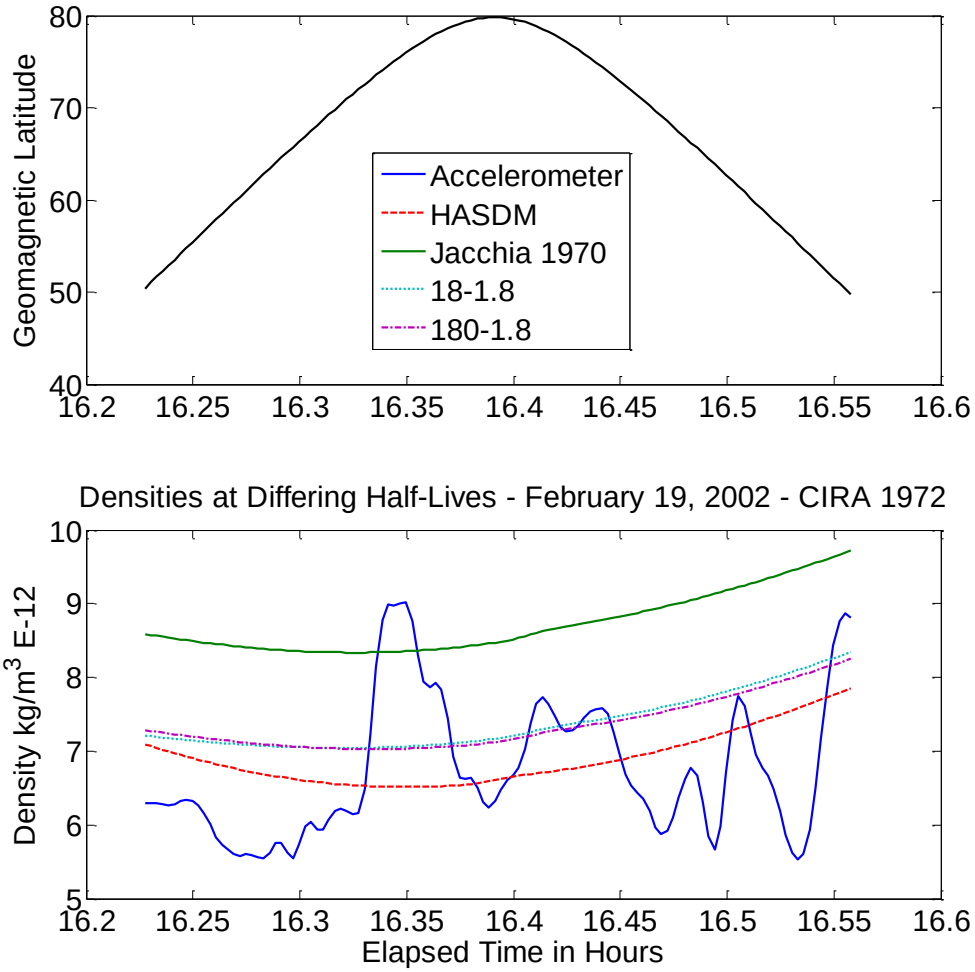

Figure 5.2: CHAMP Geomagnetic Pole Pass at Approximately 16:24 UTC April 19, 2002

Atmospheric density peaks are observable in accelerometer data at 16:21 and 16:26 UTC.

Again, HASDM and POE derived densities are much closer to values for atmospheric density derived from accelerometer measurements than the empirical

Jacchia 1971 model, and none of the density estimates show any indication of modeling this geomagnetic cusp phenomena in Figure 5.2.

5.2 Geomagnetic Pole Pass from March 21, 2003

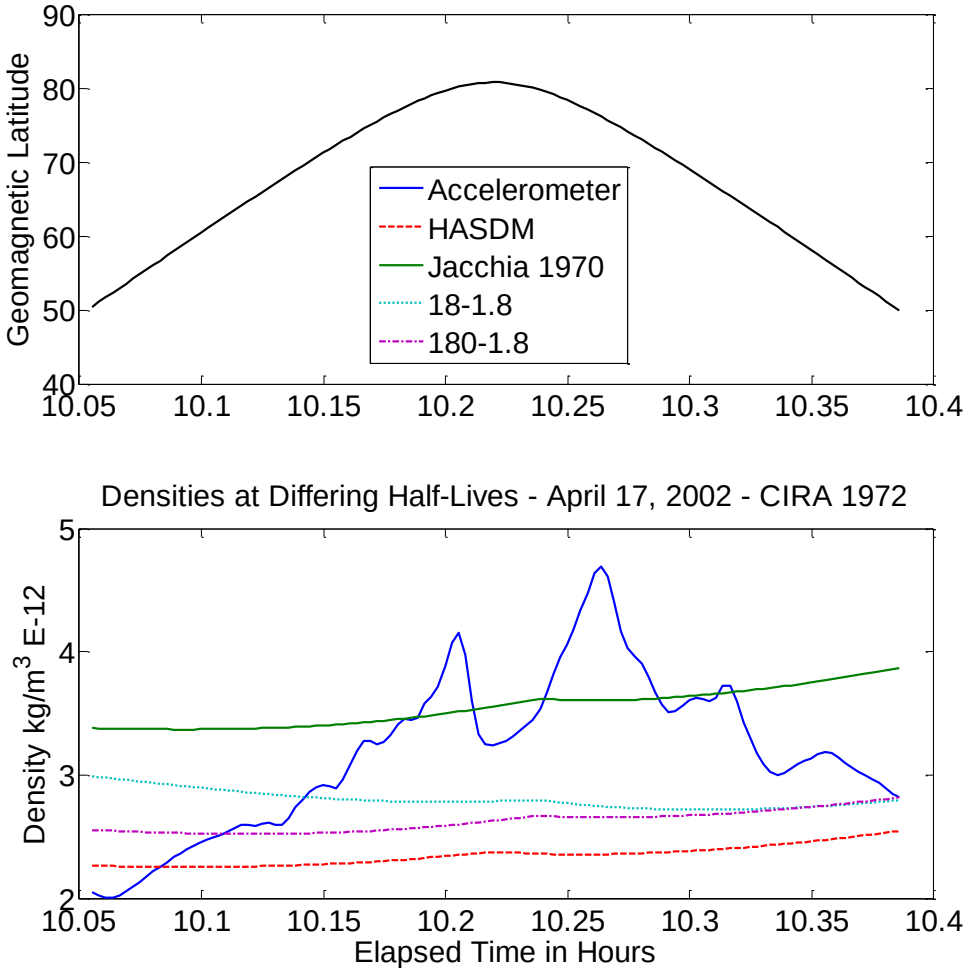

Figure 5.3: CHAMP Geomagnetic Pole Pass at Approximately 10:14 UTC March 21, 2002

Atmospheric density peaks are observable in accelerometer data at 10:12 and 10:16 UTC.

All density models show a minor peak near the maximum latitude the satellite reaches. However, this does not correspond with either of the density increases of either side this peak in Figure 5.3.

5.3 Geomagnetic Pole Pass from February 19, 2002

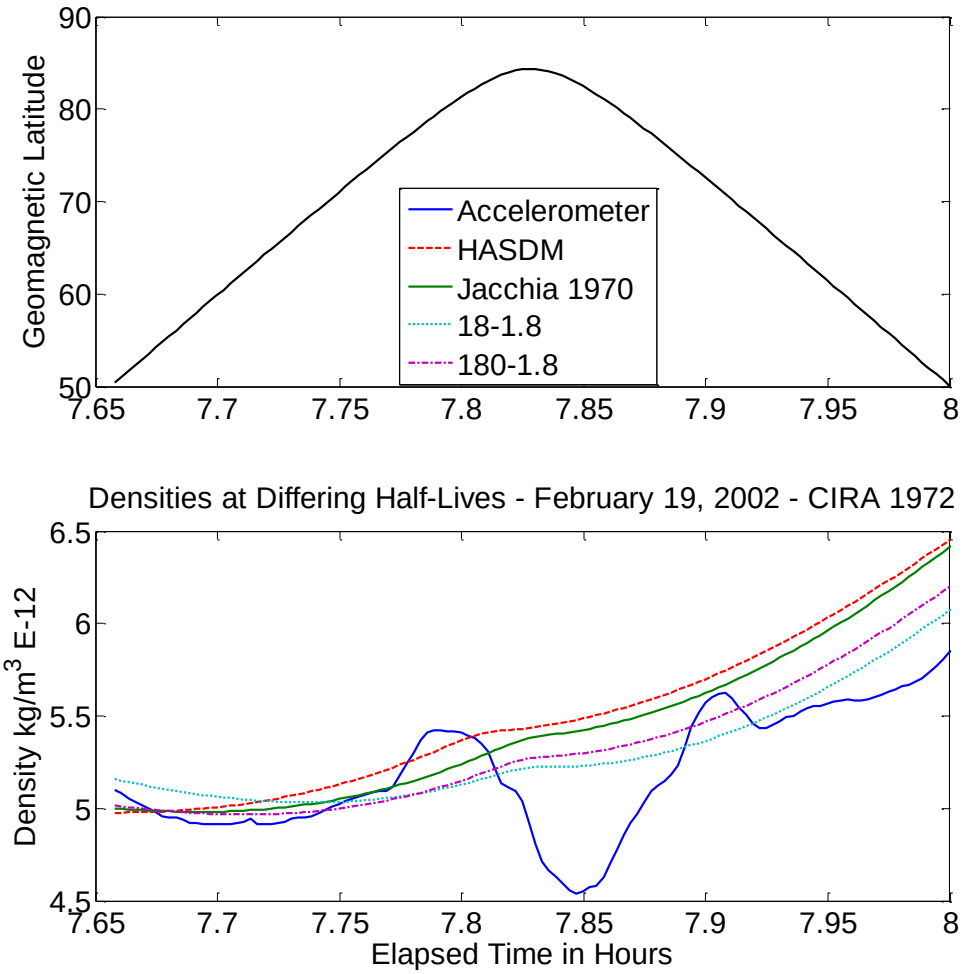

Figure 5.4: CHAMP Geomagnetic Pole Pass at Approximately 7:50 UTC February 19, 2002

Atmospheric density peaks are observable in accelerometer data at 10:12 and 10:16 UTC.

All density models show a minor peak following the first pass over the geomagnetic cusp, though the depression between the geomagnetic cusps is not characterized in any of the density models in Figure 5.4. The density models show a significant increase in density following the pass over the geomagnetic pole as the CHAMP satellite moves to the lit side of the Earth.

5.4 Summary

The lack of corresponding density peaks in the above figures indicates that the POE derived densities have a difficult time modeling geomagnetic cusp features. Both the empirical Jacchia 1971 and HASDM densities also do very little to model these very short term perturbations. At some points, the geomagnetic cusps are observable in the accelerometer data on either side of the geomagnetic pole, and at one point the cusp is only seen on the later side of the geomagnetic pole. The temporal resolution of these density models is obviously not of sufficient quality to model the density perturbations as is, this may be improved by acquiring POE data in more frequent intervals, though this would increase the computing load for applications that are intended to be more long term.

6 EXAMINATION OF COPLANAR PERIODS OF CHAMP AND GRACE SATELLITES

In this study, only the dates surrounding April 3, 2005 are examined to determine what similarities can be observed between the two satellites. During the time period examined, the orbits of the two satellites were roughly synchronous three times. Once during the later part of April 1, 2005, and then roughly every two days following this first period; the later part of April 3, 2005, and the later part of April 5, 2005. CHAMP's lower orbit causes it to move faster and pass the GRACE satellites along the satellite track. Eventually the CHAMP satellite completes one orbit more than the GRACE satellites, and they are then synchronous again. By examining these synchronous periods, effects that are solely a function of altitude are isolated

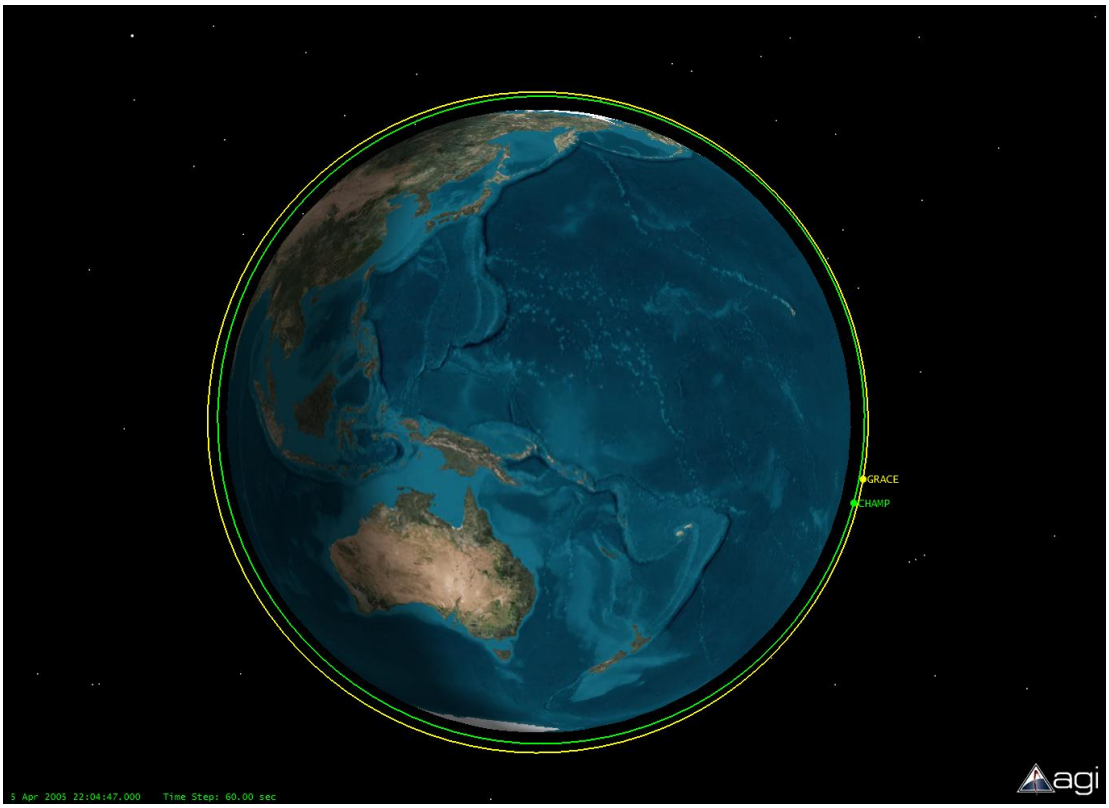

Figure 6.1: CHAMP and GRACE Satellite Orbits during Coplanar Periods
At this point, the orbits are concentric and synchronous. This lasts only a few hours before the CHAMP and GRACE satellites are too far apart to be observing similar points in the atmosphere. The yellow line represents the two GRACE satellites which are at a higher orbit than the CHAMP satellite represented by the green line.

6.1 CC and RMS Values for the Coplanar Period near April 3, 2005

Table 6.1: Cross Correlation Coefficients for CHAMP near April 3, 2005.
The total duration is given in minutes, and both the HASDM and Empirical Jacchia 1971 cross correlations are given. Yellow (light gray) indicators are the best cross correlation coefficients for the given baseline density model, and the Orange (darker gray) indicates the best overall cross correlation.

	Total Duration	A_p avg	$F_{10.7}$ avg	Bowman	Empirical
	8378	28.20	86.10	0.9346	0.9151
Half Lives (min) Density/Ballistic	CIRA 1972	Jacchia 1971	Jacchia-Roberts	MSISE 1990	NRLMSISE 2000
1.8-1.8	0.9333	0.9319	0.9323	0.9276	0.9273
1.8-18	0.9307	0.9299	0.9302	0.9252	0.9245
1.8-180	0.9267	0.9261	0.9263	0.9231	0.9225
18-1.8	0.9381	0.9372	0.9375	0.9279	0.9275
18-18	0.9381	0.9375	0.9377	0.9275	0.9268
18-180	0.9365	0.9359	0.9362	0.9266	0.9259
180-1.8	0.9389	0.9390	0.9390	0.9281	0.9281
180-18	0.9380	0.9383	0.9383	0.9272	0.9269
180-180	0.9386	0.9388	0.9388	0.9275	0.9272

Table 6.2: Root-Mean-Squared Values for CHAMP near April 3, 2005.
The total duration is given in minutes, and both the HASDM and Empirical Jacchia 1971 RMS values are given. Yellow (light gray) indicators are the best RMS values for the given baseline density model, and the Orange (darker gray) indicates the best overall RMS values. All RMS values are given in 10^{-12} kg/m^3.

	Total Duration	A_p avg	$F_{10.7}$ avg	Bowman	Empirical
	8378	28.20	86.10	0.4880	0.7202
Half Lives (min) Density/Ballistic	CIRA 1972	Jacchia 1971	Jacchia-Roberts	MSISE 1990	NRLMSISE 2000
1.8-1.8	0.4953	0.5062	0.5026	0.7184	0.7118
1.8-18	0.5280	0.5238	0.5248	0.7031	0.7021
1.8-180	0.5742	0.5713	0.5728	0.6954	0.6944
18-1.8	0.4801	0.5070	0.4992	0.7314	0.7190
18-18	0.4768	0.4933	0.4882	0.7164	0.7088
18-180	0.4881	0.4936	0.4915	0.6967	0.6920
180-1.8	0.4806	0.5032	0.4967	0.7364	0.7243
180-18	0.4827	0.4955	0.4915	0.7306	0.7237
180-180	0.4796	0.4857	0.4834	0.7224	0.7186

Seen in Table 6.1 and Table 6.2, the POE derived densities possessed better CC and RMS values than both the HASDM and empirical Jacchia 1971 densities for the CHAMP satellite during this time period,. CHAMP data follows trends seen above in that optimal RMS and CC values belong to the three Jacchia based baseline density models. The optimal RMS values occur at a density correlation half-life of 180 minutes, and a ballistic coefficient correlation half-life of 1.8 minutes. Optimal CC values for CHAMP occur at slightly different half-lives, at a density correlation half-life of 18 minutes, and a ballistic coefficient correlation half-life of 18 minutes. This deviates from previous findings for optimal schemes for density estimates in which they match those found for the CHAMP RMS values. This deviation is likely a random deviation from optimal characteristics over the long term as the data in question is restricted to a short time period of six days. For this reason, the densities displayed will be those for a density correlation half-life of 180 minutes, and a ballistic coefficient half-life of 1.8 minutes.

Table 6.3: Cross Correlation Coefficients for GRACE near April 3, 2005.
The total duration is given in minutes, and both the HASDM and Empirical Jacchia 1971 cross correlations are given. Yellow (light gray) indicators are the best cross correlation coefficients for the given baseline density model, and the Orange (darker gray) indicates the best overall cross correlation.

	Total Duration	A_p avg	$F_{10.7}$ avg	Bowman	Empirical
	8378	28.20	86.10	0.8979	0.8812
Half Lives (min) Density/Ballistic	CIRA 1972	Jacchia 1971	Jacchia-Roberts	MSISE 1990	NRLMSISE 2000
1.8-1.8	0.8946	0.8950	0.8933	0.8933	0.8950
1.8-18	0.8965	0.8967	0.8958	0.8924	0.8930
1.8-180	0.8943	0.8944	0.8940	0.8901	0.8902
18-1.8	0.9110	0.9113	0.9104	0.9011	0.9023
18-18	0.9088	0.9090	0.9082	0.9000	0.9007
18-180	0.9039	0.9041	0.9034	0.8963	0.8968
180-1.8	0.9179	0.9180	0.9178	0.9049	0.9049
180-18	0.9155	0.9156	0.9154	0.9030	0.9027
180-180	0.9057	0.9058	0.9055	0.8972	0.8971

Table 6.4: Root-Mean-Squared Values for GRACE near April 3, 2005.
The total duration is given in minutes, and both the HASDM and Empirical Jacchia 1971 RMS values are given. Yellow (light gray) indicators are the best RMS values for the given baseline density model, and the Orange (darker gray) indicates the best overall RMS values. All RMS values are given in 10^{-12} kg/m^3.

	Total Duration	A_p avg	$F_{10.7}$ avg	Bowman	Empirical
	8378	28.20	86.10	0.0933	0.1729
Half Lives (min) Density/Ballistic	CIRA 1972	Jacchia 1971	Jacchia-Roberts	MSISE 1990	NRLMSISE 2000
1.8-1.8	0.1043	0.1054	0.1016	0.1733	0.1757
1.8-18	0.1183	0.1191	0.1160	0.1721	0.1741
1.8-180	0.1416	0.1420	0.1403	0.1734	0.1746
18-1.8	0.0897	0.0910	0.0866	0.1712	0.1740
18-18	0.0957	0.0969	0.0927	0.1721	0.1748
18-180	0.1163	0.1173	0.1136	0.1817	0.1841
180-1.8	0.0891	0.0903	0.0858	0.1705	0.1736
180-18	0.0939	0.0952	0.0907	0.1730	0.1763
180-180	0.1175	0.1188	0.1142	0.1959	0.1990

GRACE POE derived densities possess better CC and RMS qualities than HASDM and empirical Jacchia 1971 densities for the time period in question as shown in Table 6.3and Table 6.4. The optimal configuration schemes are restricted to the Jacchia based baseline models, and a density correlation half-life of 180 minutes, and a ballistic coefficient correlation half life of 1.8 minutes. This corresponds with what was found earlier in terms of optimal density estimation schemes. The MSIS based models have significantly worse CC and RMS values than the Jacchia based models.

6.2 Density Values for the CHAMP and GRACE Coplanar Time Period

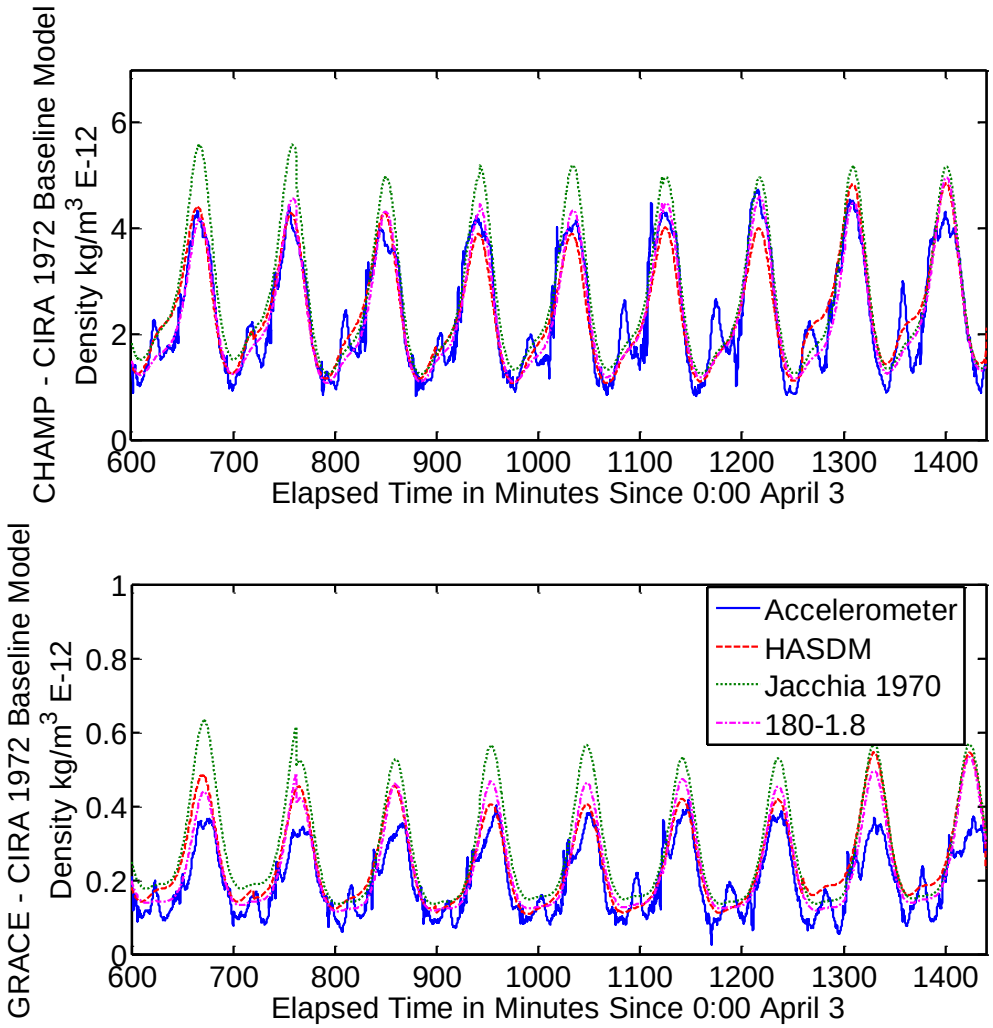

Figure 6.2: Densities Measured and Estimated for the CHAMP and GRACE Satellites on April 3, 2005

There are secondary peaks that arise about midway through the nocturnal halves of the orbit. These secondary nocturnal peaks can be seen in both the GRACE and CHAMP accelerometer derived densities in Figure 6.2. The estimated densities

have trouble characterizing these secondary peaks, much as the estimated densities were unable to characterize the travelling atmospheric disturbances (TAD) previously. Unlike the TADs in the Section 4, these peaks have a much greater relative increase over ambient densities at the time. This translates to the estimated densities showing a minor response in that minor peaks are observed as well as swifter initialization of the increasing density portion of the satellites' orbit.

The primary peaks that occur on the sunlit portion of the earth for the GRACE satellites appear truncated in respect to the estimated densities. The estimated densities for GRACE overshoot the accelerometer derived densities by a significant amount during every orbit. These truncations are not as severely apparent in the CHAMP accelerometer derived densities which are much better modeled by the different variations of estimated densities.

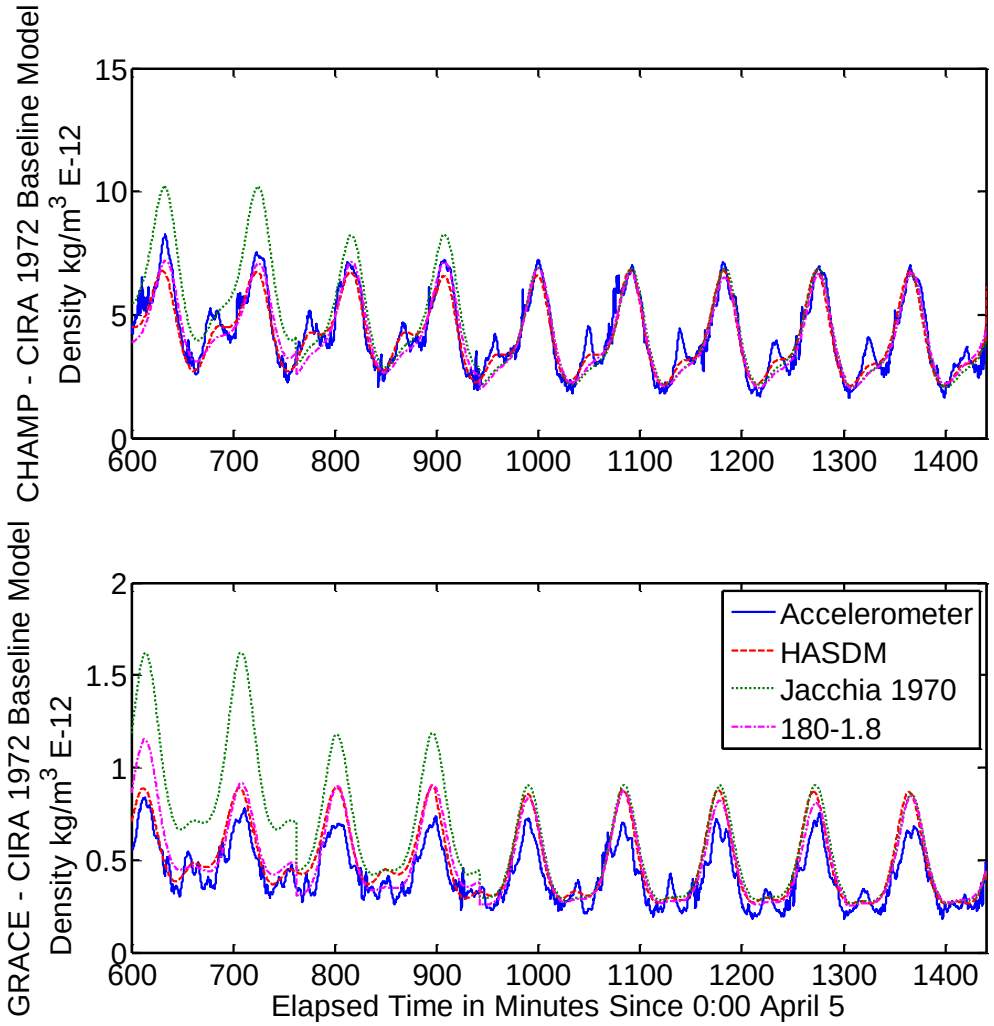

Figure 6.3: Densities Measured and Estimated for the CHAMP and GRACE Satellites on April 5, 2005

The nocturnal peaks from April 3rd are still apparent during April 5th, though their relative amplitudes appear greatly diminished for the GRACE data. The amplitudes for the secondary nocturnal peaks for the CHAMP satellite, however, are still readily apparent in the accelerometer derived densities seen in Figure 6.3. The estimated densities exhibit behavior similar to that observed for the data from April

3rd in that there are minor peaks that may be observed as well as a more rapid response in the increasing density portion of the orbit due to these secondary peaks.

The truncated primary peaks again appear in the GRACE accelerometer derived densities, and again, the estimated densities overshoot the accelerometer derived densities for the GRACE satellite. The truncation is much less readily visible in the CHAMP accelerometer derived densities, and as such, the estimated densities approximate the observed densities much more closely.

7 EXTENSION OF POE DENSITY DERIVATION TECHNIQUES TO THE TERRASAR-X SATELLITE

In addition to the GRACE and CHAMP satellites, other satellites are capable of generating precision orbit ephemerides. One of these satellites is the TerraSAR-X satellite, which has rapid science orbit (RSO) data available from GFZ-Potsdam, much like data available for the CHAMP and GRACE satellites. The TerraSAR-X satellite is a German satellite designed to perform radar based Earth observations, and unlike the CHAMP and GRACE satellites, the TerraSAR-X does not possess an accelerometer. The optimal orbit determination configuration determined from the cross correlation and root-mean-squared values for the CHAMP and GRACE satellites was applied to the TerraSAR-X satellite in order to model corrections to atmospheric density at the TerraSAR-X's operating altitude. The TerraSAR-X was launched from the Baikonur Cosmodrome in Kazakhstan on June 15th, 2007 [Ref. 58]. The orbits for the CHAMP, GRACE, and TerraSAR-X satellites were examined for the period of September 21-30, 2007. During this period, CHAMP had an altitude of about 360 km, GRACE had an altitude of about 473 km, and TerraSAR-X had an altitude of about 528 km.

7.1 CC and RMS Values for CHAMP and GRACE for September 21-30, 2007

Table 7.1: Cross Correlation Coefficients for CHAMP for September 21-30, 2007.
The total duration is given in minutes, and both the HASDM and Empirical Jacchia 1971 cross correlations are given. Yellow (light gray) indicators are the best cross correlation coefficients for the given baseline density model, and the Orange (darker gray) indicates the best overall cross correlation.

	Total Duration	A_p avg	$F_{10.7}$ avg	HASDM	Empirical
	11732	19.43	66.93	0.9219	0.9138
Half Lives (min) Density/Ballistic	CIRA 1972	Jacchia 1971	Jacchia-Roberts	MSISE 1990	NRLMSISE 2000
1.8-1.8	0.9130	0.9109	0.9072	0.9119	0.9110
1.8-18	0.9216	0.9221	0.9208	0.9163	0.9162
1.8-180	0.9192	0.9195	0.9189	0.9158	0.9158
18-1.8	0.9292	0.9284	0.9276	0.9239	0.9244
18-18	0.9273	0.9270	0.9261	0.9220	0.9225
18-180	0.9195	0.9204	0.9196	0.9143	0.9148
180-1.8	0.9368	0.9363	0.9364	0.9282	0.9292
180-18	0.9339	0.9337	0.9337	0.9253	0.9264
180-180	0.9139	0.9134	0.9124	0.9074	0.9080

Table 7.2: Root-Mean-Squared Values for CHAMP for September 21-30, 2007.
The total duration is given in minutes, and both the HASDM and Empirical Jacchia 1971 RMS values are given. Yellow (light gray) indicators are the best RMS values for the given baseline density model, and the Orange (darker gray) indicates the best overall RMS values. All RMS values are given in 10^{-12} kg/m^3.

	Total Duration	A_p avg	$F_{10.7}$ avg	HASDM	Empirical
	11732	19.43	66.93	0.4103	1.2446
Half Lives (min) Density/Ballistic	CIRA 1972	Jacchia 1971	Jacchia-Roberts	MSISE 1990	NRLMSISE 2000
1.8-1.8	0.5447	0.5136	0.5092	0.6871	0.6569
1.8-18	0.7764	0.7361	0.7144	0.9094	0.8866
1.8-180	1.0305	1.0194	1.0080	1.1165	1.1053
18-1.8	0.4496	0.4559	0.4657	0.6021	0.5658
18-18	0.5020	0.4745	0.4651	0.6854	0.6492
18-180	0.7654	0.7264	0.7023	0.9511	0.9235
180-1.8	0.4275	0.4445	0.4601	0.5518	0.5172
180-18	0.4525	0.4410	0.4446	0.6013	0.5643
180-180	0.6516	0.5921	0.5700	0.8456	0.8089

Table 7.3: Cross Correlation Coefficients for GRACE for September 21-30, 2007.
The total duration is given in minutes, and both the HASDM and Empirical Jacchia 1971 cross correlations are given. Yellow (light gray) indicators are the best cross correlation coefficients for the given baseline density model, and the Orange (darker gray) indicates the best overall cross correlation.

	Total Duration	A_p avg	$F_{10.7}$ avg	HASDM	Empirical
	11732	19.43	66.93	0.7707	0.7530
Half Lives (min) Density/Ballistic	CIRA 1972	Jacchia 1971	Jacchia-Roberts	MSISE 1990	NRLMSISE 2000
1.8-1.8	0.6907	0.6951	0.6846	0.7131	0.6983
1.8-18	0.7417	0.7433	0.7393	0.7348	0.7267
1.8-180	0.7637	0.7639	0.7634	0.7511	0.7487
18-1.8	0.6936	0.6986	0.6870	0.7017	0.6937
18-18	0.7120	0.7162	0.7063	0.7133	0.7067
18-180	0.7449	0.7475	0.7411	0.7357	0.7315
180-1.8	0.8071	0.8080	0.8058	0.7793	0.7812
180-18	0.8081	0.8090	0.8068	0.7794	0.7814
180-180	0.8097	0.8105	0.8085	0.7800	0.7820

Table 7.4: Root-Mean-Squared Values for GRACE for September 21-30, 2007.
The total duration is given in minutes, and both the HASDM and Empirical Jacchia 1971 RMS values are given. Yellow (light gray) indicators are the best RMS values for the given baseline density model, and the Orange (darker gray) indicates the best overall RMS values. All RMS values are given in 10^{-12} kg/m^3.

	Total Duration	A_p avg	$F_{10.7}$ avg	HASDM	Empirical
	11732	19.43	66.93	0.0305	0.1161
Half Lives (min) Density/Ballistic	CIRA 1972	Jacchia 1971	Jacchia-Roberts	MSISE 1990	NRLMSISE 2000
1.8-1.8	0.0589	0.0599	0.0580	0.0732	0.0704
1.8-18	0.0688	0.0697	0.0678	0.0819	0.0794
1.8-180	0.0912	0.0916	0.0907	0.0981	0.0967
18-1.8	0.0388	0.0396	0.0382	0.0524	0.0491
18-18	0.0402	0.0411	0.0394	0.0546	0.0512
18-180	0.0470	0.0481	0.0460	0.0621	0.0589
180-1.8	0.0298	0.0307	0.0290	0.0454	0.0414
180-18	0.0305	0.0315	0.0296	0.0464	0.0425
180-180	0.0317	0.0327	0.0307	0.0481	0.0441

The POE derived densities for the CHAMP satellite indicated in Table 7.1 and Table 7.2 that the optimal orbit determination scheme was attained using a baseline density model of CIRA-1972, a density correlation half-life of 180 minutes, and a ballistic coefficient correlation half-life of 1.8 minutes. The values obtained for the GRACE satellite are less clear. In Table 7.3 the cross correlation for the GRACE densities progressively increases to a maximum at density and ballistic coefficient correlation half-lives of 180 minutes each, a result not previously observed in RMS values for other days. In Table 7.4 the root-mean-squared values for the GRACE satellite better correspond to previously determined RMS results in that the optimal values occur at a density correlation half-life of 180 minutes, and a ballistic coefficient correlation half-life of 1.8 minutes. The CC and RMS values determined for HASDM for the GRACE satellite are similar to the values determined for the POE derived densities, though slightly worse. The TerraSAR-X satellite POE derived densities were examined for a baseline model of CIRA-1972, a density correlation half-life of 180 minutes, and a ballistic coefficient half-life of 1.8 minutes.

7.2 Density Values for September 26-27, 2007

The estimated corrections to density values, as well as the baseline model of Jacchia-1971, and the accelerometer derived densities where available are displayed below in Figure 7.1.

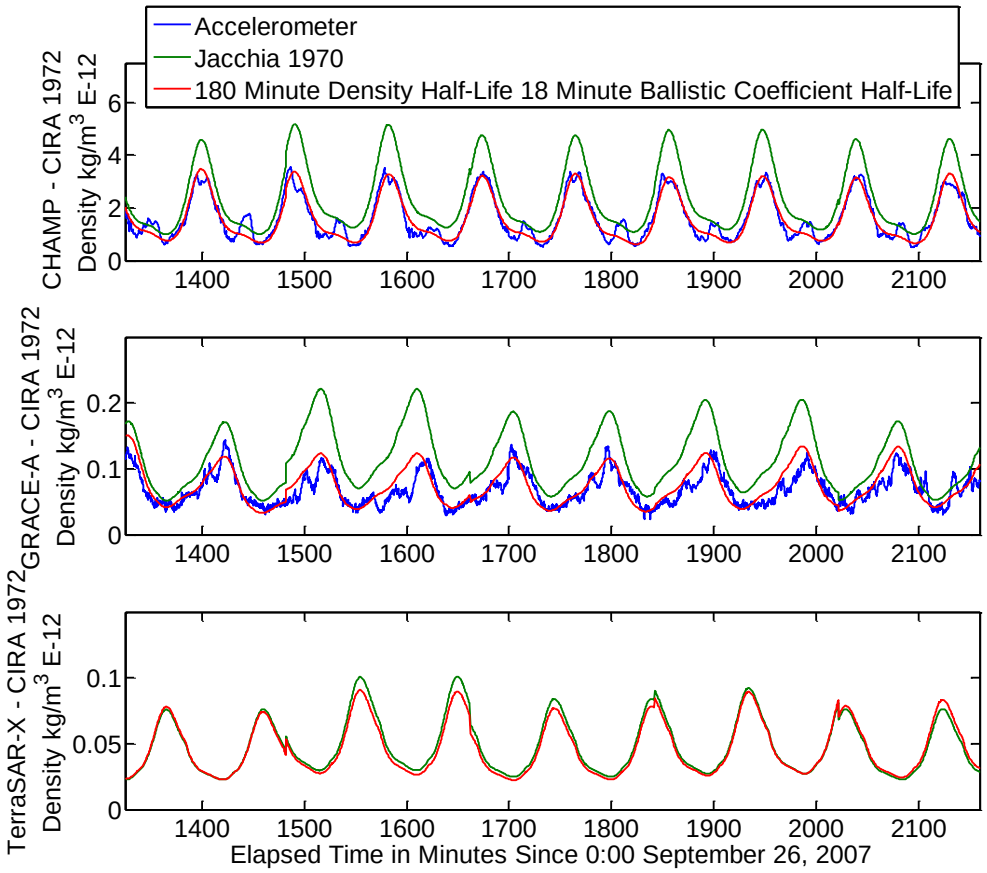

Figure 7.1: Estimated and Measured Densities for CHAMP, GRACE, and TerraSAR-X, September 26-27, 2007

For the CHAMP and GRACE data in the first and second plots of Figure 7.1, the estimated corrections to the existing models quite obviously performed better than the empirical model which greatly overestimates the atmospheric density during every orbit cycle. This reason, and the large variability of the atmospheric density measured along the GRACE satellites' orbit, may contribute to the CC and RMS values for GRACE being lower than would be expected. The estimated corrections to the baseline density model for TerraSAR-X show less deviation from the empirical models, which may be due to the higher altitude of the TerraSAR-X satellite. The estimated corrections deviate from the empirical model most during the 3^{rd}-5^{th} orbits, during which the atmospheric density appears noticeably lower than the empirical model predictions.

7.3 Density Values for September 29-30, 2007

The estimated corrections to density values, as well as the baseline model of Jacchia-1971, and the accelerometer derived densities where available are displayed below in Figure 7.2.

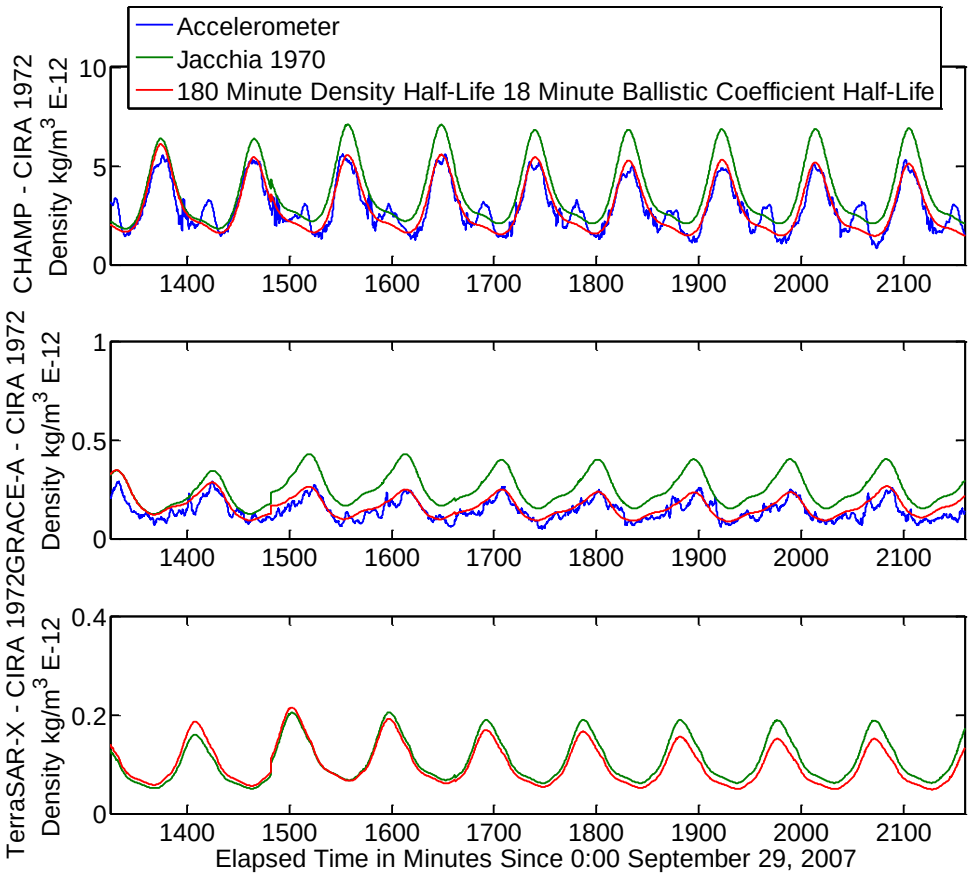

Figure 7.2: Estimated and Measured Densities for CHAMP, GRACE, and TerraSAR-X, September 29-30, 2007

The corrections made for the CHAMP and GRACE densities in plots 1 and 2 of Figure 7.2 show significant improvement over empirical models for the same time period, which greatly overestimate the density values, particularly for the path of the GRACE satellite. The deviations from the empirical densities for the TerraSAR-X satellite are relatively less severe than those for the CHAMP and GRACE satellites. This may be due in part to the orbit of the TerraSAR-X satellite being roughly 50km higher than the GRACE satellite, which is in turn higher in altitude than the CHAMP satellite. The CHAMP accelerometer data shows secondary density increases during the nighttime passes of the satellite. These density increases are not characterized in the POE derived densities, and are unobservable in the GRACE data. It was therefore not expected for the TerraSAR-X POE derived densities to exhibit these secondary increases in density.

8 SUMMARY, CONCLUSIONS, AND FUTURE WORK

8.1 Summary

Many of the current empirical models of atmospheric density in today's world are based primarily on altitude and solar activity, yet most possess significant errors when compared to data determined from actual satellite measurements. One of the greatest uncertainties in orbit determination has been drag, which is largely influenced by atmospheric density. There are many factors which affect the variability of atmospheric densities, and some of these factors are well modeled, such as atmospheric heating and to some degree the solar and geomagnetic activity levels, though some variations are not modeled at all.

This research used precision orbit ephemerides (POE) in an optimal orbit determination scheme to generate corrections to these existing density models to better characterize observations of satellites in low earth orbit (LEO). This orbit determination process can be utilized to produce more accurate satellite drag calculations, improve orbit determination and prediction, and provide a better understanding of the atmospheric density of our planet.

These corrections were compared to accelerometer derived densities that are available for the CHAMP and GRACE satellites. These corrections were analyzed by determining the cross correlation coefficients, and root-mean-squared values of these estimated corrections as compared to the accelerometer derived densities for these satellites for time periods spanning 2001 to 2007 and a range of seasons, solar

activity, and geomagnetic activity. The solar and geomagnetic activity levels were separated into different bins as follows in Table 8.1:

Table 8.1: Defined Solar and Geomagnetic Activity Bins

$F_{10.7}$ Solar Activity			A_p Geomagnetic Activity	
Low	$F_{10.7}<75$		Quiet	$A_p<10$
Moderate	$75<F_{10.7}<150$		Moderate	$10<A_p<50$
Elevated	$150<F_{10.7}<190$		Active	$50<A_p$
High	$190<F_{10.7}$			

The orbit determination program, ODTK, used a sequential Kalman filter/smoother scheme to process measurements of the satellites in question. Five baseline atmospheric models were examined for this research: Jacchia 1971, Jacchia-Roberts, Committee on Space Research (COSPAR) International Reference Atmosphere (CIRA 1972), Mass Spectrometer Incoherent Scatter (MSISE 1990), and Naval Research Laboratory Mass Spectrometer Incoherent Scatter (NRLMSISE 2000). The density correlation half-life and ballistic coefficient correlation half-life were varied as user specified parameters in the orbit determination scheme between the values of 1.8, 18, and 180 minutes. This resulted in 45 unique cases for the orbit determination process for each scenario that was examined. The resulting densities were compared to densities derived from accelerometer measurements by Sean Bruinsma at the Centre National d'Études Spatiales (CNES). These accelerometer derived densities were also compared to estimated densities supplied by Bruce Bowman of the U.S. Space Command for the High Accuracy Satellite Drag Model (HASDM).

ODTK calculated residuals for each orbit determination scenario which were easily analyzed for the McReynolds' Filter-Smoother Consistency test. The residuals plot allows a check for measurements that are inconsistent with previous measurements. In general the consistency test was passed by every set of measurements unless the initial conditions for the scenario were inaccurate. The only notable exception of this test occurred during a period when the geomagnetic and solar activity levels rapidly changed from relatively quiet to very active, causing the orbit determination scheme to have a short period of adjustment.

The cross correlation coefficient compares the density value change rates for both the accelerometer derived densities and the POE derived densities and is an excellent measurement of precision of an orbit determination scheme. The root-mean-squared (RMS) values measure the average deviation from the accelerometer data for all data points considered in a scenario. RMS values give a measure of how accurate the orbit determination scheme is, and is another measure of how well the POE derived densities characterize actual densities.

Two different sources of short term density variations were examined in this research: travelling atmospheric disturbances (TAD), which propagate from the poles towards the equator; and geomagnetic cusps, which are localized density increases near the geomagnetic poles where magnetic geopotential lines interact with the ionosphere to increase atmospheric density. The specific variations examined had temporal spans of between four and ten minutes, and less than three minutes respectively for the different phenomena examined. Density variations of shorter

duration are difficult to observe even in accelerometer data due to diurnal variations that arise from cyclical density increases due to the satellite passing from the darkened side of the earth to the lit side.

This research observed vertically propagating atmospheric density increases by examining periods of time during which both the GRACE and CHAMP satellites possessed the same orbital plane, during which perturbations can be examined for their capability to extend vertically through the atmosphere, as well as their observability in POE derived densities. The cross correlation and root mean squared values were determined for dates encompassing the range in question, and actual density values were graphically examined for time periods during which both the CHAMP and GRACE satellites had nearly synchronous orbits. This occurred at an interval of about every two days, as the CHAMP satellite outpaced the two GRACE satellites, and eventually completed an extra orbit.

Additionally, this research extends the application of optimal orbit determination techniques to an additional satellite, TerraSAR-X, which lacks an accelerometer. The optimal orbit determination scheme determined by the CHAMP and GRACE satellites was applied to the POE data available for the TerraSAR-X satellite and used to model corrections to atmospheric density models along the path of the TerraSAR-X satellite.

8.2 Conclusions

The following conclusions were reached as a result of this work

1. The Jacchia based models (Jacchia-1971, CIRA-1972, and Jacchia-Roberts), outperform Mass Spectrometer Incoherent Scatter based models (MSISE-1990 and NRLMSISE-200) as baseline density models for the techniques used in this research.

Table 8.2: Optimal CC Values for CHAMP at Varying Solar and Geomagnetic Activity Levels

Optimal Orbit Determination Schemes for CHAMP CC Values			
Activity Level	Baseline Model	Density Correlation Half-Life (min)	Ballistic Coefficient Correlation Half-Life (min)
Overall	Jacchia-1971	180	1.8
Quiet Geomagnetic	CIRA-1972	180	1.8
Moderate Geomagnetic	Jacchia-Roberts	180	1.8
Active Geomagnetic	CIRA-1972	18	1.8
Low Solar	Jacchia-1971	180	1.8
Moderate Solar	CIRA-1972	18	1.8
Elevated Solar	CIRA-1972	18	1.8
High Solar	CIRA-1972	180	1.8

Table 8.3: Optimal RMS Values for CHAMP at Varying Solar and Geomagnetic Activity Levels

Optimal Orbit Determination Schemes for CHAMP RMS Values			
Activity Level	Baseline Model	Density Correlation Half-Life (min)	Ballistic Coefficient Correlation Half-Life (min)
Overall	CIRA-1972	180	1.8
Quiet Geomagnetic	CIRA-1972	180	1.8
Moderate Geomagnetic	CIRA-1972	180	1.8
Active Geomagnetic	CIRA-1972	180	1.8
Low Solar	CIRA-1972	180	1.8
Moderate Solar	CIRA-1972	180	1.8
Elevated Solar	CIRA-1972	18	1.8
High Solar	CIRA-1972	180	1.8

2. Table 8.2 and Table 8.3 indicate that a ballistic coefficient correlation half-life of 1.8 minutes performs best for all levels of solar and geomagnetic activity.
3. Table 8.2 and Table 8.3 indicate that the optimal density correlation half-lives are either 180 or 18 minutes, though more often 180 minutes.
4. Table 8.3 shows that the CIRA-1972 baseline model outperforms all other baseline density models at all levels of solar and geomagnetic activity in terms of RMS.
5. Table 8.2 shows that the CIRA-1972 baseline model often outperforms other baseline density models, though it is outperformed by the Jacchia-1971 and Jacchia-Roberts baseline models for select levels of solar and geomagnetic activity.
6. POE derived atmospheric densities are unable to predict or characterize travelling atmospheric disturbances.

7. The secondary density increase in POE derived densities that is observed during the time of the travelling atmospheric disturbance is unrelated to the travelling atmospheric disturbance as it also manifests when no TAD is observable.
8. POE derived densities were unable to characterize the geomagnetic cusps observed at 22:33 UTC, April 19, 2002; 16:21 and 16:26 UTC, April 19, 2002; 10:12 and 10:16 UTC, March 21, 2003; and at 7:48 and 7:54 UTC, February 19, 2002.
9. Secondary density increases on the unlit side of the earth have a vertical range of at least 50 km, the approximate altitude differential between GRACE and CHAMP.
10. POE derived densities were unable to characterize these secondary density increases for the CHAMP and GRACE satellites.
11. POE density derivation can be applied to other satellites such as TerraSAR-X as a method of estimating atmospheric density corrections along the path of the satellite.
12. POE derived densities for the TerraSAR-X satellite have a maximum deviation from empirical models of roughly 10%.

POE derived densities show marked improvement over baseline density models, and yield results comparable to those of HASDM. The optimal orbit determination scheme configuration changes from case to case, but a few trends are

observed. 1) POE derived densities found using Jacchia based baseline models possess significantly better qualities than MSIS based baseline models. 2) A ballistic coefficient half life of 1.8 minutes nearly always has better characteristics than higher values. 3) The optimal density correlation half life is typically either 180 or 18 minutes. The three Jacchia based models all had very similar characteristics, and the choice of one model over another will not likely skew the results singificantly, however, the CIRA-1972 model tended to slightly outperform the other two Jacchia based models with some regularity.

Unfortunately, neither of the short term density variations examined in this work were observable by the POE derived densities. Minor changes in density appear to occur in response to variations, but are largely unable to characterize them.

The coplanar periods showed secondary density increases that occur on the unlit side of the earth. These increases were largely unseen in the POE derived densities, though the POE derived densities did show a slight response to the secondary peaks. The secondary density peaks were seen in both the GRACE and CHAMP accelerometer data, and likely existed both above and below the orbits of these two satellites.

For peak atmospheric density values, the TerraSAR-X densities found for the time period examined in this study using POE data showed deviations from the empirical density models of up to 10%. The CHAMP and GRACE POE derived densities showed a greater relative deviation from the empirical density models during peak density periods than during low density periods, and these deviations for

the CHAMP and GRACE satellites much better approximated the density values found using the accelerometers aboard both satellites. The TerraSAR-X satellite lacks an accelerometer, so the optimal combinations of baseline density values, density correlation half-life and ballistic coefficient half-life are determined from data obtained from the CHAMP and GRACE satellites.

8.3 Future Work

8.3.1 Considering Gravity Recovery and Climate Experiment (GRACE) Accelerometer Derived Density Data

Research akin to that performed for Section 3, but executed using the GRACE satellites would provide further verification for the results found there, which are currently limited to CHAMP satellite. Other satellites that possess sensitive accelerometers would also prove useful for this purpose.

Examination of the GRACE satellite allows investigation of the effect of altitude on the optimal orbit determination configuration. With increased altitude, the density decreases exponentially, and satellites may be more or less susceptible to rapid changes in density.

8.3.2 A More Detailed Examination of the Density and Ballistic Coefficient Correlated Half-Lives

This research examined density and ballistic coefficient correlation half-lives that varied by an order of ten. Intermediary half-lives between those already examined may yield still better results in terms of cross correlation and root-mean-squared values. The effect may prove to be negligible, but may also account for the optimal density correlation half-life at times being 180 minutes, and at times 18 minutes. Proposed future work would include the intervals being evenly divided into ten divisions, with CC and RMS values found for each division. Thus the values examined between 1.8 and 18 minutes would be 3.6, 5.4, 7.2, 9 minutes, etc.

8.3.3 Using the Jacchia-Bowman 2008 Atmospheric Model as a Baseline Model

Existing models available in ODTK consider solar and geomagnetic activity using supplied 3-hourly values in the form of $F_{10.7}$ and a_p values. There now exist satellites capable of measuring solar and geomagnetic activity on much shorter time scales, as well as being able to measure solar flux directly as opposed to measuring it via proxy. Very few atmospheric models are currently able to account for this data, though the 2008 Jacchia-Bowman model is able to do so. As the Jacchia-Bowman model takes into account a more thorough model of solar flux heating, the baseline density estimates would likely be much improved upon. This would yield a better starting point for derivation of densities based upon POE data.

8.3.4 Additional Satellites with Precision Orbit Ephemerides

Of the satellites with POE data, one has been examined in the method above so far, the TerraSAR-X. The TerraSAR-X was only examined for a short time period, and further examination is warranted to better understand densities at altitudes higher than those previously examined. There are a multitude of satellites which exist and have sufficient measurement systems to be used in the manner above. GPS receivers, in particular are useful as they provide continuous coverage of the satellite during its orbit, and can reach high position accuracies after post-processing of 5-10 cm. Other satellites that may be of interest include the Ice, Cloud, and Land Elevation Satellite (ICESat), Jason-1, and other Earth observation satellites whose

primary roles require accurate position measurements that can be used to estimate atmospheric density.

REFERENCES

1. J. M. Forbes, G. Lu, S. Bruinsma, S. Nerem, and X. Zhang, "Thermospheric Density Variations Due to the 15-24 April 2002 Solar Events from CHAMP/STAR Accelerometer Measurements," *Journal of Geophysical Research*, Vol. 110, 2005, pp. 1-9.
2. K. Schlegel, H. Luhr, J. P. St. Maurice, G. Crowley, and C. Hackert, "Thermospheric Density Structures over the Polar Regions Observed with CHAMP," *Annales Geophysicae*, Vol. 23, 2005, pp. 1659-1672.
3. S. Bruinsma and R. Biancale, "Total Densities Derived from Accelerometer Data," *Journal of Spacecraft and Rockets*, Vol. 40, No. 2, March-April 2003, pp. 230-236.
4. M. F. Storz, B. R. Bowman, Major J. I. Branson, S. J. Casali, and W. K. Tobiska, "High Accuracy Satellite Drag Model (HASDM)," *Advances in Space Research*, Vol. 36, Issue 12, 2005, pp. 2497-2505.
5. D. A. Vallado, *Fundamentals of Astrodynamics and Applications*, Microcosm Press, El Segundo, CA, 3rd Edition, 2007, Chap. 8, App. B.
6. A. C. Tribble, *The Space Environment: Implications for Spacecraft Design*, Princeton University Press, Princeton, New Jersey, 2003.
7. J. K. Hargreaves, *The Solar-Terrestrial Environment*, Cambridge University Press, Cambridge, 1992.
8. C. A. McLaughlin, "Upper Atmospheric Phenomena and Satellite Drag," *Advances in the Astronautical Sciences*, Vol. 123, AAS 05-315, Univelt, 2005, pp. 989-996.
9. C. Sabol and K. K. Luu, "Atmospheric Density Dynamics and the Motion of Satellites," *AMOS Technical Conference*, Wailea, HI, September 2002.
10. J. T. Emmert, J. M. Picone, J. L. Lean, and S. H. Knowles, "Global Change in the Thermosphere: Compelling Evidence of a Secular Decrease in Density," *Journal of Geophysical Research*, v. 109, 2004.
11. L. G. Jacchia, *Revised Static Models for the Thermosphere and Exosphere with Empirical Temperature Profiles*, SAO Special Report No. 332, Smithsonian Institution Astrophysical Observatory, Cambridge, MA, 1971.
12. C. E. Roberts, Jr., "An Analytic Model for Upper Atmosphere Densities Based upon Jacchia's 1970 Models," *Celestial Mechanics*, Vol. 4, Issue 3-4, December 1971, pp. 368-377.
13. COSPAR Working Group IV, *COSPAR International Reference Atmosphere*, Akademie-Verlag, Berlin, 1972.
14. A. E. Hedin, "Extension of the MSIS Thermosphere Model into the Middle and Lower Atmosphere," *Journal of Geophysical Research*, Vol. 96, 1991, pp. 1159-1172.
15. J.M. Picone, A. E. Hedin, D. P. Drob, "NRLMSISE-00 Empirical Model of the Atmosphere: Statistical Comparisons and Scientific Issues," *Journal of Geophysical Research*, Vol. 107, No. A12, 2002.
16. B. R. Bowman, W. K. Tobiska, F. A. Marcos, C. Y. Huang, C. S. Lin, W. J. Burke, "A New Empirical Thermospheric Density Model JB2008 Using New Solar and Geomagnetic Indices," AIAA 2008-6438, AIAA/AAS Astrodynamics Specialist Conference, Honolulu, HI, August 2008.

17. National Geophysical Data Center, *Solar Indices Bulletin*, Boulder, CO: National Geophysical Data Center, http://www.ngdc.noaa.gov/ and ftp://ftp.ngdc.noaa.gov/STP/SOLAR_DATA/SOLAR_RADIO/FLUX.
18. National Geophysical Data Center, *Solar Indices Bulletin*, Boulder, CO: National Geophysical Data Center, http://www.ngdc.noaa.gov/ and ftp://ftp.ngdc.noaa.gov/STP/GEOMAGNETIC_DATA/INDICES/KP_AP/.
19. S. Tanygin and J. R. Wright, "Removal of Arbitrary Discontinuities in Atmospheric Density Modeling," *Advances in the Astronautical Sciences*, Vol. 119 II, AAS 04-176, Univelt, 2004, pp. 1185-1196.
20. B. Bowman, F. A. Marcos, and M. J. Kendra, "A Method for Computing Accurate Atmospheric Density Values from Satellite Drag Data," *Advances in the Astronautical Sciences*, Vol. 119, AAS 04-173, Univelt, 2004, pp. 1117-1134.
21. B. Bowman, "The Semiannual Thermospheric Density Variation from 1970 to 2002 Between 200-1100 km," *Advances in the Astronautical Sciences*, Vol. 119, AAS 04-174, Univelt, 2004, pp. 1135-1154.
22. P. J. Cefola, R. J. Proulx, A. I. Nazarenko, and V. S. Yurasov, "Atmospheric Density Correction Using Two Line Element Sets as the Observation Data," *Advances in the Astronautical Sciences*, Vol. 116, AAS 03-626, Univelt, 2003, pp. 1953-1978.
23. V. S. Yurasov, A. I. Nazarenko, P. J. Cefola, and K. T. Alfriend, "Results and Issues of Atmospheric Density Correction," *Journal of the Astronautical Sciences*, Vol. 52, No. 3, July-September 2004, pp. 281-300.
24. V. S. Yurasov, A. I. Nazarenko, K. T. Alfriend, and P. J. Cefola, "Reentry Time Prediction Using Atmospheric Density Corrections," *Journal of Guidance, Control, and Dynamics*, Vol. 31, No. 2, March-April 2008, pp. 282-289.
25. M. P. Wilkins, C. A. Sabol, P. J. Cefola, and K. T. Alfriend, "Practical Challenges in Implementing Atmospheric Density Corrections to the NRLMSISE-00 Model," *Advances in the Astronautical Sciences*, Vol. 124, AAS 06-170, Univelt 2006, pp. 1113-1130.
26. M. P. Wilkins, C. A. Sabol, P. J. Cefola, and K. T. Alfriend, "Improving Dynamic Calibration of the Atmosphere," *Advances in the Astronautical Sciences*, Vol. 127, AAS 07-185, Univelt, 2007, pp. 1257-1272.
27. M. P. Wilkins, C. A. Sabol, P. J. Cefola, and K. T. Alfriend, "Validation and Application of Corrections to the NRLMSISE-00 Atmospheric Density Model," *Advances in the Astronautical Sciences*, Vol. 127, AAS 07-189, Univelt, 2007, pp. 1285-1304.
28. S. R. Mance, C. A. McLaughlin, F. G. Lemoine, D. D. Rowlands, and P. J. Cefola, "GEOSAT Follow-On Precision Orbit Improvement Through Drag Model Update," *Advances in the Astronautical Sciences*, Vol. 134, AAS 09-105, Univelt, 2009, pp. 43-62..
29. E. Doornbos, H. Klinkrad, and P. Visser, "Use of Two-Line Element Data for Thermosphere Neutral Density Model Calibration," *Advances in Space Research*, Vol. 41, 2008, pp. 1115-1122.
30. E. A. Rhoden, J. M. Forbes, and F. A. Marcos, "The Influence of Geomagnetic and Solar Variability on Lower Thermospheric Density," *Journal of Atmospheric and Solar-Terrestrial Physics*, Vol. 62, 2000, pp. 999-1013.
31. R. Konig and K. H. Neumayer, "Thermospheric Events in CHAMP Precise Orbit Determination," *First CHAMP Mission Results for Gravity, Magnetic and*

Atmospheric Studies, eds. C. Reigber, H. Luhr, P. Schwintzer, Springer, Berlin, 2003, pp. 112-119.
32. S. Bruinsma and R. Biancale, "Total Density Retrieval with STAR," *First CHAMP Mission Results for Gravity, Magnetic and Atmospheric Studies*, eds. C. Reigber, H. Luhr, P. Schwintzer, Springer, Berlin, 2003, pp. 192-199.
33. S. Bruinsma, S. D. Tamagnan and R. Biancale, "Atmospheric Densities Derived from CHAMP/STAR Accelerometer Observations," *Planetary and Space Science*, Vol. 52, 2004, pp. 297-312.
34. E. K. Sutton, R. S. Nerem, and J. M. Forbes, "Global Thermospheric Neutral Density and Wind Response to the Severe 2003 Geomagnetic Storms from CHAMP Accelerometer Data," *Journal of Geophysical Research*, Vol. 110, 2005.
35. E. K. Sutton, J. M. Forbes, R. S. Nerem, and T. N. Woods, "Neutral Density Response to the Solar Flares of October and November, 2003," *Geophysical Research Letters*, Vol. 33, 2006.
36. S. Bruinsma, J. M. Forbes, R. S. Nerem, and X. Zhang, "Thermospheric Density Response to the 20-21 November 2003 Solar and Geomagnetic Storm from CHAMP and GRACE Accelerometer Data," *Journal of Geophysical Research*, Vol. 111, No. AO6303, 2006, pp. 1-14.
37. S. L. Bruinsma and J. M. Forbes, "Storm-Time Equatorial Density Enhancements Observed by CHAMP and GRACE," *Journal of Spacecraft and Rockets*, Vol. 44, No. 6, 2007, pp. 1154-1159.
38. E. K. Sutton, R. S. Nerem, and J. M. Forbes, "Density and Winds in the Thermosphere Deduced from Accelerometer Data," *Journal of Spacecraft and Rockets*, Vol. 44, No. 6, 2007, pp. 1210-1219.
39. B. D. Tapley, J. C. Ries, S. Bettadpur, and M. Cheng, "Neutral Density Measurements for the Gravity Recovery and Climate Experiment Accelerometers," *Journal of Spacecraft and Rockets*, Vol. 44, No. 6, 2007, pp. 1220-1225.
40. S. L. Bruinsma and J. M. Forbes, "Medium- to Large-Scale Density Variability as Observed by CHAMP," *Space Weather*, Vol. 6, S08002, doi:10.1029/2008SW000411, 2008.
41. S. L. Bruinsma and J. M. Forbes, "Properties of Traveling Atmospheric Disturbances (TADs) Inferred from CHAMP Accelerometer Observations," *Advances in Space Research*, Vol. 43, 2009, pp. 369-376.
42. Y. L. Zhou, S. Y. Ma, H. Lühr, C. Xiong, and C. Reigber, "An Empirical Relation to Correct Storm-Time Thermospheric Mass Density Modeled by NRLMSISE-00 with CHAMP Satellite Air Drag Data," *Advances in Space Research*, Vol. 43, 2009, pp. 819-828.
43. E. Doornbos, H. Klinkrad, and P. Visser, "Atmospheric Density Calibration Using Satellite Drag Observations," *Advances in Space Research*, Vol. 36, 2005, pp. 515-521.
44. J. van den Ijssel, P. Visser, and R. Haagmans, "Determination of Non-Conservative Accelerations from Orbit Analysis," *Earth Observation with CHAMP Results from Three Years in Orbit*, eds. C. Reigber, H. Luhr, P. Schwintzer, J. Wickert, Springer, Berlin, 2005, pp. 95-100.
45. J. van den IJssel and P. Visser, "Determination of Non-Gravitational Accelerations from GPS Satellite-to-Satellite Tracking of CHAMP," *Advances in Space Research*, Vol. 36, 2005, pp. 418-423.

46. J. van den IJssel and P. Visser, "Performance of GPS-Based Accelerometry: CHAMP and GRACE," *Advances in Space Research*, Vol. 39, 2007, pp. 1597-1603.
47. O. Montenbruck, T. van Helleputte, R. Kroes, and E. Gill, "Reduced Dynamic Orbit Determination Using GPS Code and Carrier Measurements," *Aerospace Science and Technology*, Vol. 9, 2005, pp. 261-271.
48. P. Willis, F. Deleflie, F. Barlier, Y. E. Bar-Sever, and L. J. Romans, "Effects of Thermosphere Total Density Perturbations on LEO Orbits During Severe Geomagnetic Conditions (Oct-Nov 2003) Using DORIS and SLR Data," *Advances in Space Research*, Vol. 36, 2005, pp. 522-533.
49. C. A. McLaughlin and B. S. Bieber, "Neutral Density Determined from CHAMP Precision Orbits," *Advances in the Astronautical Sciences*, Vol. 129, AAS 07-260, Univelt, 2008, pp. 167-186.
50. C. A. McLaughlin, A. Hiatt, and B. S. Bieber, "Comparison of Total Density Derived from CHAMP Precision Orbits and CHAMP Accelerometer," *Advances in the Astronautical Sciences*, Vol. 130, AAS 08-177, Univelt, 2008, pp. 1193-1206.
51. C. A. McLaughlin, A. Hiatt, T. Lechtenberg, "Calibrating Precision Orbit Derived Total Density," AIAA 2008-6951, *2008 AIAA/AAS Astrodynamics Specialist Conference and Exhibit*, Honolulu, HI, August 2008.
52. A. Hiatt, C. A. McLaughlin, and T. Lechtenberg, "Deriving Density Estimates Using CHAMP Precision Orbit Data for Periods of High Solar Activity," *Advances in the Astronautical Sciences*, Vol. 134, AAS 09-104, Univelt, 2009, pp. 23-42.
53. B. D. Tapley, B. E. Schutz, and G. H. Born, *Statistical Orbit Determination*, Elsevier Academic Press, Amsterdam, 2004.
54. J. R. Wright, "Real-Time Estimation of Local Atmospheric Density," *Advances in the Astronautical Sciences*, Vol. 114, AAS 03-164, Univelt, 2003, pp. 927-950.
55. J. R. Wright and J. Woodburn, "Simultaneous Real-Time Estimation of Atmospheric Density and Ballistic Coefficient," *Advances in the Astronautical Sciences*, Vol. 119, AAS 04-175, Univelt, 2004, pp. 1155-1184.
56. National Aeronautics and Space Administration, "CHAMP," Last Accessed: April 14, 2010.
57. GRACE: Gravity Recovery and Climate Experiment: Center for Space Research, "GRACE Orbital Configuration," August 2, 2007, Last Accessed: April 14, 2010, http://www.csr.utexas.edu/grace/operations/configuration.html.
58. Infoterra GmbH, "TerraSAR-X: First Commercial 1m Radar Satellite," 2010, Last Accessed: April 10, 2010, http://terrasar.de/terrasar-x.html.
59. A. Hiatt, "Deriving Atmospheric Density Estimates Using Satellite Precision Orbit Ephemerides," M.S. Thesis, University of Kansas, 2009.
60. R. Konig, S. Zhu, C. Reigber, K. H. Neumayer, H. Meixner, R. Galas, G. Baustert, "CHAMP Rapid Orbit Determination for GPS Atmospheric Limb Sounding," *Advances in Space Research*, Vol. 30, No. 2, 2002, pp. 289-293.
61. G. Michalak, G. Baustert, R. Konig, C. Reigber, "CHAMP Rapid Science Orbit Determination: Status and Future Prospects," *First CHAMP Mission Results for Gravity, Magnetic and Atmospheric Studies*, eds. C. Reigber, H. Luhr, P. Schwintzer, Springer, Berlin, 2003, pp. 98-103.
62. R. Konig, G. Michalak, K. H. Neumayer, S. Y. Zhu, H. Meixner, C. Reigber, "Recent Developments in CHAMP Orbit Determination at GFZ," *Earth Observation with CHAMP Results from Three Years in Orbit*, eds. C. Reigber, H. Luhr, P. Schwintzer, J. Wickert, Springer, Berlin, 2005, pp. 65-70.

63. R. Konig, G. Michalak, K. H. Neumayer, S. Zhu, "Remarks on CHAMP Orbit Products," *Observation of the Earth System from Space*, eds. J. Flury, R. Rummel, C. Reigber, M. Rothacher, G. Boedecker, U. Schreiber, Springer, Berlin, 2006, pp. 17-26.
64. O. Montenbruck and E. Gill, *Satellite Orbits: Models, Methods, and Applications*, Springer-Verlag, Berlin, 2001.
65. J. R. Wright, "Optimal Orbit Determination," *Advances in the Astronautical Sciences*, Vol. 112, AAS 02-192, Univelt, 2002, pp. 1123-1134, http://www.agi.com/downloads/support/productSupport/literature/pdfs/whitePapers/optimal_od.pdf.
66. Analytical Graphics, Inc., "Orbit Determination Tool Kit Help," *Orbit Determination Tool Kit*, Version 5.1.4.
67. B. R. Bowman, F. A. Marcos, K. Moe, M. M. Moe, "Determination of Drag Coefficient Values for CHAMP and GRACE Satellites Using Orbit Drag Analysis," *Advances in the Astronautical Sciences*, Vol. 129, AAS 07-259, Univelt, 2008, pp. 147-166.
68. P. Bourke, "Cross Correlation," August 1996, Last Accessed: March 24, 2010, http://local.wasp.uwa.edu.au/~pbourke/miscellaneous/correlate/.
69. Geological Survey of Canada, "Geomagnetism: North Magnetic Pole," Jan. 2008, Last Accessed: March 28, 2010, http://gsc.nrcan.gc.ca/geomag/nmp/northpole_e.php.